MECHANOCHEMICAL FABRICATION AND CHARACTERIZATION OF NOVEL LOW-DIMENSIONAL MATERIALS

A Dissertation

by

DAVID RYAN HUITINK

Submitted to the Office of Graduate Studies of
Texas A&M University
in partial fulfillment of the requirements for the degree of

DOCTOR OF PHILOSOPHY

August 2011

Major Subject: Mechanical Engineering

Mechanochemical Fabrication and Characterization of Novel Low-Dimensional Materials

MECHANOCHEMICAL FABRICATION AND CHARACTERIZATION OF NOVEL LOW-DIMENSIONAL MATERIALS

A Dissertation

by

DAVID RYAN HUITINK

Submitted to the Office of Graduate Studies of
Texas A&M University
in partial fulfillment of the requirements for the degree of

DOCTOR OF PHILOSOPHY

Approved by:

Chair of Committee,	Hong Liang
Committee Members,	K. Ted Hartwig
	Warren Heffington
	Phillip Hemmer
Head of Department,	Dennis O'Neal

August 2011

Major Subject: Mechanical Engineering

ABSTRACT

Mechanochemical Fabrication and Characterization of Novel Low-Dimensional Materials. (August 2011)

David Ryan Huitink, B.S.; M.S., Texas A&M University

Chair of Advisory Committee: Prof. Hong Liang

In this research, for the first time, a novel nanofabrication process is developed to produce graphene-based nanoparticles using mechanochemical principles. Utilizing strain energy at the interface of Si and graphite via the use of a tribometer, a reaction between nanometer sized graphite particles with a reducing agent (hydrazine) was initiated. This simple method demonstrated the synthesis of lamellar platelets (lamellae of ~2nm) with diameters greater than 100 μm and thicknesses less than 30 nm directly on the surface of a substrate under rubbing conditions. Spectroscopic evaluation of the particles verified them to be graphene-based platelets, with functionalized molecules including C-N and C-Si bonding. Furthermore, the size of the particles was shown to be highly correlated to the applied pressure at the point of contact, such that three-body friction (with intermediate particles) was shown to enhance the size effect, though with greater variation in size among a single test sample. A chemical rate equation model was developed to help explain the formation of the chemically modified graphene platelets, wherein the pressure applied at the surface can be used to explain the net energy supplied in terms of local flash temperature and strain energy. The activation

energy calculated as a result of this method (~42kJ/mol) was found to be extraordinarily close to the difference in bond enthalpies for C-O and the C-N, and C-Si bonds, indicating the input energy required to form the platelets is equivalent to the energy required to replace one chemical bond with another, which follows nicely with the laws of thermodynamics.

The ability to produce graphene-based materials using a tribochemical approach is a simple, one-step process that does not necessarily require specialized equipment. This development could potentially be translated into a direct-write nanopatterning procedure for graphene-based technologies, which promise to make electronics faster, cheaper and more reliable. The tribochemical model proposed provides insight into nanomanufacturing using a tribochemical approach, and suggests that further progress can be accomplished through the reduction of the activation energy required for graphene formation.

For my wife, Linsay,

and our children: Davis, Levi, and Isabella.

I love you!

ACKNOWLEDGEMENTS

As in any major accomplishment of mine, the accolade would never have been possible without the efforts, contributions, and support of many others, to whom I am deeply grateful. Particularly for an endeavor of such a great magnitude, so many are due my thanks, and I do not have the space to list all of those who assisted and encouraged along the way.

Thanks are first due to my advisor, Dr. Hong Liang, for her guidance and support during my doctoral program. She has been a spectacular mentor and has taught me incredibly much about achieving success in the academic environment. Also, thank you to the rest of my Ph.D. committee: Dr. K. Ted Hartwig, Dr. Warren Heffington, and Dr. Phillip Hemmer. Thank you for your constructive comments, advice and willingness to help me through difficult problems.

Thanks to my co-workers and collaborators: many of you have contributed to this work in various ways, whether directly through assistance with measurements or indirectly through discussions and asking tough questions. I especially would like to thank Dr. Feng Gao, Dr. Subrata Kundu, Dr. Ke Wang, Dr. Luohan Peng, Dr. Funda Aksoy, Chiwoo Park, Rodrigo Cooper, Yan Zhou, Matt Sanders, Sukbae Joo, Oliver Mulamba, Michael Cleveland, Xingliang He, and Melissa Clough. Each of you has helped me with various measurements or analysis procedures during my Ph.D. studies, and I appreciate all of your contributions.

Without the proper tools, a scientist is only a wishful thinker; and without the experts to navigate the use of scientific tools, the scientist wishes the tools would work! Thank you to each of the staff scientists and facilities managers who helped me to use equipment for obtaining results presented in this dissertation. Thanks to Dr. Zhi Liu at Lawrence Berkeley National Laboratory for access and help with the ambient pressure photoemission station. Thanks to Dr. Gang Liang and Dr. Amanda Henkes for assistance with Raman at the Texas A&M Materials Characterization Facility. Support by Dr. Zhiwei Shan and Dr. Andrew Minor at the National Center of Electron Microscope for *in situ* TEM analysis was greatly appreciated.

Finally, thank you to my family for all of your support and encouragement during this degree program. Thank you especially to my beautiful wife, whose love and encouraging attitude continually inspires me. Thank you also for taking care of our kids by yourself while I worked or traveled, and for working hard to make our home a wonderful place to come home to. I love you and I am grateful to spend my life with you! And thanks to my children, Davis, Levi, and Isabella; I never would have anticipated the joys of being your dad! You make me smile. I love you.

NOMENCLATURE

Acronyms

AFM	Atomic force microscope
CTE	Cycle-to-event
CMG	Chemically modified graphene(s)
FTIR	Fourier transform infrared spectroscopy
GO	Graphene oxide
NP	Nanoparticle
SEM	Scanning electron microscope/microscopy
TEM	Transmission electron microscope/microscopy
Tribosynthesis	Synthesis methodology using a tribological procedure
XPS	X-ray photoelectron spectroscopy/spectrometer
XRD	X-ray diffraction

Symbols

A	Contact area
A*	Contact area of asperity/third body particle
C	Heat capacitance
E_a	Activation energy
k	Thermal conductivity
k_B	Boltzmann constant: 1.380×10^{-23} J/K
l	Length between asperities
L	Normal load

p	Pressure
r	Radius of contact
r^*	Radius of contact by asperity
R	Universal gas constant: 8.314 J/K·mol
T	Temperature
ΔT_{flash}	Flash temperature rise
δ	Periodicity factor for contact points
μ	Coefficient of friction
κ	Thermal diffusivity
ρ	Density
#	Number of contact asperities/particles per nominal contact area

TABLE OF CONTENTS

Page

Page

LIST OF FIGURES

Page

Page

Page

Page

Page

Page

LIST OF TABLES

Page

1. INTRODUCTION: MECHANOCHEMISTRY AND NANOMATERIALS

The mass production of personal computers over the past 30-40 years has resulted in the increasing need for faster and more cost efficient devices. This largely has been accomplished through the scaling down of integrated circuit (IC) devices through the development of photolithography techniques and similar technologies, but the need for smaller and smaller circuit elements has driven the need for more sophisticated and elaborately engineered devices. One promising area of science that has developed in recent years lies in the emergence of nanotechnology. Herein, scientists and engineers have developed methods to create materials on the nanometer scale (10^{-9} m) for various applications ranging from chemistry to cosmetics. The research presented in this dissertation investigates a new methodology of creating nanomaterials and the scientific understanding of this technique. This introductory section discusses the concepts and prior research that serves as a background for the research endeavor presented thereafter.

1.1. It's a Small World after All: Nanotechnology

As a result of discovering promising mechanical, thermal, and electrical properties, etc. that are discussed in the following section, nanotechnology has emerged as a leading topic among academic researchers, and has begun to find its way into commercial products. Not only have new properties and products been discovered, but encroaching on the atomic scale has led to new understanding of how the world behaves as a result of atom and molecule interactions. This exciting new field has led to many

---

This dissertation follows the style of *Applied Physics Letters*.

new discoveries and breakthroughs in terms of understanding material behaviors and interactions at the nanoscale, leading to various novel engineering applications.

1.1.1. Graphene: The "nano" Holy Grail

Perhaps one of the most highly researched and sought after nanomaterials in recent years is found in graphene. In fact, because of its incredible properties and promise for future technology, Andre Geim and collaborator K. Novoselov received the 2010 Nobel Prize in physics for their contributions to the characterization and pioneering research in graphene in the past 10 years.[1] Defined as a single atomic layer of graphite, the sp^2 electronic configuration for carbon, graphene is essentially the fundamental unit of all major carbon nanomaterials studied in recent years (with the notable exception of diamond which is the sp^3 configuration).[2] Because of the planar electronic configuration of the sp^2 hybridization, carbon (as graphene) forms a single layer of atoms arranged in a hexagonal lattice.[3] A schematic of graphene and the sp^2 electronic configuration of carbon are shown in Figure 1. When curled into a sphere, graphene is better known as a fullerene, or "buckyball," which often has been described as a 0-D material. Likewise, when rolled into a cylinder, the tube shape has come to be known as the 1-D carbon nanotubes (CNTs), which also have many promising properties. The most common of the sp2 hybridization is its 3-D form as graphite, which is built of a layered structure of individual graphene planes, loosely connected by van der Waals forces.[3] But the most interest in research has been generated over the production of 2D atomically thick layers of graphene, by which many amazing technologies may be developed if a suitable production technique may arise.

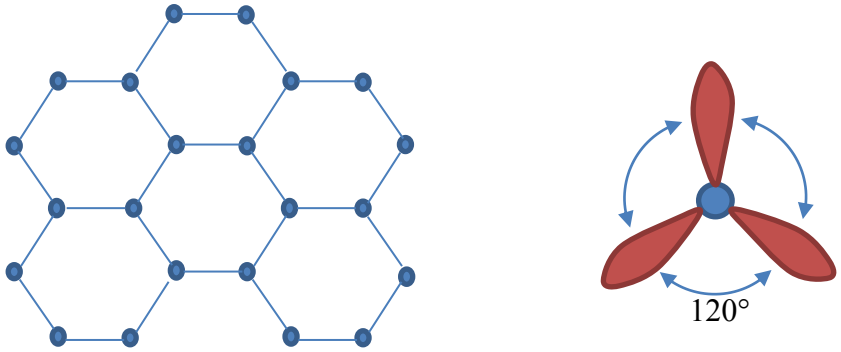

Figure 1. Graphene hexagonal lattice structure (left) and carbon sp^2 hybridization (right)

More interestingly, the electronic configuration and the resulting structure of graphene results in amazing properties. Graphene has experimentally and theoretically been shown to have enormous strength and modulus,[4,5] superior thermal[6] and electrical conductivity[2,7] as compared to conventional materials like copper, and even has unique optical behavior.[8] Table 1 summarizes some of the properties of graphene found among literature.

Perhaps the most intriguing characteristic of graphene comes from its electronic band gap. In fact, it is sometimes referred to as a "zero-gap semiconductor" because of its unique electronic structure.[9] This physical phenomena results in the high conductivity, as well as the optical properties, but also allows for the use of graphene as a field effect transistor (FET) since its gap can be adjusted by local electric or magnetic fields.[10] Additionally, graphene is studied fervently among physicists due to its quantum Hall effect, which arises from its unique electronic structure.[11] These properties and

abilities lead to the potential applications of graphene in molecular switches in integrated circuits,[12] flexible touchscreens and solar collectors,[13,14] and many other applications.[15]

Table 1. Experimentally measured properties of graphene

Category	*Material Property*	*Value*	*Reference*
Mechanical	Bulk Strength (extrapolated)	130 GPa	[4]
	Modulus	0.5-1 TPa	[5,16]
	Stiffness	1-5 N/m	[16]
Thermal	Conductivity	~5×10^3 W/m·K	[6]
Electrical	Electron Mobility	15,000 $cm^2/V\cdot s$	[2]
	Resistivity	10^{-6} Ω·cm	[7]
Optical	Absorption	2.3% of white light per atomic layer	[8]

Unfortunately, the largest drawback for the implementation of graphenes in engineered devices is the inability to produce graphene sheets in a useful form and with controlled size and shape. A number of chemists have performed various studies on the production of graphenes and chemically modified graphenes (CMGs) with moderate success from building on former research on the production of graphite oxide (GO).[17,18] For instance, Tung et al. demonstrated the production of up to 20×40 μm graphene sheets by reducing GO sheets in hydrazine (N_2H_4).[19] Gilje, et al. also demonstrated a method consisting of spray coating GO sheets onto a substrate, and then subsequently reducing the GO with hydrazine, allowing for larger scale utilization of graphene layers for electronic applications.[20] Several additional chemistry-based techniques have been

employed (see Table 2), and each result in a colloidal suspension of graphene or CMG flakes. The challenge then becomes how to assemble these flakes in a useful way.

Table 2. Recent successes in colloidal CMG synthesis from graphite oxide and similar. Adapted from reference [21]

Researchers	Description of CMG Production	Size of CMGs (lateral dim. × thickness)	Reference
Li, et al. 2008	GO dispersed in water using modified Hummer's method[17]	Several hundred nm × 1 nm	22
Paredes, et al. 2008	GO dispersed in water, acetone, ethanol, 1-proponol, ethylene glycol, DMSO , DMF, NMP, pyridine, THF using Hummer's method	Up to 1 µm × 1.0-1.4 nm	23
Tung, et al. 2008	GO dispersed in hydrazine using modified Hummer's method	Up to 40 µm × 0.6 nm	19
Muszynski, et al. 2008	GO dispersed in THF using Staudenmaier method[18] & decorated with Au NPs	? × 1-2 nm	24
Williams, et al. 2008	GO dispersed in ethanol by Hummer's method & UV assisted photocatalyzation	Several hundred nm × 2 nm	25
Hernandez, et al. 2008	Graphite powder exfoliated in NMP, DMAc, GBL, DMEU	Several µm × 1-5 nm	26
Liu, et al. 2008	Graphite rod electrochemically exfoliated in DMF, DMSO, NMP	500-700 nm × 1.1 nm	27

1.1.2. Nanofabrication Techniques: "Top-Down" and "Bottom-Up"Approaches

When considering the production of nanomaterials and other low-dimensional material products such as thin films and flake-like particles such as graphene, the fabrication processes have been typically classified in two ways: "top-down" and "bottom-up" methods. In top-down methods, a bulk material is broken down into smaller elements – usually by a mechanical process. Some examples of top-down methods include photo[28] and X-ray lithography,[29] nanoimprint lithography,[30] laser

ablation,[31] and sputtering.[32] Alternatively, in bottom-up techniques, the precise combination of reactants under the proper conditions leads to the chemical formation of new particles, as demonstrated in the widely used sol-gel and colloidal synthesis techniques.[33] This second, chemistry-based method can often lead to more controllable and designed particles; however, the mechanical processes are often much simpler and cost-effective in producing nanomaterials. Both methods have pros and cons, which must be weighed when considering how to process the specific materials needed for their intended application, whether it be catalysis, integrated-circuit (IC) devices, colloidal mixtures for cosmetics or lubricants, etc., medical technologies, or some other nanoparticle technology.

1.1.3. Direct-write Nanofabrication

In terms of developing nanomaterials for integrated circuit fabrication, several researchers have investigated the use of "direct-write" procedures for patterning nanowires and circuit elements directly onto a substrate. This method could potentially obtain higher resolution patterns as compared to lithographic techniques, as it is not limited by the diffraction of light. In fact, Peng et al. evaluated a AFM based technique for writing metallic nanowires as electrodes.[34] Others have tested indirect patterning of elements using dip pen nanolithography to first pattern a chemical substance followed by additional deposition processes.[35] Additionally, in regards to graphene production and isolation, Zhang et al. developed the use of a "nanopencil" to isolate graphitic layers of small size and subsequently measure their transport properties.[36] Unfortunately, this method only allowed for the deposit of submicron-sized graphene platelets which were

not regularly spaced or even single layers in many cases. Even so, the direct write approach offers an incredible precision in the placement and production of nanomaterials, however, the processing time and related cost is much greater as a result.

Ideally, if the cost effectiveness of top-down could be combined with the reactive selectivity of bottom-up methods, the potential for greater technological benefits through nanotechnology could be realized.

1.2. Mechanochemistry: Bridging the Gap

A possible route for accomplishing controllable synthesis at low processing costs may be found in mechanochemistry.[37] As a relatively unexplored branch of chemistry when compared to thermochemistry (read: classical chemistry), electrochemistry, and photochemistry, mechanochemistry offers alternate reaction pathways for chemical synthesis while having lower costs since its primary process parameter is force. Simply defined, mechanochemistry is the chemical transformation (or reaction) of a substance as a result of forceful interaction.[37] Since solid materials and even molecules have a defined structure, they can be influenced by a physical strain, leading to shear, compression, tension, or bending of their molecular arrangement. As described by J.J. Gilman and illustrated in Figure 2, these strains can lower the energy gap between the highest occupied molecular orbital (HOMO) and the lowest unoccupied molecular orbital (LUMO), leading to the formation of a new chemical bond which wouldn't otherwise exist.[38]

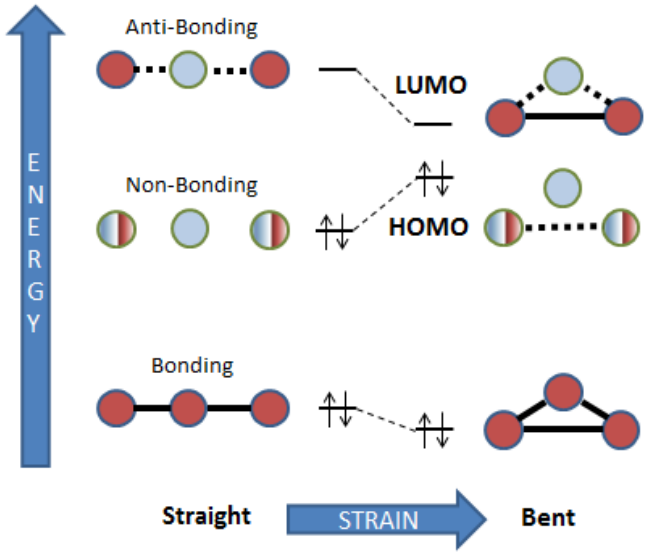

Figure 2. Illustration of mechanochemical reaction as a result of strain induced HOMO-LUMO gap modification. Adapted from reference [38]

In fact, by using mechanochemisty so-called "non-equilibrium" materials can be obtained![39] For instance, classical thermodynamics requires that for a chemical reaction to proceed, the Gibb's free energy of the reactants must be more than the products, or in other words, the free energy of the system must decrease during a reaction. According to this statement, gold cannot be oxidized. Even so, Thiessen et al. demonstrated the reaction $4Au+3CO_2 \rightarrow 2Au_2O_3+3C$ through a simple rubbing experiment.[40] This "violation" of thermodynamics can be better understood when considering that the mechanical strain from rubbing created a new reaction pathway by which the force input raises the system energy such that the transformation allows the system to stabilize under the strain. Furthermore, a recent review of several hundred papers on bond breakage and polymer fracturing by mechanical activation systematically showed the dominance of force dependent reactions in systems where thermal influence was negligible to non-

existent proving the definitive dependency on externally applied forces.[41] Unlike temperature variations which increase the vibration energy of atoms or molecules, the strain energy is directional, based on the type of stress input. When considering the Lennard-Jones model[42] of potential energy vs. interatomic distance, it can be inferred that the compression or tension of a molecule results in the movement of the equilibrium separation distance along the potential curve, as illustrated in Figure 3. Conversely, altering chemical reaction pathways with electrical or photochemical perturbations will change the nature of the potential energy diagram.

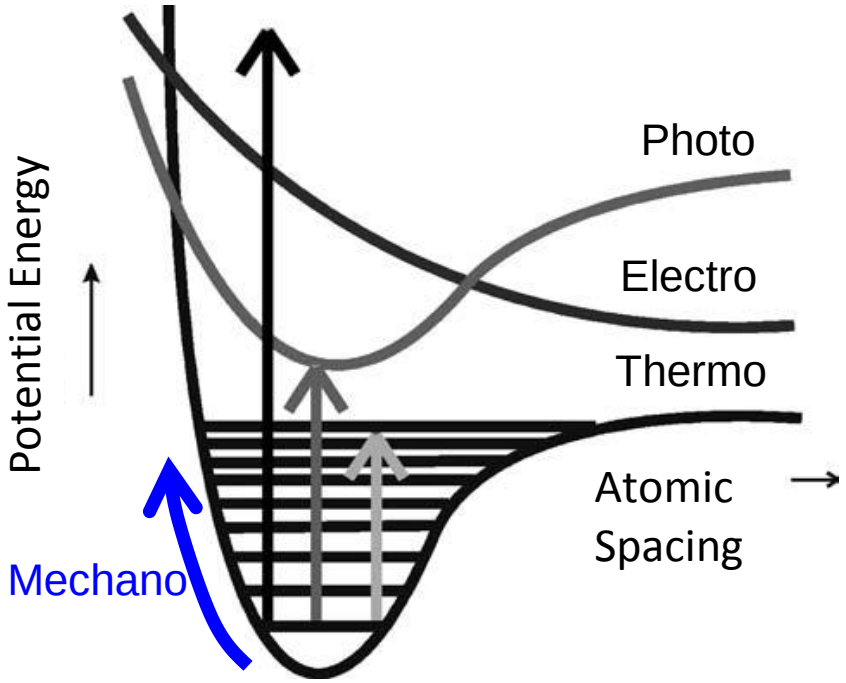

Figure 3. Potential energy vs. interatomic/molecular separation for various chemical pathways. Adapted from reference [43]

In attempt at explaining the tendency of molecules to bend, stretch and eventually break or create new bonds as a result of an externally applied force, quantum mechanics offers the best explanation of the nature of these reactions. The nearing proximity of atoms or molecules based on an externally applied force can be represented as two encroaching electron "clouds" which exert an electric field on one another. From quantum mechanics, this can be represented in terms of an external potential applied in the Schrödinger equation. This modifies the Hamiltonian of the system such that the electrons will reconfigure to enter the lowest energy state. To approximate this behavior in a computational study of a cyclobutene derivative, Ribas-Arino et al. suggested a non-linear model using the Born-Oppenheimer potential energy surface by imposing a directionally applied force and minimizing the energy with respect to both the ground state and the "constrained geometry simulating external force" and the increased system energy of an "externally force explicitly induced" based on a defined molecular shape factor, q.[44] Additional efforts have been made using other computational techniques to model the behavior, but the challenge of predicting bond formation is immense due to the many different factors in play, including contact mechanics, quantum mechanics, and thermal influences.

Because of its relatively unexplored nature, according to Craig Eckhardt, the uniqueness of mechanochemistry makes it "the last energetic frontier" such that "…the direct effect on molecular degrees of freedom by mechanical energy, which will likely be due to compressive forces, *may be expected to generate new chemistry.*" [43]

1.2.1. Mechanochemistry in History

This uniqueness has been observed from ancient times, having first been recorded by Theophrastus of Eresus in 322 BC with the leaching of elemental mercury from ore when rubbing with a copper pin (HgS+Cu→Hg+CuS).[37] The ability to leach metals from ore using mechanical techniques has been used for many years in mining and waste processing industries.[45] In fact, throughout the last two millennia, various scholars have studied the intrigue of chemical transformations resulting from force. A timeline of some of the notable discoveries is shown in Figure 4.

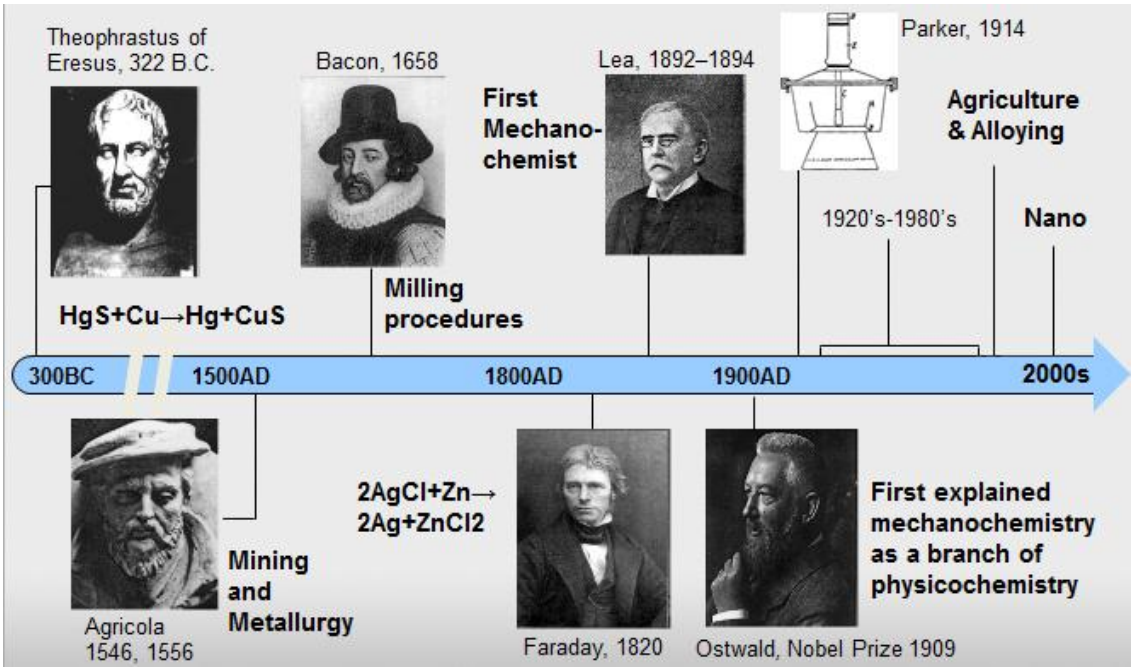

Figure 4. Timeline of advances in mechanochemistry. Adapted from reference [37]

As early as 300 BC documentation of mechanochemical reactions resulting in the isolation of elemental mercury was penned by Theophrastus of Eresus, a prominent student of Aristotle. Not until nearly 1800 years later did additional reports of mechanochemical procedures reemerge in the mining and metallurgy fields, and mathematician and scientist Francis Bacon, actually designed milling procedures for processing ore in a refinement process. Additional instances of mechanochemical reactions were discovered by a number of scientists and chemists during the Age of Reason, including Michael Faraday, but they had only "scratched" the surface. Some consider M. Carey Lea to be the "first mechanochemist" since he spent much of his scientific career devoted to understanding the effects of pressure and force on chemical reactions.[46] However, it was not until Nobel Prize winner Friedrich Ostwald coined the term that the reaction pathway became known as "Mechanochemistry."

1.2.2. Industrial Application of Mechanochemistry

More recently, mechanochemistry has found a significant role in mechanical alloying, where dissimilar materials which would not naturally alloy together are forced to form an alloy using a ball milling technique.[47] In fact, mechanical alloying can alloy materials in which one exhibits a much lower melting point than its counterpart, such as Mg-Ti.[39] This method can generate high strength or other interesting properties of alloys.[48] In polymer technologies, mechanochemistry has been recognized as a simple method to synthesize new polymer chains by the breaking of longer polymers.[49,50] These benefits have led to a number of industries having found profitable uses for mechanochemistry (see Table 3) [45]. Perhaps some of the greatest benefits are found in

the ability to process certain chemical reactions at lower temperatures and without the use of dangerous solvents which can be costly to dispose of and harmful for the environment. By applying mechanochemical techniques, scientists have demonstrated the ability to generate unique materials, for which many methods have become industrial processing techniques for all types of materials

.

Table 3. Industrial uses of mechanochemistry for various purposes

Industry	Application	Reference
Agriculture	• "Superphosphate" with increased water solubility for fertilizer • Increased fertilizer activity • Longer lasting effects	51 52 53
Minerology	• Lurgi-Mitterberg process: Extraction of Cu from Chalcopyrite • Activox process: Extraction of Au, Ni, Co and Cu from sulphides and calcines • MELT: Mechanochemical Leaching of tetrahedrites • Coal processing for novel properties	54 55 56 57
Metallurgy	• Mechanical Alloying • Super Alloys for Aerospace	47 48
Solid State Reactions for Molecular Engineering	• Simpler synthesis of molecules for applications in chemical additives, organic compounds etc. Reduces waste solvent.	58
Pharmacology	• New properties of compounds • Increased solubility and bioavailability • preparation of special diterpene compounds (kaurane derivates) with cytostatic activity for pharmaceutical effectors	59,60 60 57
Polymers	• Breaking longer polymer chains	50

1.2.3. Recent Experimental Observations

Additionally, several experiments performed during the course of the author's doctoral program revealed evidence of mechanochemical reactions taking place at the interfaces of contacting materials. For instance, when examining the nanoindentation of a gold coated probe into a silicon (100) substrate to understand the adhesion mechanisms involved with direct-write nanopatterning, the formation of interfacial materials was observed in a TEM, shown in Figure 5. In addition to visualizing the progression of indenting a surface to fracture, the in situ TEM analysis displayed the stress behavior at the surface that resulted in the generation of nano-sized nucleations of new material. A diffraction analysis revealed the material was a metastable material known as $AuSi_3$, which does not exist naturally.[61] Here it was discovered that through the application of pressure at ambient temperature and vacuum environment, the reaction proceeds like a high-temperature diffusion process – but surprisingly without any added heat. This mechanochemically formed interfacial material promotes both the adhesion of gold to Si as well as enhances the electrical continuity between the semiconductor substrate and deposited metal.

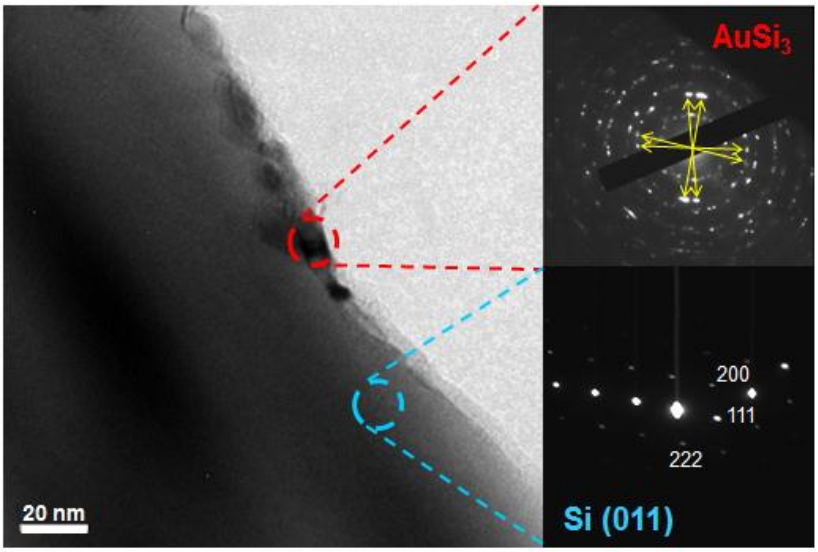

Figure 5. Diffraction pattern revealing the formation of interfacial $AuSi_3$ as a result of mechanochemical interaction.

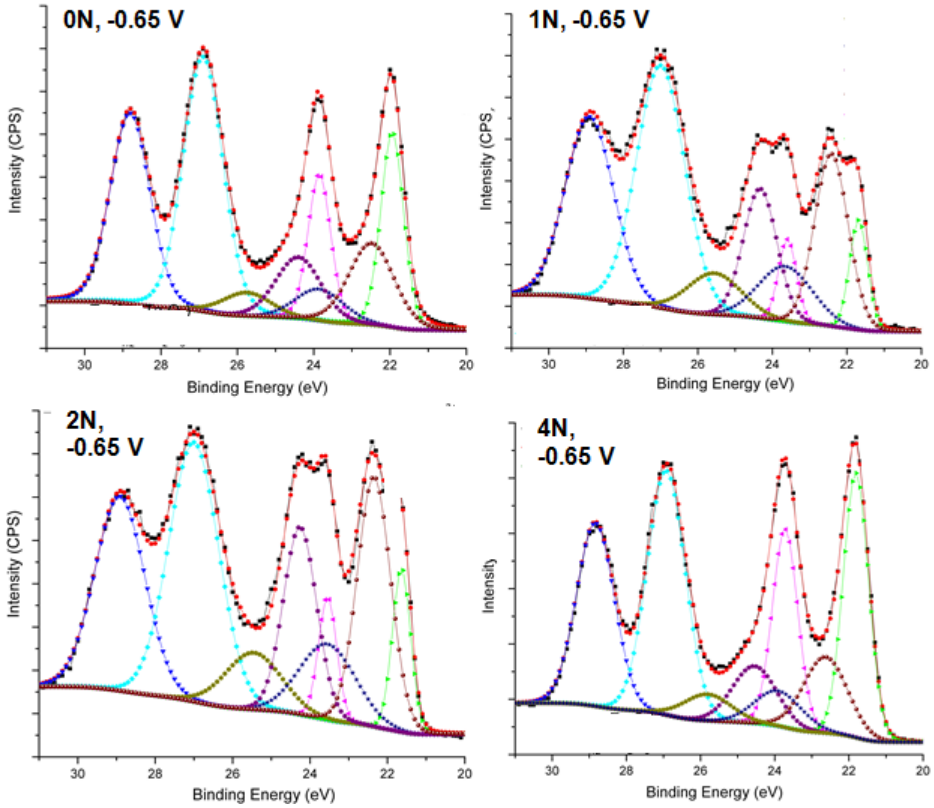

Figure 6. XPS spectra for processing under varying load with constant electrochemical reducing potential.

Furthermore, when looking at the effect of loading during electrochemical-mechanical polishing procedures, an XPS surface analysis (see Figure 6) revealed the stabilization of the metastable or intermediate sub-oxide states of tantalum. With increased pressure during a cathodic electrochemical potential, the surface was observed to have an increased contribution of the sub-oxides relative to the most stable oxide form: Ta_2O_5. When studying similar contact conditions inside an electrochemical AFM with an environmental cell, the repeated mechanical activation of a scanning probe was seen to alter the surface properties of the affected area, as revealed by a friction force scan of the surface after testing. As shown in Figure 7, the forceful action on the surface led to the reduced friction over the affected area, presumably as a result of the different chemical structure of the suboxides.[62] As shown in the schematic, the forceful interaction of the tip or polishing particles with the surface creates localized residual stresses that stabilize the presence of lower order oxidation states that normally do not exist at the surface.

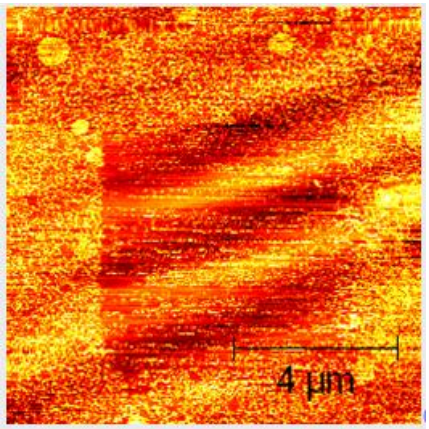

Figure 7. Evidence of chemically modified surface via contact forces from LFM measurement.

In another experiment, it was shown that even thermal expansion/compression can induce chemical nature of surfaces under some circumstances. As shown in Figure 8, when heating a lead sheet to a temperature of 150°C, the higher order oxidation states tend to transform into the most stable state, as might be expected. However, when rapidly cooling the surface back to room temperature, the other oxide states are observed to return, as well as the formation of a new oxide of even higher oxidation state. In this case, the thermal expansion during heating and subsequent compression upon cooling again evidenced a diffusive element in the migration oxide states at the surface. The compressive stress offered by the cooling of the sample appeared to "lock-in" oxygen atoms into a matrix of Pb such that the higher order oxidation state and related bonding might be stabilized, instead of allowing a more conventional development of PbO and PbO_2 states.

Irrespective of the pathway by which the stress was applied, it appeared from these investigations that the origin of the mechanochemically induced reactions was by definition at the interface of stress-inducing contact, as well as defined by molecular interactions. As such, the products of mechanochemically reacted surfaces are by nature nanoscale, and serve as intermediates in interfaces to reduce the surface energy. As nanoscale reactions, mechanochemistry is potentially an unexplored route to obtaining novel nanomaterials.

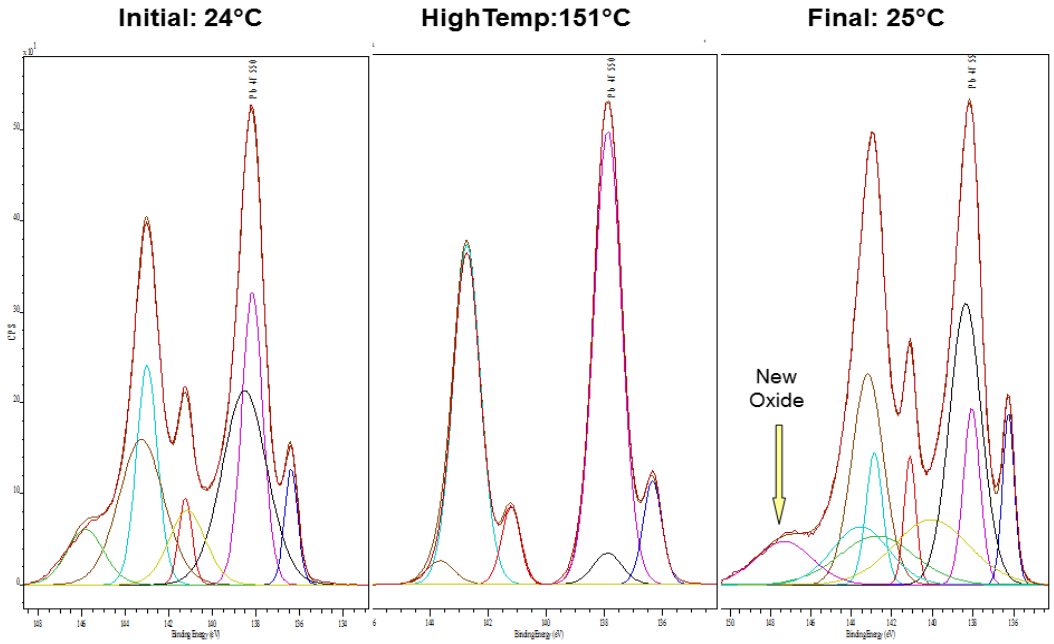

Figure 8. Observation of new oxide formation in Pb during heat/cool cycle.

1.3. Mechanochemistry for Nanomaterials

Since the advent of the "nano-craze," a few researchers have begun to explore mechanochemical routes through the use of ball milling techniques, like those used in mechanical alloying, to fabricate nanoparticles.[37,63-65] Several of the reactions induced by this high-energy milling technique have been recorded in Table 4 for reference. Some of the benefits of using this technique include small particle sizes (down to a few nanometers), fairly small size distributions, low agglomeration of nanoparticles, and the elimination of need for surfactants and chemical capping agents required in bottom-up synthesis processes.[37,63] Furthermore, the ball milling technique has allowed for the formation of particles either not previously available or in smaller sizes that enable enhanced surface properties. The combined benefit of chemically driven reactions

(bottom-up) with the cost-effectiveness of mechanical processing (top-down) makes mechanochemistry a field ripe for growth in nanotechnology. As stated by Peter Balaz, "mechanochemical processing of solids as a relatively novel and simple solid-state process for the manufacture of nanoparticles is on the way to be incorporated into the world of nanoscience and nanotechnology."[37]

Table 4. Mechanochemically synthesized nanoparticles in literature

Nanoparticle Category	Type	Reaction	Reference
Metallic	Fe	$FeCl_3 + 3\ Na \rightarrow Fe + 3\ NaCl$	66
	Co	$CoCl_2 + 2\ Na \rightarrow Co + 2\ NaCl$	67
	Ni	$NiCl_2 + 2\ Na \rightarrow Ni + 2\ NaCl$	67
	Cu	$CuCl_2 + 2\ Na \rightarrow Cu + 2\ NaCl$	68
Oxides	Al_2O_3	$2AlCl_3 + CaO \rightarrow Al_2O_3 + 3CaCl_2$	69
	ZrO_2	$ZrCl_4 + 2CaO \rightarrow ZrO_2 + 2CaCl_2$	70
	Gd_2O_3	$GdCl_3 + 3NaOH \rightarrow Gd_2O_3 + 3NaCl + 1.5H_2O$	71
	CeO_2	$CeCl_3 + NaOH \rightarrow CeO_2 + 3NaCl + H_2O$	72
	Cr_2O_3	$Na_2Cr_2O_7 + S \rightarrow Cr_2O_3 + Na_2SO_4$	73
	Nb_2O_5	$2NbCl_5 + 5Na_2CO_3 \rightarrow Nb_2O_5 + 10NaCl + 5CO_2$	74
	SnO_2	$SnCl_2 + Na_2CO_3 + O_2 \rightarrow SnO_2 + 2NaCl + CO_2$	75
	Fe_2O_3	$2FeCl_3 + 3Ca(OH)_2 \rightarrow Fe_2O_3 + 3CaCl_2 + 3H_2O$	76
	ZnO	$ZnCl_2 + Na_2CO_3 \rightarrow ZnO + 2NaCl + CO_2$	77
Sulphides	ZnS	$ZnCl_2 + CG\text{-}CaS \rightarrow ZnS + CaCl_2$	78
	CdS	$CdCl_2 + MA\text{-}Na_2S + 16NaCl \rightarrow CdS + 18NaCl$	79
	Ce_2S_3	$CeCl_3 + CG\text{-}CaS \rightarrow Ce_2S_3 + CaCl_2$	64
Carbonates	$CaCO_3$	$CaCl_2 + Na_2CO_3 \longrightarrow CaCO_3 + 2NaCl$	80

In a very few cases, chemists have begun to look at using mechanochemistry for modifying C_{60} "buckyballs" and other fullerenes.[81] Similar to the nanoparticle synthesis techniques, these researchers use high speed vibration milling (or ball milling) to

functionalize the surface of carbon fullerenes with a number of different functional groups. This allows the chemist then to encourage chemical interactions and binding between the relatively non-reactive buckyballs and some intentional chemical complex, perhaps for pharmaceutical use. A similar result was seen when staining carbon nanotubes, showing that the strained edges were more reactive with oxidative compounds, and also exhibited functional linkage through peptide bonds with polystyrene nanospheres.[82] Additionally, manipulation of molecular arrangement through mechanochemistry can cause amorphitization or formation of new polymorphs which may offer desirable functionality in molecular electronics or magnets.[39]

1.4. Tribochemistry

Despite the intriguing results seen in mechanochemical nanofabrication, researchers have yet to explore other techniques outside of ball milling in the production of mechanochemically synthesized nanomaterials. The use of ball milling primarily generates spherical particles, which must be separated from the other reaction products before it can be used in a potential application. One solution to eliminating this complicated and impractical step is to directly fabricate mechanically synthesized materials where they are desired. By using a tribological approach – that is, using friction through rubbing contact – a mechanochemical reaction can be initiated at the precisely positioned point(s) of contact. Recently, a novel approach to generating silver nanochains was demonstrated using a tribological technique using silver pins sliding in the presence of crown ether.[83] However, other than in this isolated case, nearly all aspects of tribochemical phenomena have been investigated for applications in the

lubrication industry. In fact, the phenomenon of surface transformation under sliding contact has long been known to affect the frictional behavior of contacting materials.[84] The resultant "tribo-film" is sometimes composed of elements of bearing coatings, raw materials, and even lubricants.[85] As a result, the term "tribochemistry" has come to represent mechanochemical transformation as the specific result of friction and wear.

1.4.1. State of the Art Applications in Tribochemistry

In fact, the development of tribofilms in an abrasive environment has found commercial application, especially in chemical additives for engine oil for reducing engine wear and friction. The most commonly cited instances of tribochemically derived lubrication modifiers are found in zinc dialkyldithiphosphate (or ZDDP) and molybdenum dialkyldithiocarbamate (or MoDTC). ZDDP, a polymeric solid, has been shown to react under pressure with ferritic surfaces (like steel) to form a protective coating of sulfides, oxides, phosphate polymers, and alkyl-phosphate precipitates that reduces wear and increases engine life.[86,87] The ZDDP molecules themselves do little to affect wear, but once forcefully reacted with the steel surfaces, it produces a sacrificial layer that is replenished by additional reaction of ZDDP with the steel surface.[86,88] But all good things must come with a cost – the presence of this protective film increases friction at the interface as the tribofilm is formed and scraped away with each stroke of contact.[86,89]

To alleviate the efficiency degradation due to the friction increase, lubrication engineers discovered that the addition of MoDTC can reduce the friction coefficient of moving engine components.[90,91] However, much like the ZDDP, the organo-metallic

additive alone does little by itself to lower the friction, but instead, the frictional activation (tribochemistry) results in the formation of MoS_2 platelets.[86,92] These molecules, like graphite, exhibit a lamellar structure with weak Van der Waals forces tying the layers together, such that the layered flakes can easily slide over one another, resulting in reduced friction.[93] When combined together with ZDDP in engine crankshafts, the resulting combo of friction modifying MoS_2 and wear reducing ZDDP results in a greatly improved engine performance and lifetime.[86] Furthermore, when looking into the formation and stability of these tribochemically derived interfacial barriers, Morina et al. found that the temperature at the surface can increase the rate of formation of the tribolayers, but is not required to induce the reaction, suggesting that thermal energy can influence tribochemical reactions, but is not necessarily required for tribofilm development.[86]

1.4.2. Existing Theory of Tribochemical Reactions

As a distinct type of mechanochemistry that relies on friction and sliding as opposed to pure contact and stress, tribochemical reactions behave similarly to mechanochemical reactions in the sense that they result from strain energy at a contact interface. However, in the investigation of tribofilm formations in lubricated sliding, surface reactions during sling have been classified into the following four categories by Kajdas and Hiratsuka:[94]

1. Purely tribochemical reaction resulting from friction and strain.
2. Thermochemical reaction induced by localized temperature increase.

3. Combination thermo-tribochemical reactions enhanced via action of both items 1 and 2.
4. Tribocatalytic reactions where catalysts aid the reaction process initiated by friction.

Generally speaking, both then influence of local heating and mechanical activation participate in tribochemical reactions, with heat enhancing the rate of the reaction according to the Arrhenius reaction rate model. However, the presence of the tribochemical reaction is not the result of temperature, but rather mechanical action leading to electron emission or "triboemission."[94] This emission has been thought to be result of temperature increases, and has even been theoretically coupled to the surface temperature in the Richardson-Dushman equation that relates low-energy electron emission flux (J) to surface temperature (T).

$$J = AT \cdot 2e^{\left(\frac{-\varphi}{kT}\right)} \quad 1.1$$

Here, A is a constant based on electron charge, mass, and Boltzmann and Planck constants equivalent to 120 A/cm^2K^2, k is the Boltzmann constant, and φ is the work function of the surface.[95] It has been presumed that these electrons interact with molecules in the interface that result in ionized particles that are prone to react with free radicals and nearby molecules. This process has been termed the negative-ion-radical action mechanism or NIRAM. [94] However, the temperature-based electron emission (thermionic emission) model would indicate that the same reactions could take place by simply raising the surface temperature through a thermochemical approach, yet this is not true.

To expand the idea of how reaction pathways exist through rubbing, Vizinitin proposed that freshly cleaved surfaces by the action of surface wear reveals unsaturated bonds that assist with bonding with the ionized radicals resulting from triboemission.[96] Often this results in oxidation or sulphurization of surfaces.[97] Furthermore, for lubricated surfaces, a process known as tribopolymerization can take place where lubricant molecules develop ionizations such that linkages form to polymerize the molecules.[98] Though different outcomes may arise, the triboemission resulting from the physics related to the wear of the surface is largely accepted to be the primary means of initiating reactions[99] with added energy though frictional heating, although J.J. Gilman suggested that mechanochemically based reactions can proceed athermally,[100] as witnessed experimentally.[61] Nakayama, in various different experiments,[101] reported measurements of various charged particles, as well as UV photons and electrons, indicating that emissions other than particles can result from sliding. This energy emission further supports the idea that the mechanical action is exciting the surface molecules into an "intermediate excited state" much like those seen in UV-vis absorption/emission processes, where exited electrons move into various energy states, then release the stored energy when returning to their ground state. Furthermore, this does not necessarily require breaking bonds as suggested by Vizintin.[96] Moreover, experimental collection of triboemitted electrons found that metallic surfaces did not emit measureable exoelectrons, while ceramic surfaces consistently emitted electrons of energies in the range of 1-5 eV.[102,103] In their review of triboemission processes, Kajdas and Hiratsuka concluded that "mechanically treated solids show that the reactivity often

increased by several orders of magnitude, particularly in the low-temperature range."[94] Furthermore, they acknowledged that the triboemission process is dominant in oxidized surfaces and likely requires such a surface to incite a reaction, as well as that "high energy wear particles are also important because they may act as a [reaction] catalyst."[94]

The extensive chemistry and physics research studies to understand how surfaces react with lubricants and organic molecules have contributed thoroughly to the understanding of tribochemical reactions. The NIRAM model has done well to conceptually describe the transformation of mechanical energy into chemical energy via the excitation of electronic states and emission of electrons (as well as electromagnetic energy). However, apart from the development of lubricant additives for friction and wear modification, the knowledge of these reactions has been ignored in terms of nanofabrication.

1.5. Summary

The field of nanotechnology has led to the development of many new materials and applications, and new methods of fabrication are constantly being tested and evaluated for the productions of new technologies. One fledgling approach is to use mechanochemistry to provide alternate reaction pathways for altering chemical constituency in nanoparticles. This long-known phenomenon has been recently demonstrated using ball milling techniques, but has very little exploration using a tribological approach. Additionally, in recent years tribologists have noted the presence of tribochemical reactions on wear surfaces leading to property variations, but insofar as applying the phenomena to producing low-dimensional materials, it has largely been

overlooked. The beauty of a tribochemical approach to producing nanomaterials and thin films, is that the process is extremely straightforward, cheap and can be applied to many different material groups. In this dissertation, the use of mechanochemical techniques, including tribological approaches, will be studied and evaluated for the fabrication of low-dimensional materials, specifically that of graphene.

2. MOTIVATION, OBJECTIVES AND APPROACHES

The relatively unexplored realm of mechanochemistry for the fabrication of low dimensional materials such as nanoparticles and thin films provides a nearly limitless backdrop for scientific pursuit of engineered materials. With the proper understanding of the interactions taking place during mechanochemical reactions, the design of new interfacial materials and particles previously undeveloped is made possible. This section briefly discusses the major motivations and objectives that stem from the ability to manipulate materials in this frontier field.

2.1. Motivation

As previously discussed, the unique nature of mechanochemistry provides alternate reaction pathways for the synthesis of nanomaterials. Additionally, the development of wear and friction-related mechanochemical reactions (or tribochemistry) has been relatively unexplored in nanofabrication. The ability to form novel materials at the interface of a bearing element and a substrate may provide the opportunity to generate highly localized and patterned depositions of novel low-dimensional particles and films for direct use as IC elements and/or interfacial boundaries. Specifically, if graphene nanomaterial could be produced in a reliable and repeatable fashion using a tribochemical approach, it would offer a great advantage over colloidal techniques that produce randomly distributed particles. More importantly, the prospect of creating these directly written nanostructures at low cost using a contact-based patterning procedure may facilitate the arrival of next-generation technologies such as the coveted quantum computer, ultrathin flexible electronics, touchscreens and solar collectors.

2.2. Objectives

The aims of this research work are to explore the use of mechanochemistry/ tribochemistry in the development of nano and mesoscopic graphene materials for use in next generation nanodevices. In order to accomplish this, three primary areas of research will be investigated: fabrication and processing, material characterization, and modeling of the tribochemical synthesis (or "tribosynthesis") procedure. Specifically, these areas will be addressed through the

- Development of tribochemical techniques for synthesis of graphene-based materials
- Identification and characterization of novel nanomaterials through mechanochemical techniques
- Modeling of the tribosynthesis processes in nanomaterials

2.3. Approaches

In order to achieve these objectives, each action item of fabrication, characterization and fundamental understanding will be addressed with the following approaches. For nanofabrication, the process development stage will consist of determining methods for fabricating using tribochemical techniques. Next the processes will be optimized to enable nanostructural design of the end product. The characterization stage consists of two elements: measuring the properties of the fabricated materials and determining the nature of the tribochemical reaction. In the property measuring and analysis stage, typical analyses for nanomaterials and thin films will be employed, including microscopy and spectroscopic measurements in addition to

in situ friction monitoring for observing surface energy change. Finally, to adequately explain the nature of the tribosynthesis reaction, the experimental observations will be considered in the development of a reaction rate equation based on processing conditions. The two aspects that will be covered will be force driven reactions – where a pressure induces a chemical change – in coordination with thermal influence from local temperature varioations. The flowchart in Figure 9 illustrates the approach in graphical format.

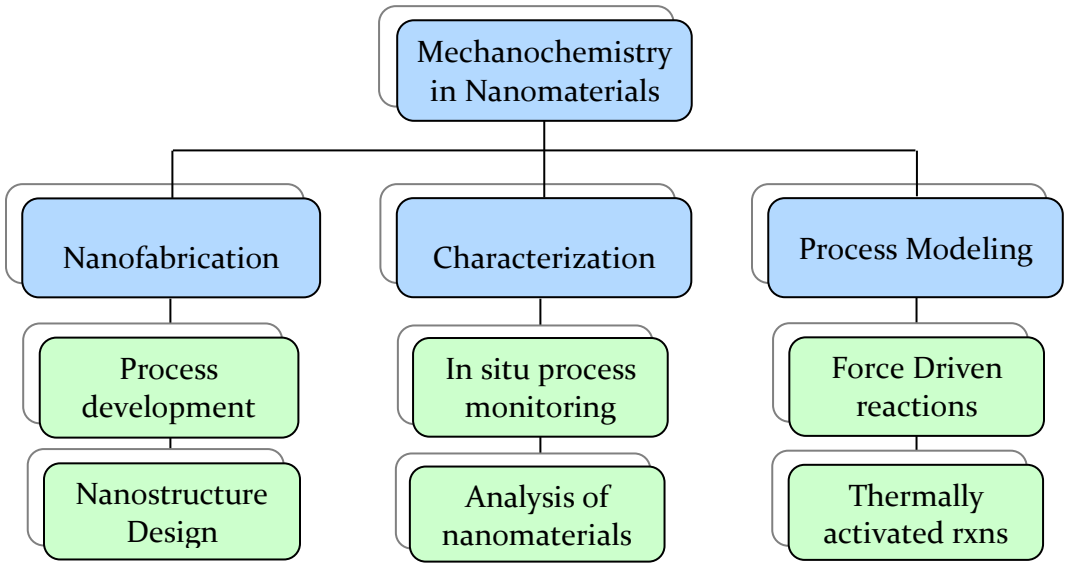

Figure 9. Objective flowchart

2.4. Summary

The tribochemical approach offers an exciting new vehicle for producing nanomaterials, yet it is still not well understood. In order to develop a useful nanomaterial processing technique (nanofabrication aspect) using a tribochemical

approach, an engineering model must be developed in conjunction with an understanding of the physics and chemistry (modeling aspect) based on observations of these reactions and material behaviors (characterization aspect). Each of these three aspects comprises the primary areas of research that are addressed in the following sections. Section 3 presents the tribochemical approach to nanofabrication of graphene-based materials and the associated process development. Section 4 categorizes the results obtained through the processing procedures and the corresponding material characterization. Finally, Section 5 evaluates the development of the graphene materials through an engineering model to describe the interfacial chemical reaction taking place during tribosynthesis.

3. TRIBOCHEMICAL NANOFABRICATION OF GRAPHENE-BASED NANOMATERIALS

Having seen the potential for new chemical pathways resulting from mechanochemical transformation, the engineering mindset begs to ask: "How can this phenomenon be used for a designed purpose?" As a primarily interfacial interaction, mechanochemistry offers a unique way to alter surface properties at the nano and molecular scale. As described in Section 1, a few scientists have begun to explore the possibilities of producing nanomaterials using a mechanochemical approach, which has led to the production of good size uniformity of nanoparticles of previously unexplored chemistries. However, this nanofabrication approach is still in its infancy, having only a small number of scientists contributing, and primarily from Eastern European research groups. Furthermore, the mechanochemical processing techniques are predominantly exclusive to ball milling procedures.

In this section, a tribological approach to mechanochemical production of low-dimensional materials and altered surfaces is presented. This procedure, termed "tribosynthesis" is based on the utilization of energy supplied via friction and contact stress to induce chemical reactions for the production of nanomaterials. This study largely focuses on the use of graphitic materials, for the production of graphenes and chemically modified graphenes, which serve as a prototypical nanomaterial.

3.1. Experimental Approach

Nobel Prize laureate Andre Geim previously surmised that graphene flakes are present in marks left by pencils,[104] suggesting that it may be possible to extrapolate this feature into a tribosynthesis technique. In fact, the use of a tribochemical technique to producing graphenes or CMGs offers three primary advantages. First, since it is an interfacial technique, it allows for the direct production of graphenes at a specified contact location. This direct method eliminates the need for separation and placement procedures required to deposit CMGs fabricated using a colloidal technique. Second, since the reaction can theoretically be regulated via the application of strain energy, it offers a more controllable method for producing CMGs of specified size, etc. Third, since a tribochemical approach is based on contact geometries, it is a scalable process that can be used in large industrial processes down to nanoscale experiments. Furthermore, an atomic force microscope provides a nanoscale equivalent to a tribometer and would allow for similar conditions in a nano-precise environment – particularly in the controlled environment of a wet-cell.

3.1.1. Materials and Methods

In order to accomplish a tribochemical reaction, a tribometer (CSM Instruments) was used to selectively pattern a tribochemically generated film on the surface of a substrate. A schematic of the basic setup is shown in Figure 10. As described in the figure, the use of this technique allows for the precise control of applied pressure, sliding velocity and sliding distance to take place during the reaction. Additionally, the selection of materials and liquid or gas mediums during sliding can be chosen

preferentially according to the planned reaction. In order to accomplish this task of producing CMGs with a tribochemical route, the tribometer was equipped with a sharpened graphite rod (6mm diameter, 99.999%, low density, Sigma-Aldrich) as a pin. The 6mm rod was sharpened to a ~250-500μm diameter point using a knife. To eliminate contamination of this rubbing partner, the pin was stored in ethanol and allowed to dry before each experiment.

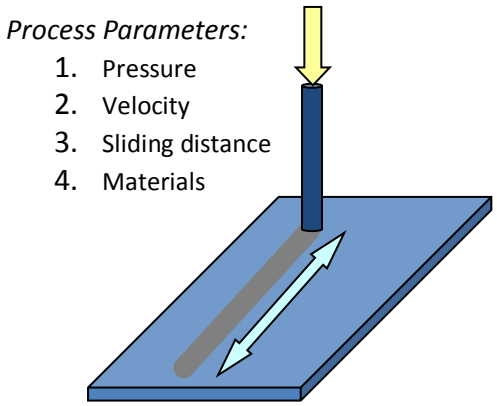

Figure 10. Tribochemical experimental setup

This particular setup is poised for micro-scale reactions, as the reaction "chamber" volume is essentially a function of the contact area. For the tribometer based experiments presented in this section, the contact area under the sliding pin was approximately 0.05mm^2, and a sliding distance of 10 mm was typical.

As a substrate, single crystal silicon (100) was selected for its smooth surface, which would help to maintain uniform contact behavior as the graphite pin slid across its surface. As an alternate reaction surface, a CVD produced Si_3N_4 deposited on (100) Si

(200nm thick as received, University Wafer) was also tested to investigate the role of Si in the formation of tribochemically produced CMGs. Its surface roughness is nearly identical to the untreated Si, but the nitrided surface possesses a higher hardness and toughness than Si.[105] In addition to their smooth surfaces which help to mitigate high local contact stresses at asperities, these two substrates are commonly used in the integrated circuit industry for circuit architecture due to their compatibility with common processing techniques. Silicon offers semiconducting properties that can be used in a device, while Si_3N_4 behaves as a dielectric that can serve as barrier layers in electronics or serve as structural elements in three-dimensional integrated circuits and micro-electromechanical systems (MEMS). By using these IC based material systems, the experiments described herein can potentially be directly translated into an industrial process, working in conjunction with classical photoresist/etching procedures.

3.1.2. Graphite Tribosynthesis Control Experiments

A series of control tests using the graphite pin rubbing against the Si and Si_3N_4 surfaces without any lubrication or chemical medium was first evaluated. Table 5 describes the test parameter matrix studied for these experiments. As can be seen in this table, the combinations of various load and speed conditions were tested, to evaluate the influence of pressure, shear rate, and dwell time on the interfacial reactions. At each load/speed condition, a two-cycle test was performed. To test the influence of the number of cycles, each load was tested at 50 cycles at the speed condition of 2cm/s. In the 4N loading case, further cycling (200) was performed to verify that no further reaction would occur.

Table 5. Testing matrix for control experiments of graphite on Si and Si_3N_4

Load / Speed	1N	2N	3N	4N
1 cm/s	2cyc	2cyc	2cyc	2cyc
2 cm/s	2, 50cyc	2, 50cyc	2, 50cyc	2, 50, 200 cyc
3 cm/s	2cyc	2cyc	2cyc	2cyc
4 cm/s	2cyc	2cyc	2cyc	2cyc

3.1.3. Optimized Chemistry with $N_2H_4 \cdot H_2O$

Additionally, a number of "enhanced chemistry" experiments were performed using intermediary chemicals and nanoparticles to assist in the formation of CMGs. With researchers having recent success in the use of hydrazine (N_2H_4) for preparing CMGs via thermochemical pathways (see Table 2),[21] hydrazine hydrate ($N_2H_4 \cdot H_2O$) was naturally chosen as a suitable medium for tribochemistry with graphite. Hydrazine has been found to act as a reducing agent for graphite oxide (GO) to graphene (G) according to the presumed process represented in Figure 11 below.

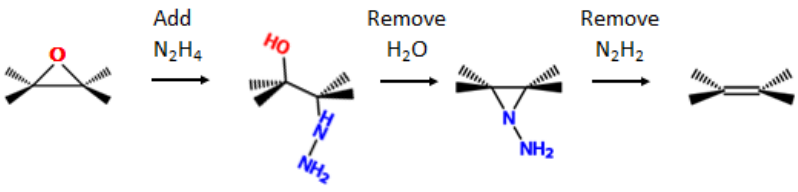

Figure 11. Presumed reduction process of GO to graphene from reference [106]

Additionally, computational studies of the decomposition of GO into graphene found slightly different results,[107] in which the process may take several routes (primary route indicated in Figure 12) including for cases in which the graphite has carboxyl terminal groups. In either case, the result is the hydrogenation of oxygen or hydroxide groups on the surface of the carbon structure, followed by a removal of H_2O and N_2H_2 molecules according to the following pseudo-reaction:

$GO + N_2H_4 \rightarrow G + N_2H_2 + H_2O$

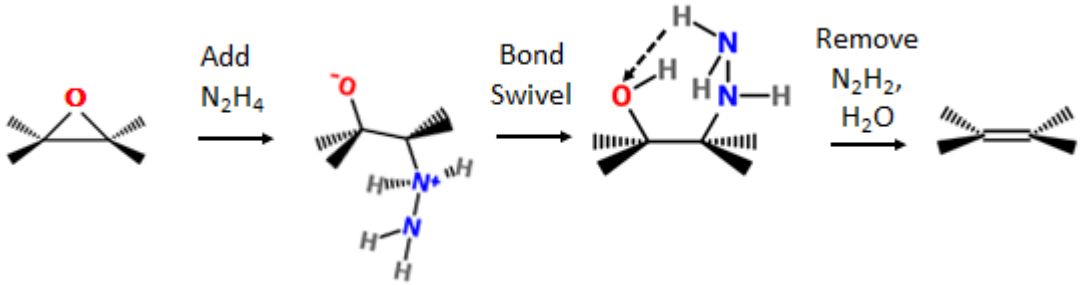

Figure 12. Computationally derived reduction scheme for GO with hydrazine from reference [107]

Essentially, the hydrazine breaks down the oxygen and hydroxyl terminals attached to defects in the graphitic lattice, which facilitates the "healing" of defects for obtaining perfect graphene structure. Since the production of larger scale GO is somewhat more controllable with a long history of success,[13,17,18,23,108] several researchers have been able to produce fairly large graphene sheets using a hydrazine reduction method.[19,20]

In the context of tribochemical processing, the combination of hydrazine's reduction of defect terminals (including edge defects) with the driving reaction of mechanochemically was expected to encourage the linking of graphitic lattices to "grow" sheets from the supplied graphite. Experimentally, this is accomplished by using $N_2H_4 \cdot H_2O$ as a medium (or lubricant) during the sliding of the graphite rod against the substrate. A 50 μL droplet of hydrazine hydrate was deposited onto the substrate immediately prior to the tribosynthesis procedure directly on the test area. As before, the combination of speed and loading in the tribochemical environment was evaluated for their efficacy. A test matrix of experiments performed with the use of hydrazine hydrate is listed in Table 6. In this table, the abbreviation "CTE" is used for "cycle-to-event," for which the test was run until an "event" occurred, representing a surface change. This will be discussed further in the results section.

Table 6. Testing matrix for $N_2H_4 \cdot H_2O$ experiments of graphite on Si.

Load / Speed	**1N**	**2N**	**3N**	**4N**	**5N**
0.25 cm/s			2cyc		
0.5 cm/s	CTE	CTE	2, 10, 100 cyc	CTE	CTE
1 cm/s	2cyc	2, 5cyc	2cyc	2cyc	2cyc
2 cm/s		2, 10, 50 cyc	2, 250cyc	2, 10, 50 cyc	
3 cm/s		2cyc		2cyc	
4 cm/s		2cyc		2cyc	
5 cm/s			2cyc		

3.1.4. Chemically Prepared Graphite Suspensions

Moreover, hydrazine hydrate solutions containing shaved graphite (obtained using a knife against a graphite rod) were prepared to test the chemical synthesis results without tribochemical influence. Additionally, select solutions were chosen to be evaluated as a medium for tribosynthesis. These suspensions were prepared starting with 0.015 wt% of shaved graphite in 10 mL of $N_2H_4 \cdot H_2O$. After this initial solution was prepared, a number of techniques were applied to evaluate their capability for producing CMGs. Table 7 describes the various synthesis methods including UV exposure, microwave irradiation, and mixing with Pt nanoparticles. Each sample was ultrasonicated (Branson, Bransonic 220) for 15min after completing the procedure and prior to analysis. For UV exposure, a Hg-Xe lamp (Newport) was operated at 260 W and the samples were placed directly in the collimated light path at a distance of 20 cm from the lamp source. A centrifuge (International Equipment Co.) was used to separate out the visibly large graphite flakes from the suspension so that the nanomaterials could be analyzed separately. For microwave synthesis, a 1020 W microwave (Goldstar) was used with the liquid suspension exposed for only a few seconds at a time to prevent boiling of the liquid. To obtain the final exposure time, the sample was repeatedly exposed for 2-3 seconds at 15-30 second intervals.

The UV-irradiated shaved graphite suspension (Sample UV1) was used as a tribosynthesis medium in both “wet” and “dry” conditions. This was performed to evaluate the influence of suspended graphite in the solution as opposed to relying on transfer of carbon material from the surface of the pin to the substrate.

Table 7. Chemi-synthesis of CMGs sample names and procedures

Step 1	Step 2	Step 3	Step 4	Step 5	Step 6	Sample Name
0.015 wt% graphite in 10mL $N_2H_4 \cdot H_2O$	Ultrasonicate for 24 hrs					S1
	UV exposure for 1 hr					UV1
		Centrifuge at 7000 rpm for 1 hr	Dilute in 10mL DI H_2O			CMG1
				Add in .5 mL Pt cube suspension		
					Microwave repeatedly for 2-3 s for a total of 20 times (~1min total)	CMG2*
					UV exposure (1 hr)	CMG3*

* Samples CMG2 and CMG3 are discussed in Appendix B as alternate reaction pathways

3.2. Characterization Techniques

In order to determine the nature of the resultant particles and films produced through the techniques discussed previously, a number of analysis and characterization methods were employed. To determine the morphology of the synthesized materials, various microscopic techniques were used to visualize the particle shapes and sizes. A digital microscope (Keyence) was used to image the surface conditions of the Si/Si_3N_4 substrates after the tribosynthesis procedures. This method allowed for the imaging of larger particles, particularly those which have thicknesses greater than ~10 nm where the light absorption of the layers created sufficient contrast for optical measurement. For

smaller particles, an AFM (PNI Nano-R) was used to observe nanomaterials on the surface, as well as determine the thicknesses of the larger materials observed in the digital microscope. In circumstances where sample quality required or allowed the use of a SEM, the surface was imaged using a Tescan Vega SEM, and in a few circumstances, a FEI Tecnai field-emission SEM (FE-SEM) was used to observe finer features.

In addition to surface evaluation, the liquid media used in the wet tribosynthesis procedures was collected. TEM analysis of the suspended particles was made possible by immersing a carbon coated copper (or nickel) TEM grid (SPI Supplies) in the collected liquid. Additionally, the chemically prepared CMGs were tested in the same way. Furthermore, in cases were enough liquid could be collected, UV-visible absorption spectra (Hitachi U-4100) were obtained to characterize the nature of the suspended particles.

In attempt to understand the structure and composition of the synthesized materials, Raman spectroscopy (Horiba Jobin-Yvon LabRam IR system using a 50x N.A. 0.55 objective (spot size: ~5μm) with a 633nm laser excitation) was used to identify the inelastic scattering due to phonons in the nanomaterial lattices, and was compared against standard samples such as plain Si, Si_3N_4, graphite (from the rubbing pin), and HOPG (highly oriented pyrolytic graphite).

For determining the chemical groups present on the surface of the samples in terms of the composition and functionality of the produced nanomaterials, X-ray Photo-electron Spectroscopy (XPS) was used to examine the electron binding energies for the

samples. These experiments were performed at the 8.2 beamline at Stanford Synchrotron Radiation Lightsource, which uses a synchrotron radiation source. The resulting spectra were processed to identify the peaks through Gauss-Lorentz curve fitting, so as to determine the nature of the chemical groups on the surface. CASAXPS was utilized to help identify the peak locations and optimize the fitting procedure. Additionally, a Shimadzu IRAffinity-1 Fourier Transform Infrared (FTIR) spectrometer was used to analyze a solution of suspended nanoparticles formed from the tribosynthesis procedure to help determine chemical groups present. In order to obtain a highly concentrated solution for FTIR measurement, the samples were cycled up to 10,000 times and the liquid media collected. DI water present in the liquid samples was then slowly boiled off by heating the solutions to 105°C, at which point the more concentrated solution was used for FTIR testing.

4. TRIBOCHEMICAL SYNTHESIS OF GRAPHENE-BASED NANOSTRUCTURES

This section discusses a novel nanofabrication process developed and optimized through this research. For the first time, tribo-nanofabrication was investigated in order to synthesize graphene-based nanostructures. Two approaches were used in this study. The first was using simple graphite abrasion as a control, while the second used optimized chemistry with hydrazine to enhance the process. Within the enhanced chemistry experiments, both a two-body and a 3-body friction approach were evaluated. Experimentally, a number of experiments were carried out in developing a method of tribochemically producing graphene and graphene-based materials, as described in the preceding section. The samples were evaluated using a variety of techniques to understand both the production and properties of the synthesized materials. This section addresses the findings of the various testing conditions, including the microscopy results, surface property results, and material spectroscopic characterization. The first section (4.1) looks specifically at the graphite abrasion experiments, whereas the following section (4.2) will describe the enhanced results through the use of hydrazine.

4.1. Graphite Abrasion

Using a pristine graphite rod for rubbing on silicon or silicon nitride served as a foundational result that shows the simple result of rubbing graphitic material in a tribological environment. This will be used as a control for comparison with the other test methods employed.

4.1.1. Surface Visualization of Tribo-synthesis Products

As a primary means of identifying the production of nanomaterials, various microscopy techniques were used to locate and measure the size of the produced materials. The following sections present the results of imaging with digital, scanning electron, and atomic force microscopy.

In the case of the direct rubbing of graphite onto Si, the observation of transferred material was not recognizable with digital microscopy. However, the application of moisture to the surface revealed deposited material by means of the beading of water on the hydrophobic SiO_2 surface, whereas the test area of the sample exhibiting hydrophilicity as a result of deposited graphite. More specifically, oxygenated graphite terminals – or Graphite oxide – produces the hydrophilic effect, rather than the graphite itself which, like SiO_2, is also hydrophobic.[109,110] In order to see more clearly the nature of the deposited graphite, the samples were examined in a SEM for which a couple sample images are shown in Figure 13. Although this lower resolution SEM did not provide sufficient resolution and contrast to image the precise morphology of the deposited material, it was possible to see the test area with varying coverage depending on the test conditions. In Figure 13, the 2-cycle sample shows a mixture of debris particles in addition to streaks running in the direction of the graphite rod's sliding path (indicated by the arrows). In the case of the 50-cycle test, the image shows a much higher contrast in the streaks, indicating a thicker deposition on the surface.

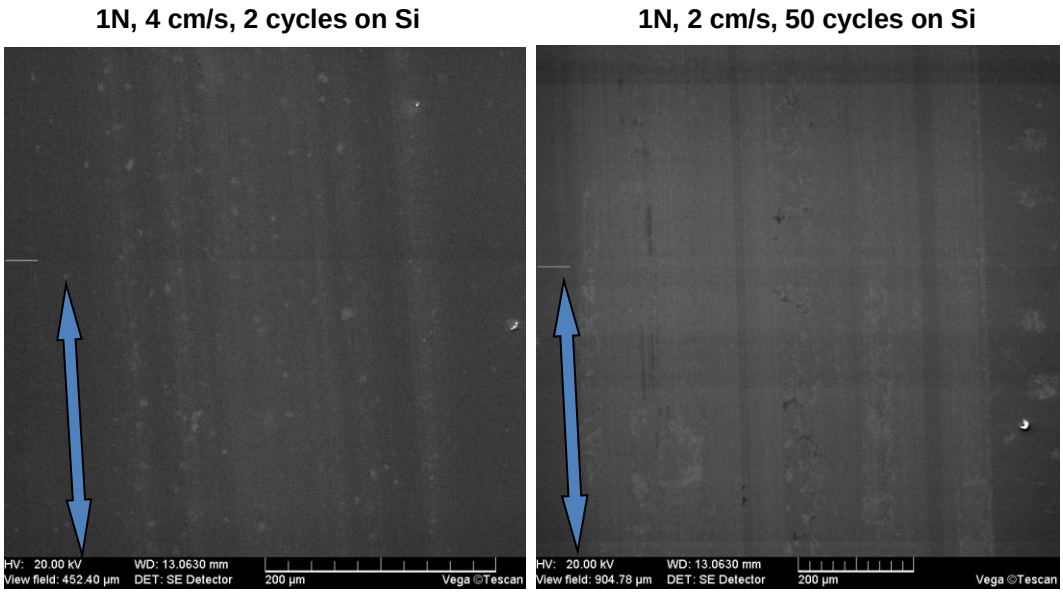

Figure 13. SEM imaging of sample surface for graphite rubbed on Si for two test cases

In order to verify that in fact the streaks were deposited material and not scratches on the surface, AFM scans of the surface were performed. In scanning, the height of the features in the test area was small, but did indeed reveal that the material was debris from the graphite rod and not wear of the Si substrate. Using lateral force mode of the AFM allowed for the most finely resolved images of the deposited material, as shown in Figure 14. As seen in the image, one "streak" seen in the earlier SEM images was approximately 4 µm wide and less than 6 nm tall, but consisted of finely distributed particles that were not obviously connected. This is consistent with graphitic debris produced from rubbing without any additional reactions taking place.

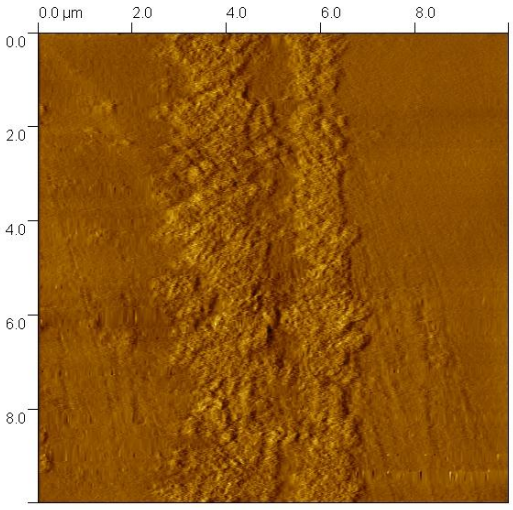

Figure 14. Lateral force microscope (LFM) image of deposited graphite on Si surface with height less than 6nm.

Although the debris apparently was a random collection of graphite, the test matrix was evaluated to examine the influence of load and speed conditions during the tribo-synthesis procedure. Specifically, the amount of deposited material was estimated using LFM to identify the amount of surface coverage by the graphite. Figure 15 depicts an example of 1N tests ran under various maximum speed conditions, as indicated in the images. The contrast variation seen in the intensity of the images is the result of occasional formation of a water meniscus between the AFM probe tip and the sample surface, as has been commonly observed in previous works.[111] This sample is particularly susceptible to this imaging artifact due to the hydrophilic nature of the deposited graphite (with oxide defects) on the sample and the common humid conditions in southeast Texas.

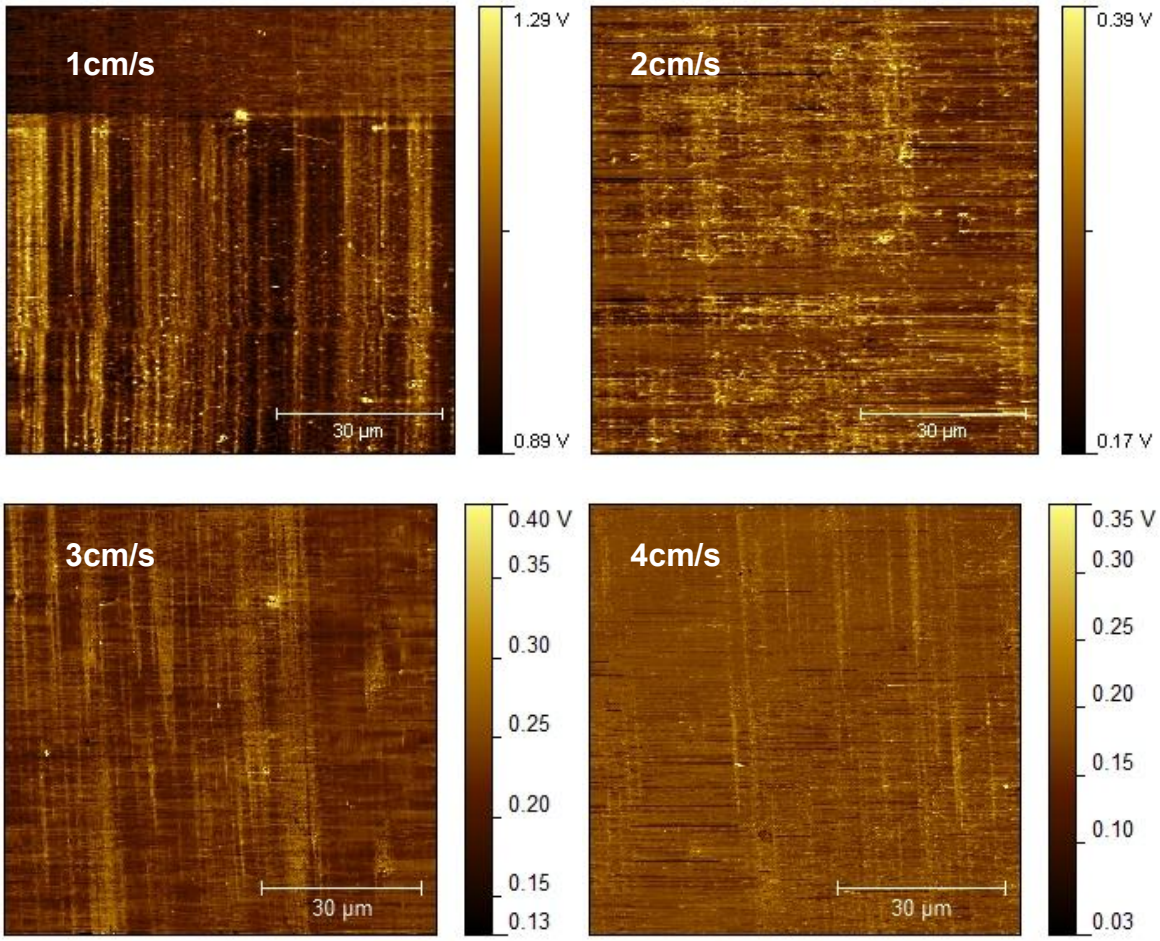

Figure 15. LFM images of graphite deposited on Si for 1N load under varying speed conditions (labeled on images).

The various load and speed conditions were examined and the surface area coverage (in percent of total area) was estimated by using Gwyddion scanning probe imaging software by determining a threshold value in the LFM friction image and calculating the area of the graphite deposited on the surface. The results were then charted for each loading condition versus the maximum sliding speed for two locations in the wear track – near the end of the wear track (at the apex of the reciprocating motion

where the sliding speed is close to zero) and at the center of the track (where the sliding speed equals the maximum speed). These charts are presented in Figure 16 and Figure 17, respectively.

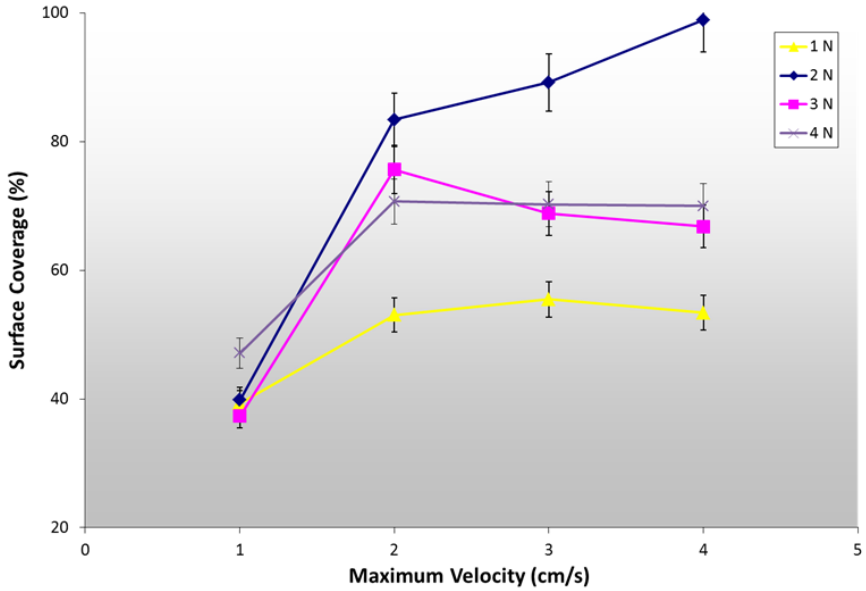

Figure 16. Surface coverage at the bottom of the wear track (near the apex of the reciprocating motion) of graphite on Si resulting from tribo-experiments

As seen in the figures, the surface coverage at the bottom of the track increases with increasing maximum speed irrespective of the loading condition, while at the center, it is not clearly linked to the velocity, with the exception of perhaps the 1N and 4N loads which depict opposite trends of decreasing or increasing with speed, respectively. Additionally, at the end of the test area, the coverage loosely scales with load, particularly above 2cm/s maximum speed, whereas the center of the track again

showed no correlation. These results indicate that the deposition of graphite material is more sensitive to shear rate than pure shear force or shear speed, since the correlation is much stronger at the end of the track where the pin speed is coming to halt before changing direction and accelerating to the maximum speed condition.

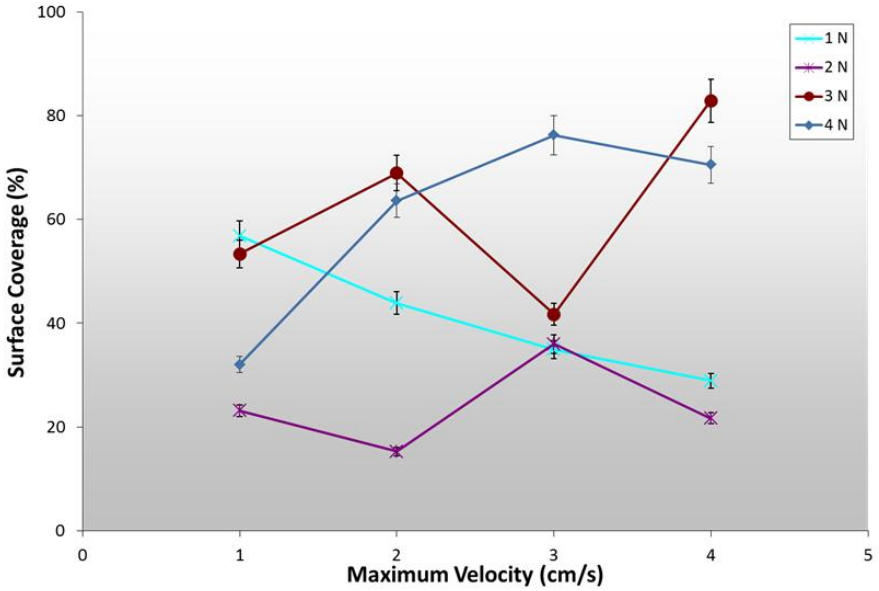

Figure 17. Surface coverage at the center of the wear track (sliding speed equal to max velocity) of graphite on Si resulting from tribo-experiments

4.1.2. Surface Characterization of Graphite Abrasion Experiments

In order to precisely define the material as abraded graphite, a number of characterization techniques were employed to better understand its nature. The following sections discuss the friction behavior of the samples during sliding as well as the spectroscopic information related to the deposited materials.

4.1.2.1. Friction Characterization of Experiments and Debris

As discussed in an earlier section, the use of the tribometer not only allows for precise control over the tribosynthesis test parameters, but also allows for an in situ monitoring of the surface condition, based on its frictional response. This is illustrated in Figure 18, where two cycles of various 1N loading procedures are depicted. In this image, it is notable to mention that the friction slightly increases with distance, but stays relatively constant over the sliding path length. This is consistent with contact theory that explains that the friction coefficient is independent of sliding speed.

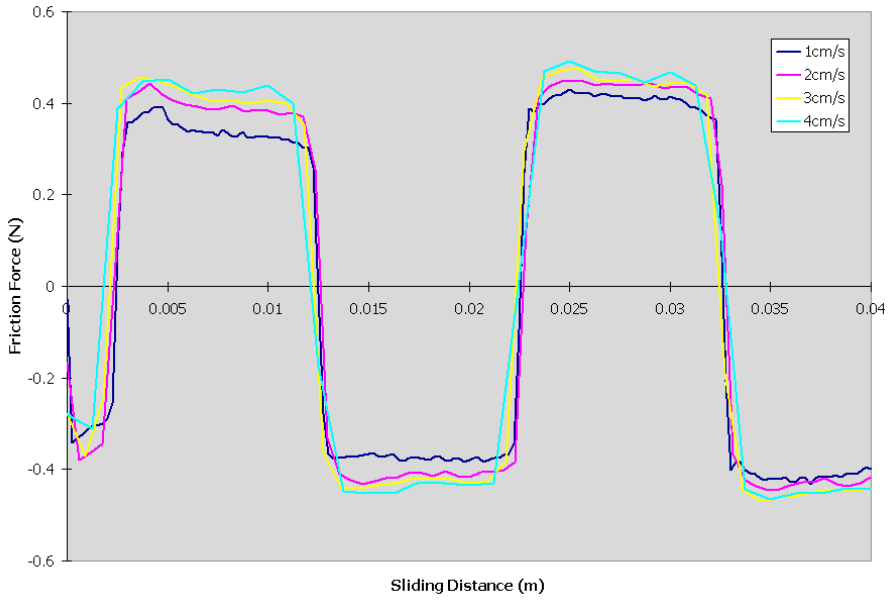

Figure 18. Friction behavior of graphite sliding on Si under 1N load for various sliding speeds

Additionally, we notice that over a longer cycling period, like that shown in Figure 19, the friction coefficient stabilizes quickly and remains constant indefinitely.

This will be important as we look at later samples. The sharp oscillation in the friction results is an artifact of the reciprocating sliding motion that results from taking the absolute values of the negative coefficients (from the return travel during the forward and backward sequence) and averaging of data collected when the pin changes directions (when the coefficient alternates between positive and negative values). This results in little dips in the curve twice per cycle.

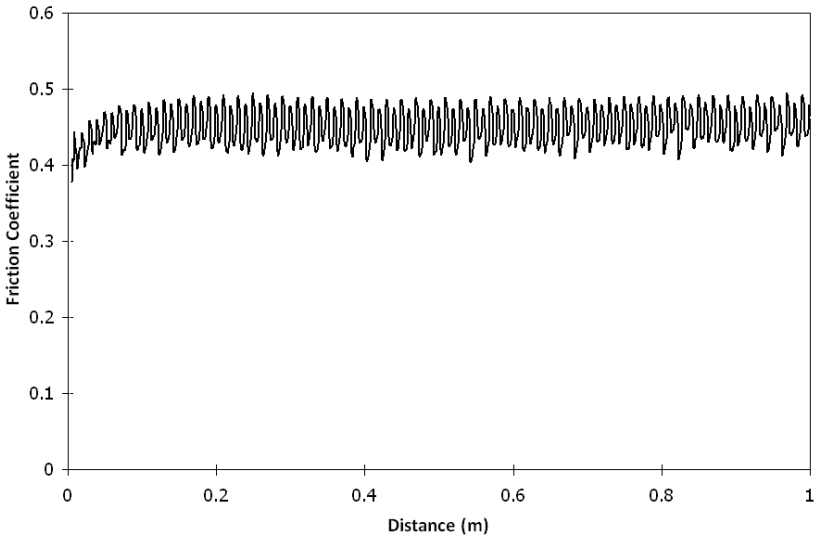

Figure 19. 50 cycle friction behavior for 1N load at max speed of 2cm/s

If the array of test data is examined for variations in the friction coefficient, as shown in Figure 20, it is observed that the lower loading conditions exhibit a larger friction coefficient, particularly at faster sliding speeds. This can best be attributed to the presence and removal of small surface asperities on the graphite pin as the tests were

conducted, particularly since the tests were performed in order of increasing loading condition. This was performed purposely in this manner to incrementally monitor the test configuration in order to avoid cracking either the pin or Si substrate, which are both brittle materials. In essence, the 3N and 4N loading conditions represent the uniform sliding condition of the pin on the surface. Here, very little variation is seen, and an average friction coefficient of ~0.35-0.45 can be attributed to the frictional interaction of dry graphite on Si. For further test results regarding the friction coefficients from the control experiments, please refer to Appendix A: Tribosynthesis Supplemental Data.

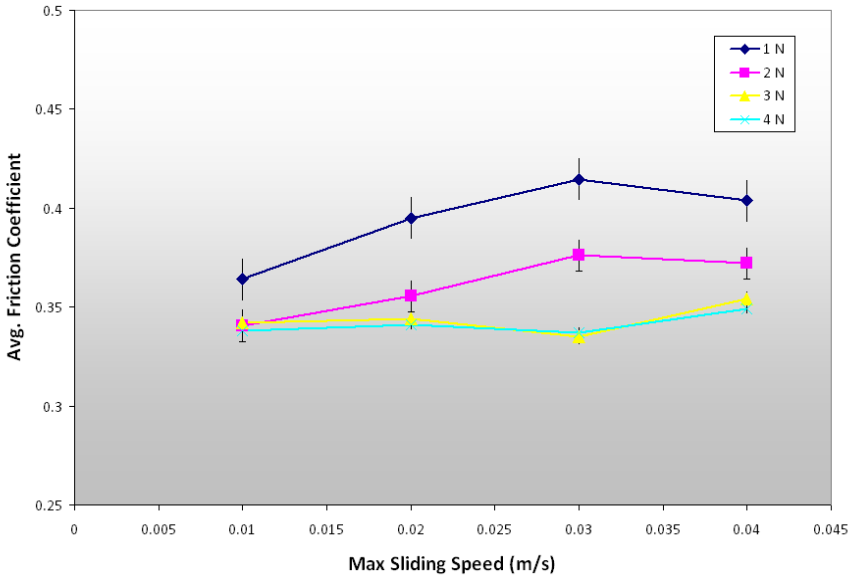

Figure 20. Average friction coefficient observed during tribo-experiments between graphite and Si for various load and speed conditions

4.1.2.2. Characterization of Surface Material

To best understand the nature of the abraded graphite on the substrate, Raman spectroscopy was used to study the graphitic phonon resonance resulting from laser excitation using a 633nm wavelength laser. The nice thing about graphitic materials is that they possess a clearly defined Raman signature resulting from the vibrational modes in its hexagonally arranged molecular structure. As such, it has a primary peak, often called the "G-band" (for graphitic) in the range of 1570-1605 cm^{-1} depending on the energy of the incident light.[112,113] Furthermore, lamellar graphite (or bulk graphite) shows this primary peak typically in the lower end of this range (often quoted at 1580cm^{-1}),[112] but single-layer graphene shows a peak shift to at the higher end as a result of the atomic planes not being vibrationally coupled to surrounding layers.[114] Using a 2.33 eV excitation, D. Graf et al.[114] observed a G-band peak at up to 1587 cm^{-1}, whereas Hulman et al.[115] observed the peak at 1590 cm^{-1} when using a similar 633 nm laser (1.9 eV) as in this experiment. Additionally, in strong signals, a second order vibrational response is able to related the number of layers specifically to the amount of Raman shift observed in the 2500-2800cm^{-1} range (called the G' band or occasionally the 2D or D* band).[113,116] The Raman spectra of graphite also can determine the quality of graphitic material through the analysis of the D-band (for disorder) that arises from edge effects on graphene planes and functional groups on the surface of the graphite that alter its phonon response.[112] This peak in the 1300-1400 cm^{-1} range also can be used to determine crystallite size of graphenes and carbon nanotubes when compared against the G-band peak.[112,117]

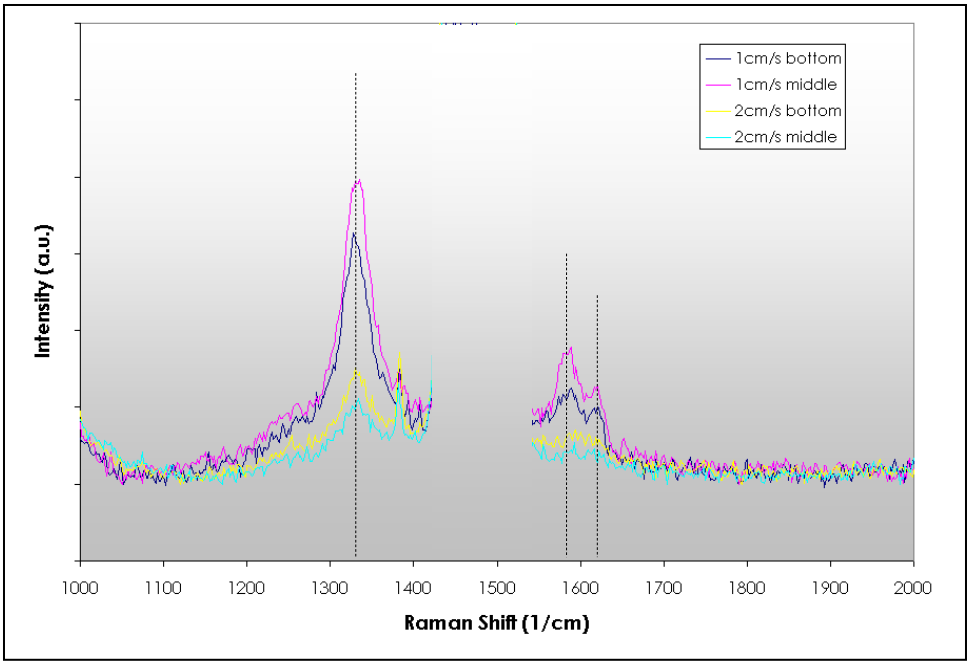

Figure 21. Raman spectra of D and G bands of graphite observed in wear tracks of tribo-control experiments.

When looking at the debris on the sliding path of the graphite on Si, the D and G bands were quickly identified, particularly for areas where there were significant amounts of debris on the surface. As seen in Figure 21, clear D band peaks of roughly twice the intensity of the G peaks were observed at 1333 cm^{-1} and 1588 cm^{-1}, respectively. Additionally, a small peak at 1620 cm^{-1} was also observed which corresponds to what is known as the D′ peak,[118] which only appears in instances of extremely small crystallite sizes where the intensity of the D peak is much more than the G peak.[113] This is due to the relative strength of edge effects as compared to the graphitic vibrations. This indicates the likely presence of nano-sized graphenes as predicted by Geim and Kim,[104] but at that size, their usefulness is very limited.

When looking more closely at the intensities of the G-band, D-band and D′ peaks as a function of the sliding condition (Figure 22) we see a decrease in all cases as the sliding speed increases. As all decrease in the same magnitude, and no relative differences arise, the decrease is more likely derived from reduced debris on the samples rather than any physical change in the graphitic structures. This is also supported by the fact that stronger signals exist in the ends of the sliding path as compared to the middle, where the shear rate is constant and less graphitic debris is left behind, reiterating the AFM results reported in Figure 16 and Figure 17. As it is, the ratio of the D to the G peak intensity is consistently ~2.4, irrespective of the processing conditions. Taking the empirically fit relationship between crystallite size, laser energy, and ratio of D and G intensities according to Sato et al.,[117] the expected crystallite size is around 35-40 nm, which corresponds well with the debris seen in AFM imaging. This also explains the appearance of the D′ peaks, which indicate the disorder discussed by Pimenta, et al.[113]

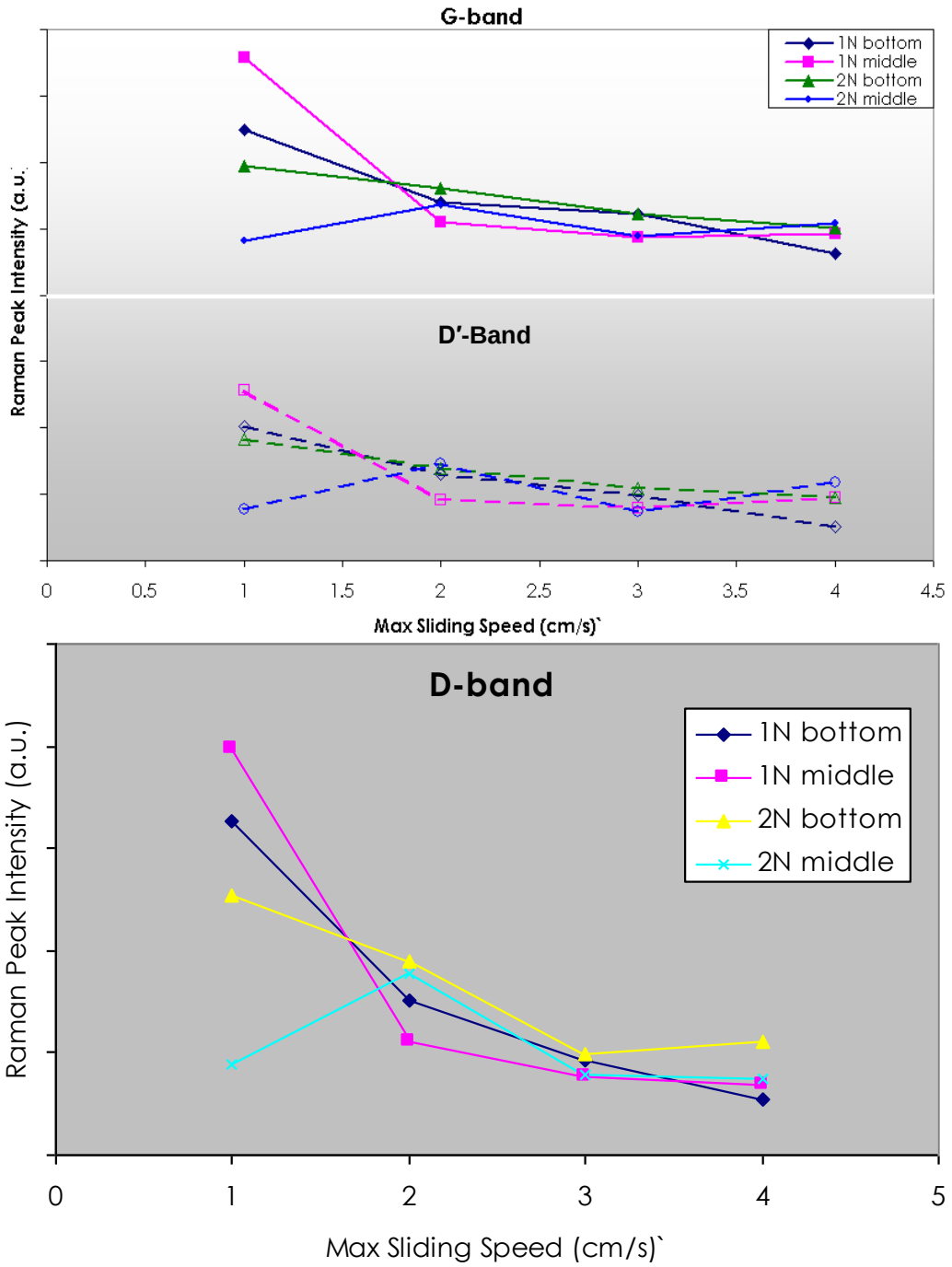

Figure 22. Relative intensity of G-band (top), D-band (bottom) and D′ (middle) peaks for low load conditions.

As a verification of the quality of the graphite used in the rubbing experiments, and also to prove that the rubbing pin did not consist of large graphitic platelets, the Graphite rod was compared to highly oriented pyrolytic graphite (HOPG) using x-ray diffraction (XRD) as shown in Figure 23. Here, it is seen that both possess the primary diffraction angles reported for graphite (indicated by the vertical lines), and the first peak at $2\theta=26.6°$ corresponds to the interlayer distance between the (002) atomic planes. It is important to note that the rod peaks are broader and do not exhibit all the smaller peaks observed in HOPG. This is due to the fact that the graphite rod is not highly ordered like the HOPG and as such lacks the strong intensities of the higher order peaks. This explains that while the graphite rod does in fact consist of randomly oriented graphite crystallites, they are likely small in nature, and not oriented in any particular manner. This helps to explain that the graphitic material observed in the control tests was not necessarily any unique formation, but rather the simple wear of graphite platelets onto the Si substrate. While probable that individual graphenes did also appear on the surface, it is almost impossible to identify their precise location, or whether their formation is influenced by the tribo-processing parameters. As such, it can be assumed that the material is simply abraded graphite.

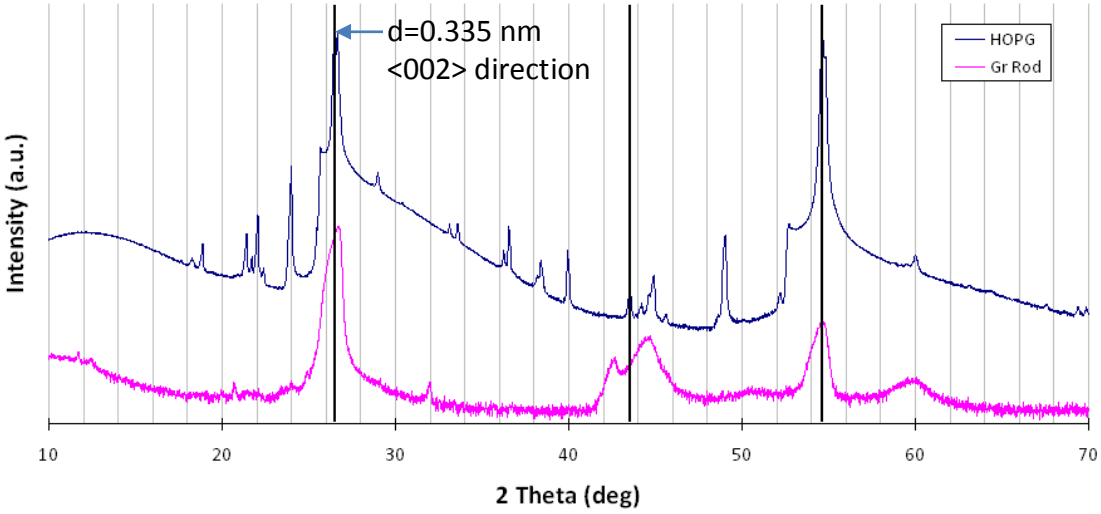

Figure 23. XRD of HOPG and graphite rod used for experiments. Vertical lines represent primary diffraction angles for graphite lattice.

4.2. Chemically Enhanced Tribosynthesis with Hydrazine

Having observed the simple wear of graphite debris from the graphite rod in the control experiments, obviously chemical manipulation is required to enable the formation of graphene and related materials. This section discusses the results obtained through the test matrix performed using hydrazine hydrate, a known reducing agent for the preparation of graphenes, in conjunction with the tribo-synthesis procedure. It was noticed nearly immediately that a drastic difference existed from the control experiments from everything including friction results to the microscopy images. These results are discussed below.

4.2.1. Two-body Tribosynthesis in Pristine $N_2H_4 \cdot H_2O$

Much like the control experiments in which the product of the tribo-synthesis procedure were not visible on the surface of the Si, so was the samples tested with

$N_2H_4 \cdot H_2O$, with the exception that the liquid left behind a residue that occasionally prohibited the viewing of the test area. However, the test area could still be located by the application of humidity to the surface, by which the liquid would adhere to the hydrophilic graphite material and reveal the striations resulting from the sliding procedure. Unlike the control experiments, the amount of debris formed from the tribosynthesis procedure was almost zero as the liquid served as a lubricating medium and reduced the average friction coefficient as compared to the dry sliding. In fact, the friction mapping of the tests in hydrazine hydrate all showed a characteristic decomposition from an initial friction coefficient near 0.15 (compare to 0.35 without the liquid medium) to a much lower value near 0.05 after sufficient number of cycles (more details in a later section). This is illustrated in Figure 24, where the friction coefficient is plotted versus the sliding distance (or equivalently, time and cycles). The colored and dashed lines in this chart represent specific positions in the sliding path for which the rate of change from the initial friction to the final coefficient value differed from one another. The fastest location (red line) to exhibit the friction decomposition was at -3 mm inside the 10 mm (+/- 5mm) path length, which corresponds to the starting position of the graphite pin. The yellow line represents the second region which was a mirrored, but slightly offset, location at the other end of the sliding length at +2.5mm. The green line represents the transition of the friction at the center of the track where the sliding velocity is equivalent to the max speed, or in this case, 2cm/s. The slowest region to transition to the lower friction coefficient – represented by the blue line – was the apex

of the sliding path where the pin comes to a stop and changes directions during its reciprocating motion.

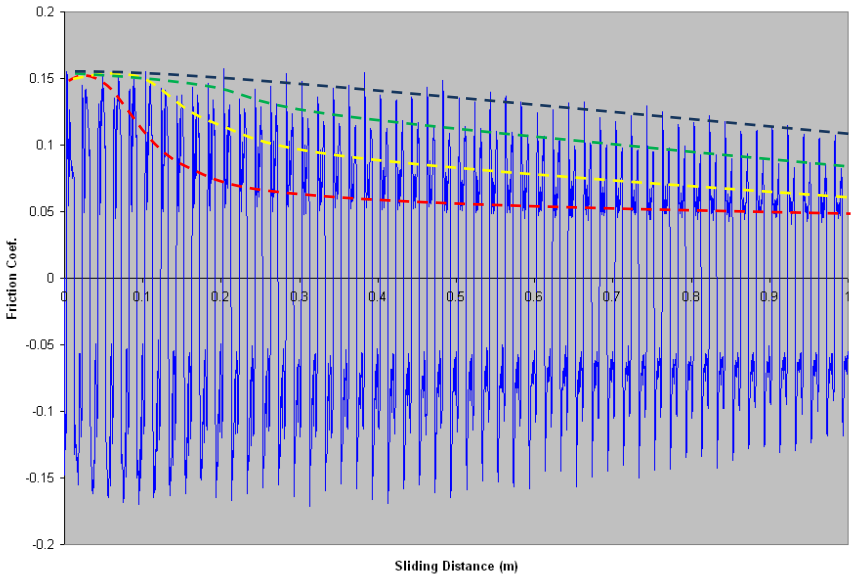

Figure 24. Friction reduction due to tribochemical reaction of surface during 50cycle test with 2N at a max speed of 2cm/s. Dashed lines show the progression of various parts of the sliding path to transition to lower friction.

This data is represented differently in Figure 25, where the friction coefficient is plotted against the position of the sliding path. The arrows on the chart describes the progression of the data during the tribosynthesis cycling. I.e. one cycle of the tribo-procedure is represented by a clockwise path in the data, for which a narrowing of the "circular" pattern represents a decrease in friction coefficient over the cycling periods. The pattern or gradient of the lines between cycles helps to show the rate at which the friction coefficient is changing, much like a topographic map shows the elevation of a

landscape on a 2-D map. Additionally, this chart helps to demonstrate that the friction coefficient is location dependent, despite having a uniform Si surface and loading condition.

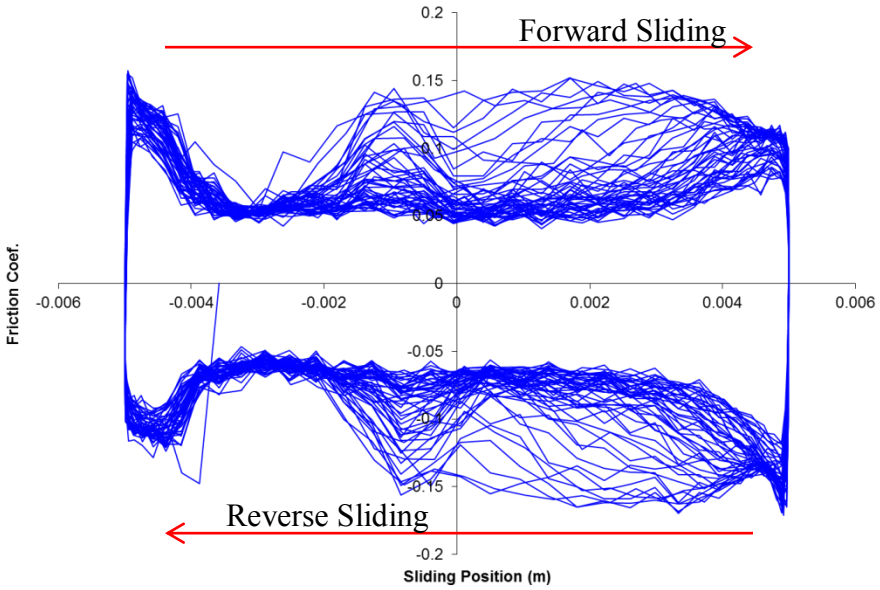

Figure 25. Friction coefficient as a function of sliding position for 2N, 2cm/s, 500 cycle in $N_2H_4 \cdot H_2O$. Arrows indicate motion/direction of tribometer.

Alternatively, in the case of an increased load on the sliding pin, the transformation to the lower friction value is almost immediate. As shown in Figure 26 and Figure 27, the same processing conditions, though with twice the load, were found to reduce the friction to the ~0.05 value within the first 10 cycles. This transition seen in both of these examples (and many others not shown here) could indicate: (1) stabilization of the friction value after wearing the surface and the pin into constant contact geometry, (2) formation of some interfacial material to change the surface

properties, or (3) some chemical change in the liquid medium resulting in better lubrication. Based on examination of the surfaces which shown no obvious wear, either of the latter two are more likely.

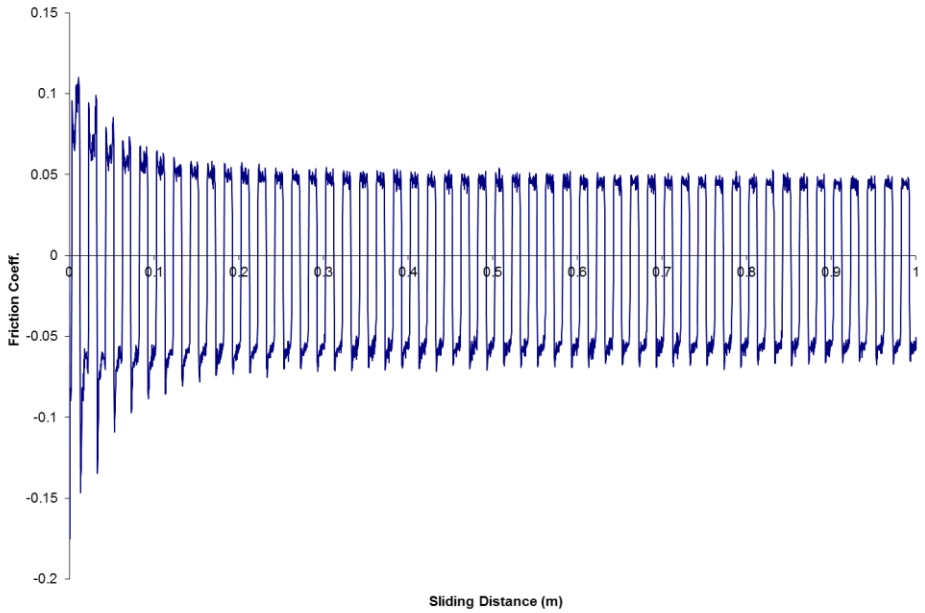

Figure 26. 4N, 2cm/s, 50 cycle in $N_2H_4 \cdot H_2O$. Faster reduction in friction.

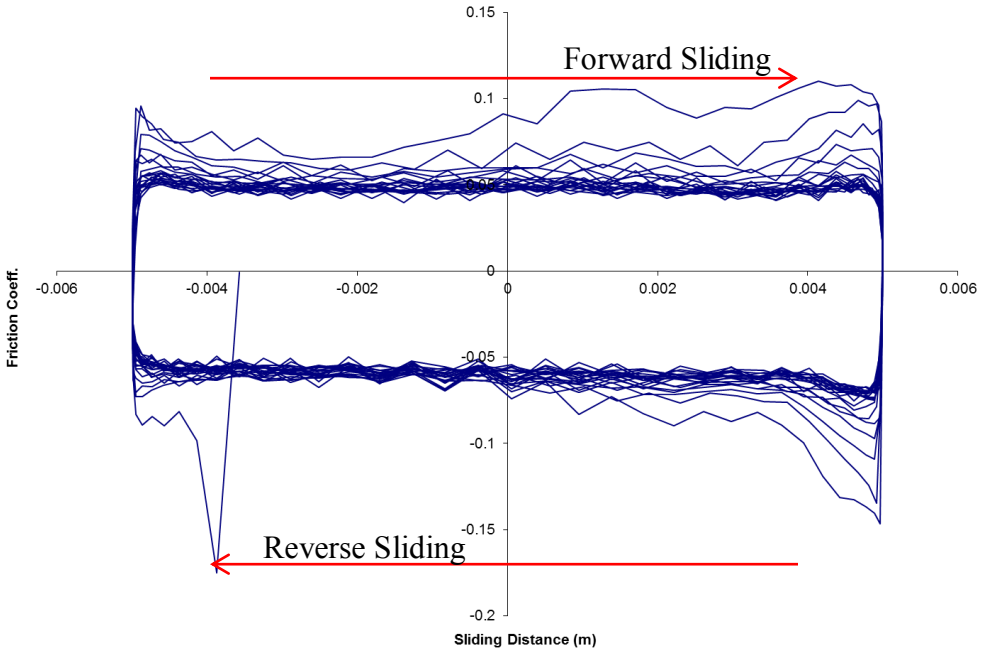

Figure 27. Corresponding 4N, 2cm/s, 500 cycle friction map as a function of sliding position. Notice near complete decomposition by end of first cycle.

This intriguing behavior by the friction coefficient actually provides valuable information regarding the interface of the graphite pin and the substrate. This friction-monitoring with the tribometer allows for the determination of a surface reaction by observing significant changes in coefficient of friction. This sort of behavior has been observed in many instances where a tribofilm[90] forms during wear processes, notably in the formation of low-friction coatings from the formation of MoS_2 from MoDTC.[118] Additionally, the reduction of friction may indicate the presence of graphitic compounds separating from the pin and serving as an additional solid lubricant which has been used in various lubricants for enhanced friction reduction.[119]

In order to determine the nature of the surface condition, various microscopic techniques were used to evaluate the product of the tribosynthesis procedures.

Using the FE-SEM, a 4N tribosynthesis test on Si revealed the formation of regularly ordered and sized circular shapes on the surface of the sliding area. These shapes were just barely visible in the SEM due to their extreme thinness on the surface of the silicon as shown in Figure 28. The size of these shapes was approximately 5μm in diameter and surprisingly uniform across the surface. This is a stark contrast to the debris seen on the surface in the control samples as shown in Figure 13 – Figure 15, which appeared to be primarily abraded graphite material from the pin onto the substrate. In these images, a controlled production of uniform thin materials is observed in the test area, suggesting a chemical product of the tribosynthesis procedure. This also verifies the 2nd hypothesis that the surface condition was altered through the generation of a film, albeit a non-continuous one, as a product of the tribosynthesis procedure. The generation of these interfacial materials explain the reduction in friction coefficient, and furthermore, while the 1st and 3rd hypotheses may also be occurring, it can be assured that their effect is negligible. This is proven by the fact that the friction decomposition seen in Figure 25 is not spatially uniform which indicates a surface effect rather than a contact area or lubrication effect. As an additional note, the dark spots in the images are small pits that have begun to form in the Si during the cyclic loading during the 50 cycle processing.

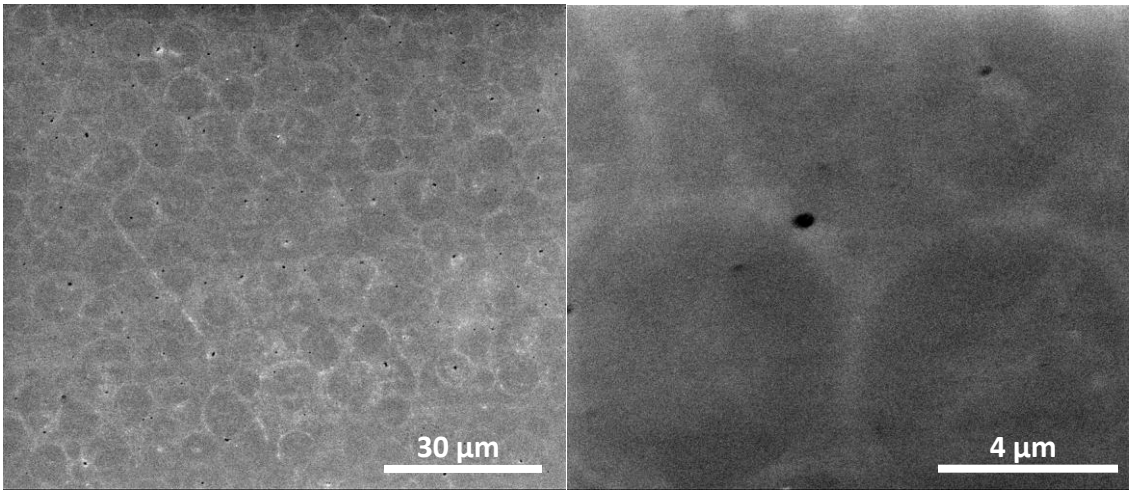

Figure 28. 4N lubricated with hydrazine hydrate FE-SEM images 1cm/s (left) same sample at higher magnification (right)

As illustrated through the poor resolution available by SEM for determining the characteristics of the shapes observed in the test area, the samples were evaluated using the AFM to determine their precise morphology. As illustrated in Figure 29, the AFM could easily identify the flakes on the surface of the substrate in close-contact mode, where the phase image (on right) highlights the presence of these materials. Furthermore, using the height scan, the flakes were found to be of a general thickness of ~2 nm which is consistent with graphite oxide flakes, reported to be 1-2nm in thickness.[120]

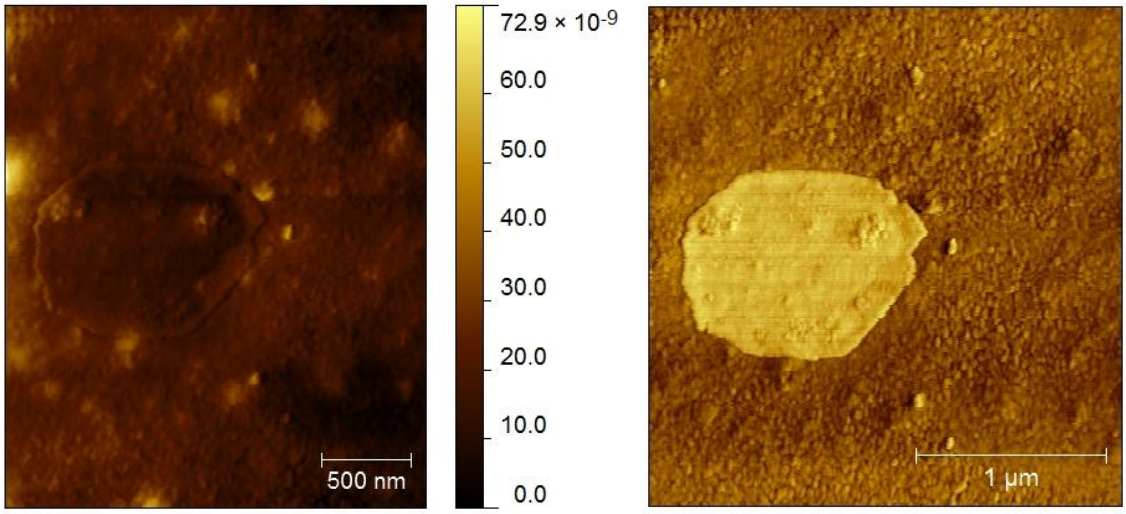

Figure 29. ~2nm thick flake resulting from testing with 1N, 0.5cm/s, 130 cycles on Si. Left image: shaded height scan, Right image: phase image.

4.2.1.1. Cycle-to-Event Testing

In order to properly understand how the frictional decomposition is linked to the formation of these interfacial materials, a number of tribosynthesis investigations were performed by specifically testing various loading conditions and cycling until the decomposition was observed. This CTE testing was tested with 1-5 N loads with 1 N increments, and specifically with a maximum sliding speed of 0.5cm/s. After testing, each sample was analyzed for the presence of the flake-like particles, which were measured by AFM. Figure 30 represents one of these AFM scans used to locate and measure the size of the resulting flakes, for statistical categorization.

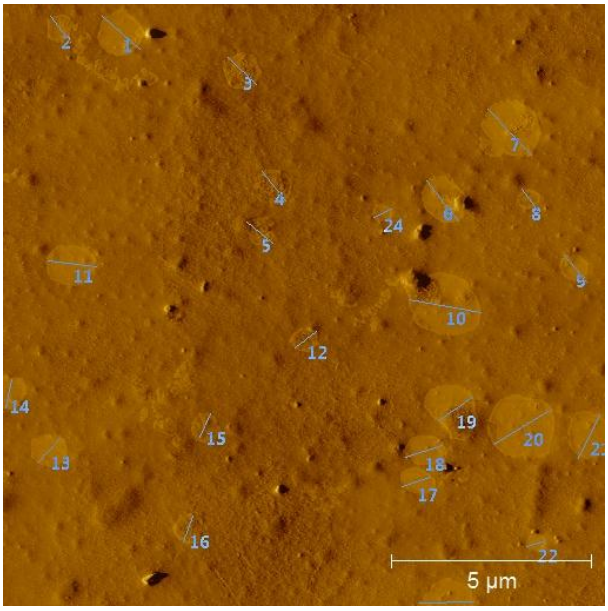

Figure 30. Identification (on phase image) and quantification of flakes produced on 1N, 0.5cm/s on Si CTE condition.

Likewise, the AFM scans were useful in determining the thickness dimensions as illustrated in Figure 31 during a 2N CTE test. The height profile of the line drawn across one of the flakes in the top image is shown in the bottom chart, which shows an average height or thickness of 2.5 nm, which was a characteristic dimension of the flakes formed from the tribosynthesis process in hydrazine hydrate. No matter what load or speed conditions were tested, the formations were nearly always in the range of 2-3nm tall. In certain instances where several flakes were present on the surface, their overlapping often led to dimensions of multiples of this characteristic thickness due to multiple layers. For instance, double layers would appear as 5-6nm thick; triple layers would measure around 8nm, and so on. More commonly for CTE testing in hydrazine hydrate, however, was to find the single layers as seen in the following figures.

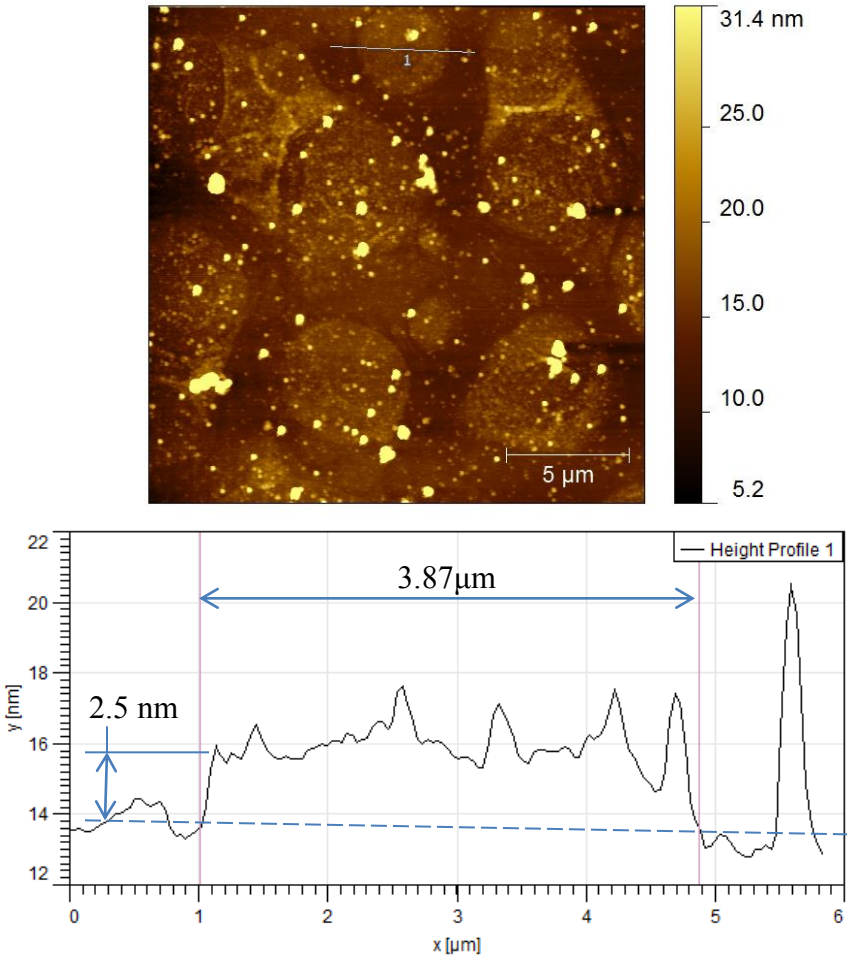

Figure 31. Height image (top) of flakes formed from 2N CTE trial. Height profile 1 (bottom) of flake in top image showing dimensions.

Similar flake formations are observed in all loading conditions when performing CTE tribosynthesis. As seen in Figure 32, the 3N and 5N loading conditions also exhibited similar featured flake formations, although larger in lateral dimension, and in varying concentration on the surface. These formations very closely resemble functionalized graphenes reported by Woresly, et al. who looked at arriving at graphenes through chemical modification of sp^3 graphite fluoride using alkyl lithium reagents.[121]

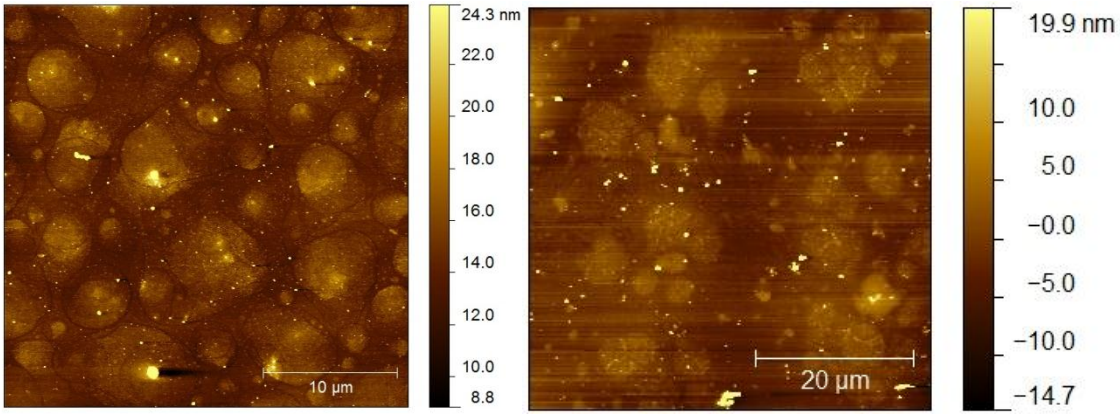

Figure 32. CTE surface for 3N (left) and 5N (right).

To identify the correlation between the size (lateral dimension represented by an approximate diameter) and the processing condition, the statistics were obtained using the measuring tool in Gwyddion's AFM image processing program. These values were plotted against the average contact pressure under the graphite pin, which is shown in Figure 33. Additionally, all the measured particle sizes are presented as the blue dots surrounding the red squares which represent the average particle diameter with an associated standard deviation represented by the error bars in the figure. The scatter in the data can be attributed to the local pressure differences due to asperities on the surface of the graphite pin that lead to difference in local diameters. Even so, the average diameters of the particles showed an extremely reliable relationship to the contact pressure. The size can be thus predicted through a logarithmic relationship represented by the equation of best fit in the chart. Or with the appropriate terminology:

$$D_p = 2.3ln(P_{ave}) - 3.2$$

where D_p is the particle diameter in the lateral dimension, and P_{ave} is the average contact pressure. The error bars in the chart represent the standard deviation of the particle size which also shows a slight increase with increased contact pressure. Note that the model crosses axis (Zero-point) at ~4 MPa.

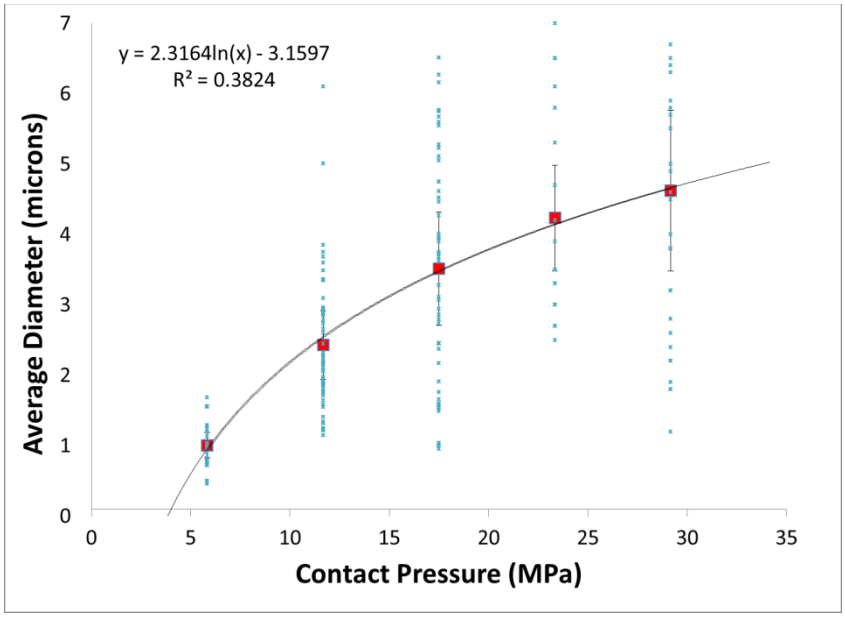

Figure 33. Statistics of average particle formation diameters with respect to average contact pressure in CTE samples having 0.5cm/s maximum velocity condition.

To understand the nature of the formation process, the images from the CTE tests were also evaluated for the number concentration (spatial density) of formations on the surface and their respective surface coverage. This data is presented in Figure 34. For both cases, it is observed that a peak in the occurrence and coverage of the platelets on the surface near 2N or 12MPa. This evidences that the spatial density and surface

coverage is both related to the inversely to the load and proportionally to the size (which is expected), which is logarithmically related to the load. Thus, in mathematical terms,

$$\rho_{spatial} \propto \varphi \propto \frac{\ln(P)}{P}$$

where ρ is the spatial density and φ is the surface coverage.

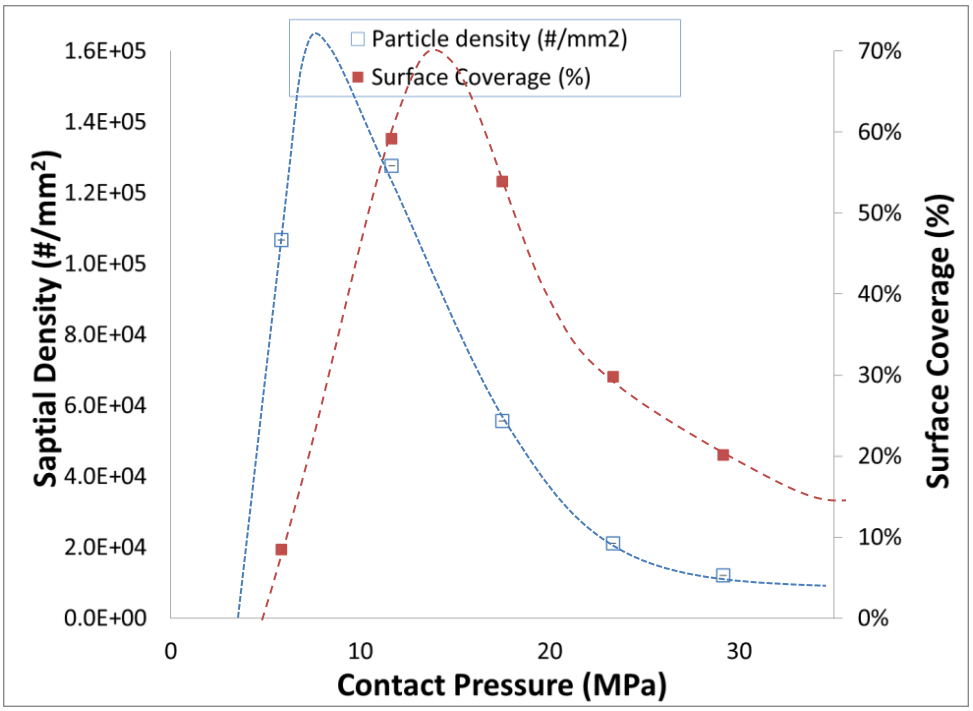

Figure 34. Spatial density and surface coverage statistics for formations of particles on surface for CTE testing. Dashed lines are representative ln(x)/x relationship.

As an additional note, in the 1N and 2N loading conditions, the surface of the silicon was often covered with a thin layer of material from which the flake formations appeared to form. This is noticeable when comparing the surrounding surfaces in Figure 29 and Figure 31, and seeing the relative smoothness in the substrate (indicative of the

Si, the bumps are more obviously debris than a surface roughness condition) in Figure 31 as opposed to the more randomly textured surface in Figure 29. In Figure 35 the circular formations are actually depressions in the thin layer, which indicates that the flakes may have formed in this film layer then are removed and re-deposited in a new location. Additionally, the peaks in the centers of these depressions suggest that during the formation process, the material migrates within the film towards a contact stress concentration. It is believed that these films are not observed in the higher load tests, due to "scrubbing" of the surface that helps to keep the surface free of this deposited thin film, while still forming the flakes in a dynamic manner.

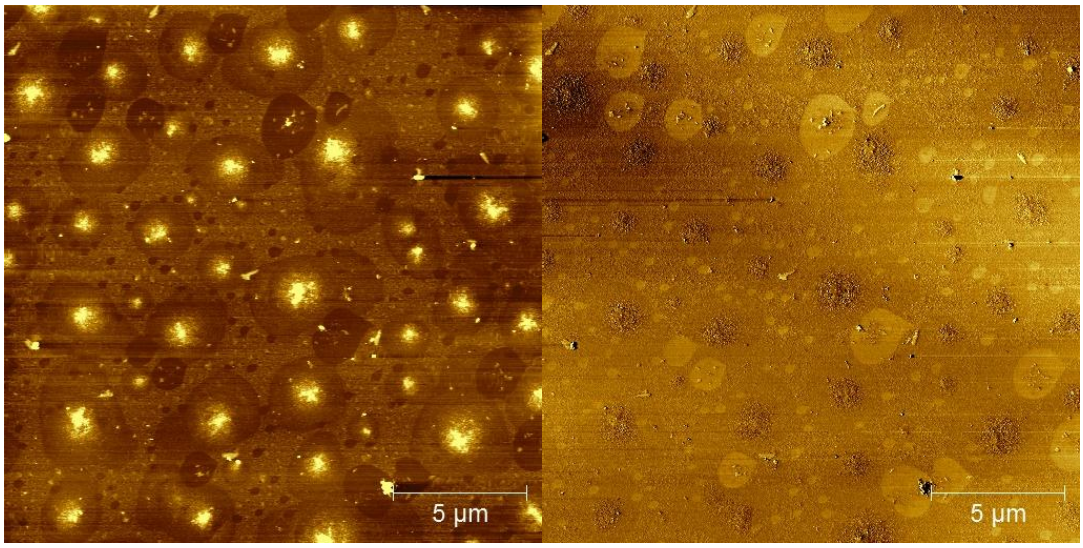

Figure 35. Height (left) and phase (right) images of formations in 2N CTE trial.

This also points out the balance required between generating the particles on the surface and forcefully removing them through wear related processes. At larger loading

conditions, the particles will still form and with larger sizes, but the deposition of the flakes onto the substrate will be hindered by the mechanical removal by the pin scraping the surface.

In an effort to develop higher contact pressures without increasing the average load that would result in removal of material, a form of three-body abrasion was used to concentrate stresses on the surface.

4.2.2. Three-body Tribo-environment with Shaved Graphite in $N_2H_4 \cdot H_2O$

Three-body contact was accomplished via adding shaved graphite into hydrazine hydrate liquid medium prior to testing. As presented in Table 7, sample S1 corresponds to the liquid suspension used in these tests. The graphite was prepared in a powder such that the size of the particles in the liquid medium was on the order of 100nm. Larger particles settled out of the solution and were discarded. Tests using this medium were performed on both Si and Si_3N_4, with tests using the solution as a liquid media ("wet") and allowing the liquid to dry on the surface of the substrate prior to the tribosynthesis experiment ("dry").

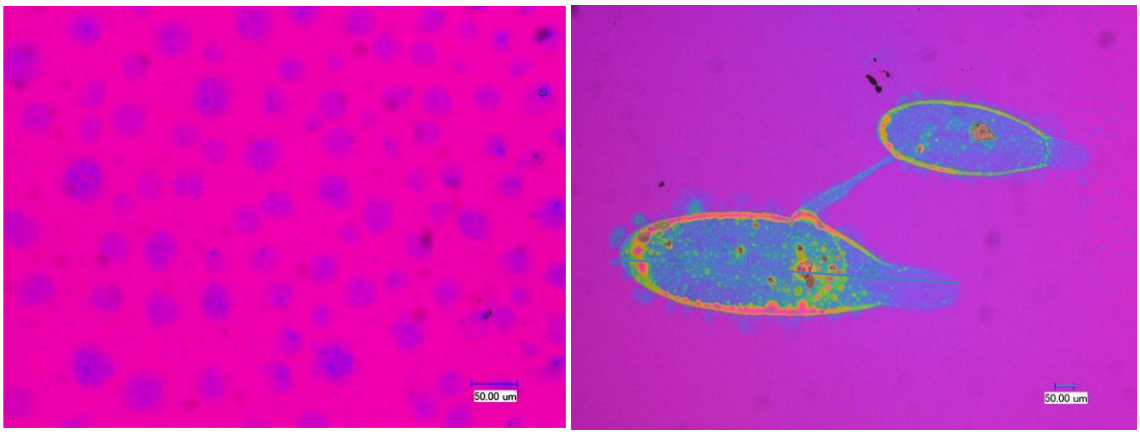

Figure 36. Digital microscope images of flake formation on Si_3N_4 on test areas from 2N, 2cm/s, 100 cycle (left image) and a 4N test area (right). Scale bars: 50µm.

The effects of adding the suspended graphite particles was evident almost immediately by the formation of much larger flake sizes that were visible through a digital microscope. As seen in Figure 36, the formations absorb enough light to be visible, despite being only a few nanometers thick. Also, in the 2N case, commonly 40µm diameter flakes are observed, and even a near 1mm formation was observed resulting from a 4N loading condition.

(a)

(b)

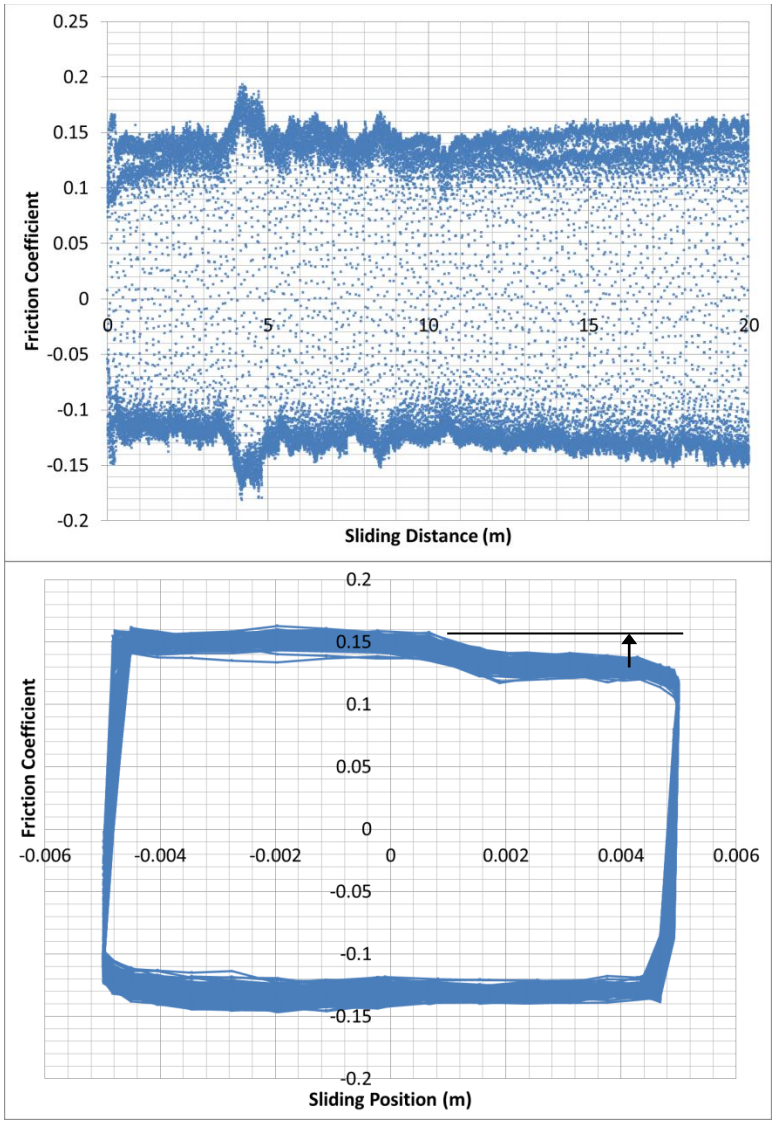

Figure 37. 4N, 2cm/s, 1000cycle wet lubricated in $N_2H_4 \cdot H_2O$ with suspended graphite. (a) Friction map corresponding to sample surface seen in Figure 38. (b) Friction coefficient as a function of sliding position showing step in friction as a result of formed interfacial material.

When examining the testing on the surface of Si, the sliding of the graphite pin in the suspension of graphite in $N_2H_4 \cdot H_2O$ did not exhibit the characteristic friction decomposition as seen in the neat hydrazine hydrate, but instead had a much higher

coefficient of friction (see Figure 37). Also, it was noticed that the friction was somewhat location specific as indicated in the separation of the friction curve in Figure 37. The heightened friction is explained easily by the wear of the silicon substrate as shown in Figure 38, which indicates that the presence of the suspended graphite particles did in fact increase the local contact stresses resulting in material removal from the substrate. Additionally, as also indicated in the figure, a material film was present in the right side of the track whereas the left side appeared to be purely worn Si. This may explain the step in the friction seen in Figure 37 for the right side of the track, such that the presence of the film slightly reduced the friction in that area of the sliding path.

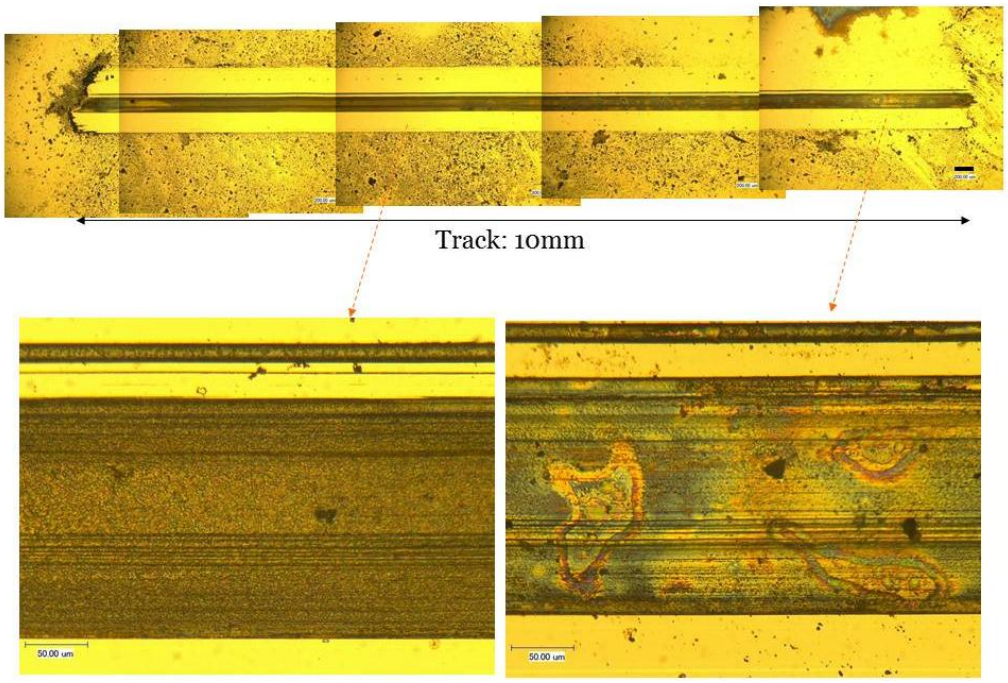

Figure 38. Test area for sliding at 4N, 2cm/s and 1000cyc with graphite suspended in N_2H_4. Notice large wear track (magnified in bottom left callout) in center of sliding path not seen in previous tests. In bottom right callout, there is some interfacial material formation inside wear track. Scale bars in top images: 200μm; in bottom: 50μm.

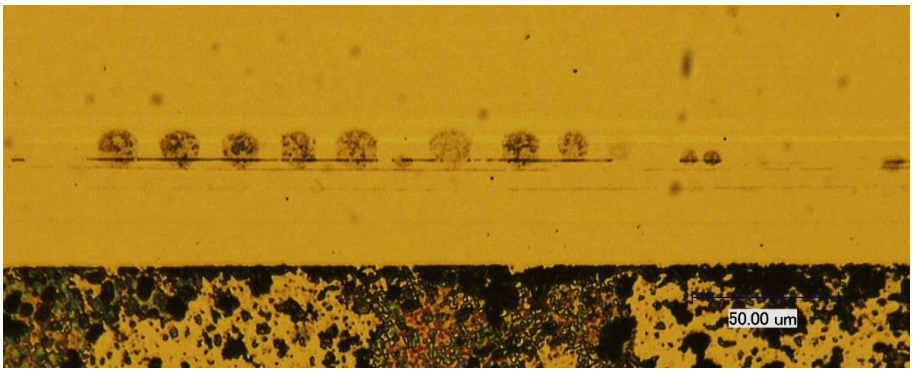

Figure 39. Large flakes observed inside sliding path near beginning formation of wear scar.

Despite the wear of the silicon substrate, when looking more closely at portions of the test area that were unworn, the appearance of large flakes similar to those seen in the Si_3N_4 sample (Figure 36) were observed as shown in Figure 39. These large and visible particles were located on top of a small surface scar resulting from abrasion of the Si, indicating their formation is directly related to the contact stresses from the tribosynthesis process. Note: the dark area at bottom of image is the edge of the sliding path (test area) where debris is collected. Furthermore, a "smooth" portion of the test area was scanned using the AFM to determine the presence of non-visible particles and determine surface characteristics. As seen in Figure 40, the surface of the test area was covered with flake nanoplatelets of varying size, although similar height. Other instances of formations in the area are included as supplemental data in Appendix A. Also from the image, it is notable that the sizes of the particles are highly organized in the direction of sliding. Additionally, the periodicity of the formations is very regular,

suggesting that the synthesis of the particles is not at all random, but highly correlated to the conditions at the surface. This will be discussed further in the next section.

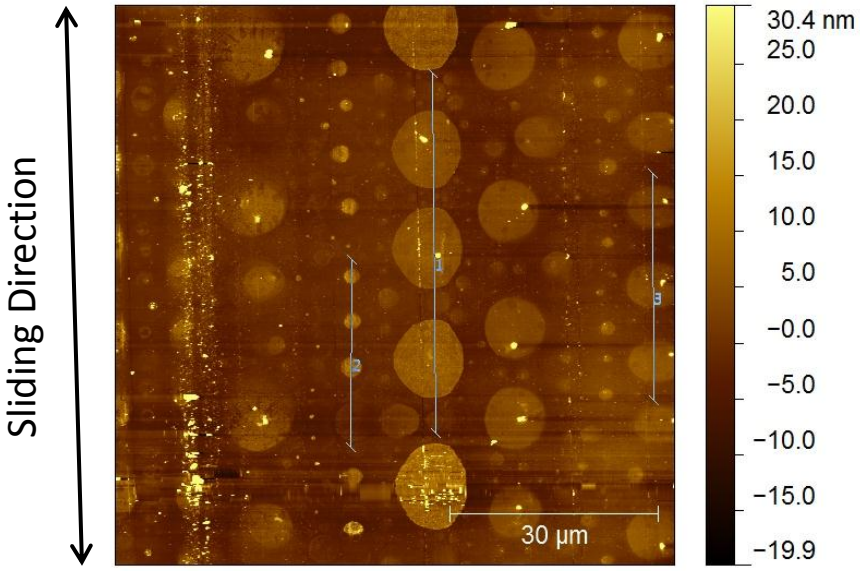

Figure 40. AFM height image showing formation of regularly ordered nanostructures inside sliding path during wet-sliding with suspended graphite (4N, 2cm/s, 1000cycle).

When looking specifically at the height profiles highlighted in Figure 40, again we find that the heights of the flakes tend to follow a set pattern of a characteristic height in multiples. The smallest particles of thinnest vertical dimension showed thicknesses of just under 2 nm, while the larger particles showed thicknesses of ~6 nm, and in the largest case, ~12 nm. Here we also see the regularly defined periodicity of the particle formations, and in the particular case of Profile 1, it is observed that the space in between the larger formations have smaller particles centered in between. Unlike the tests performed in plain $N_2H_4 \cdot H_2O$, these formations are obviously less regularly ordered

in size throughout the scan area, but the ordering within the sliding direction is uncanny. Additionally, though at a 4N load over a similar average contact area, the largest particles in Figure 40 and Figure 41 are at least twice the diameter of those seen in the same loading conditions previously charted in Figure 33. This suggests that either (1) the presence of particles in the solution or (2) the longer scanning period (1000 cycles as compared to ~100 in CTE testing) encourages the formation of these larger particles.

Additionally, some larger formations were also observed occasionally inside the sliding area that were visible through optical microscopy. One such flake is depicted in Figure 42 where a 3D rendering of the shapes from an AFM scan shows one side of the 20×100μm flake which appeared as a flat shape with larger debris particles adhered to the surface. The total height of the flake plus debris was around 120 nm, and the debris appeared to add approximately 80-100nm of height to the surface.

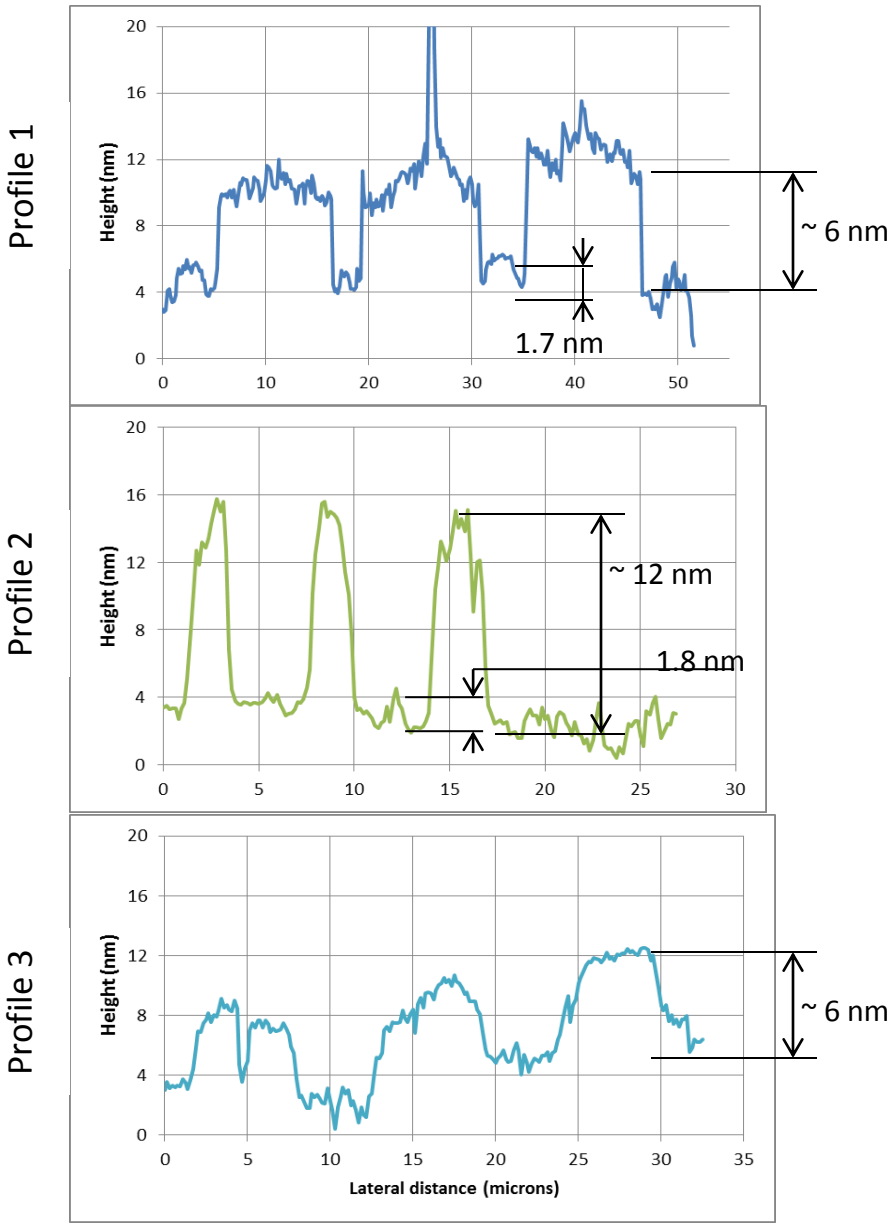

Figure 41. Height profiles for platelets in Figure 40.

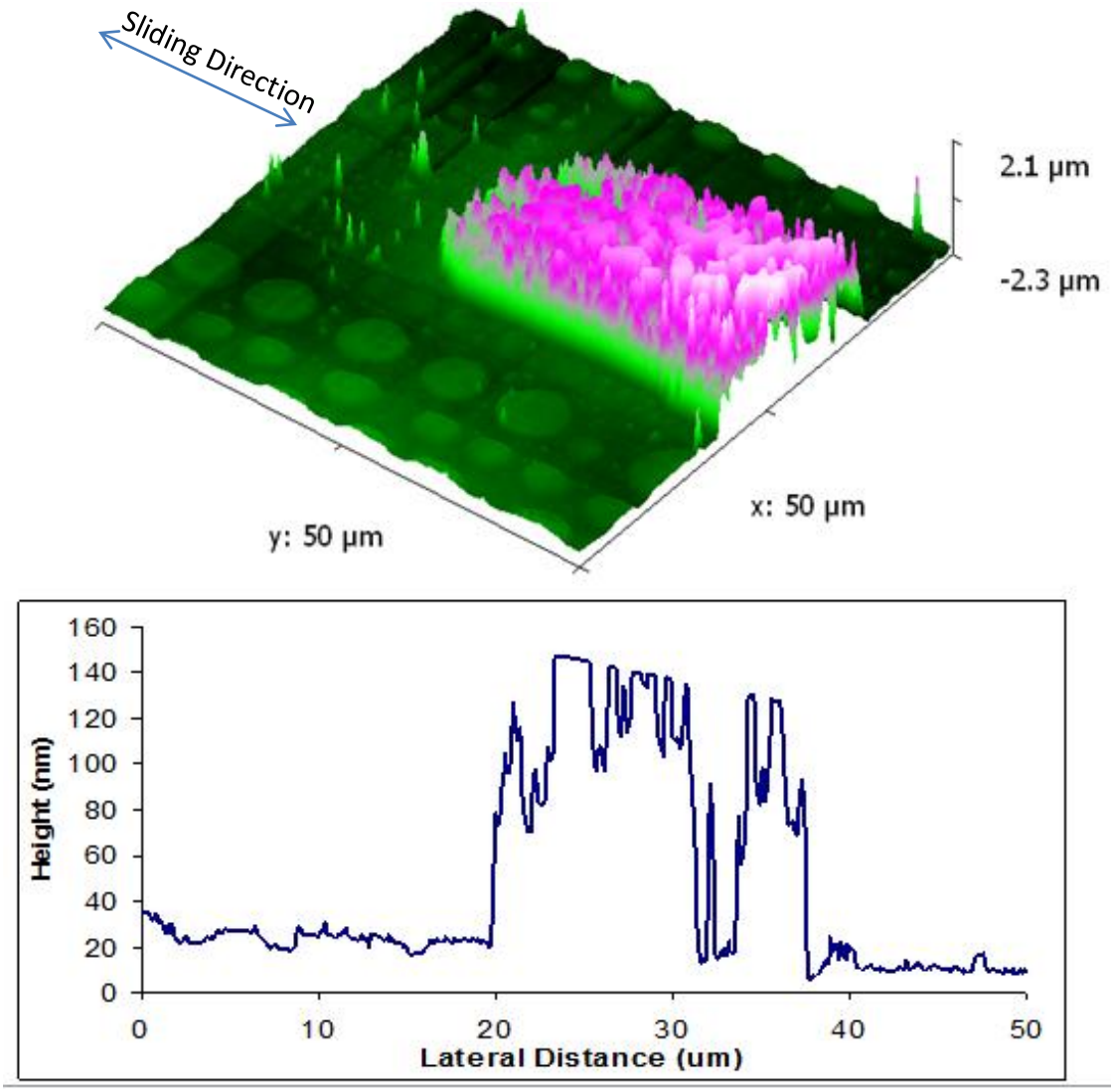

Figure 42. Large flake formation inside sliding path amidst circular shapes discussed previously. The heights of the features were 120 nm for the large object and 5.3 nm for the smaller flakes.

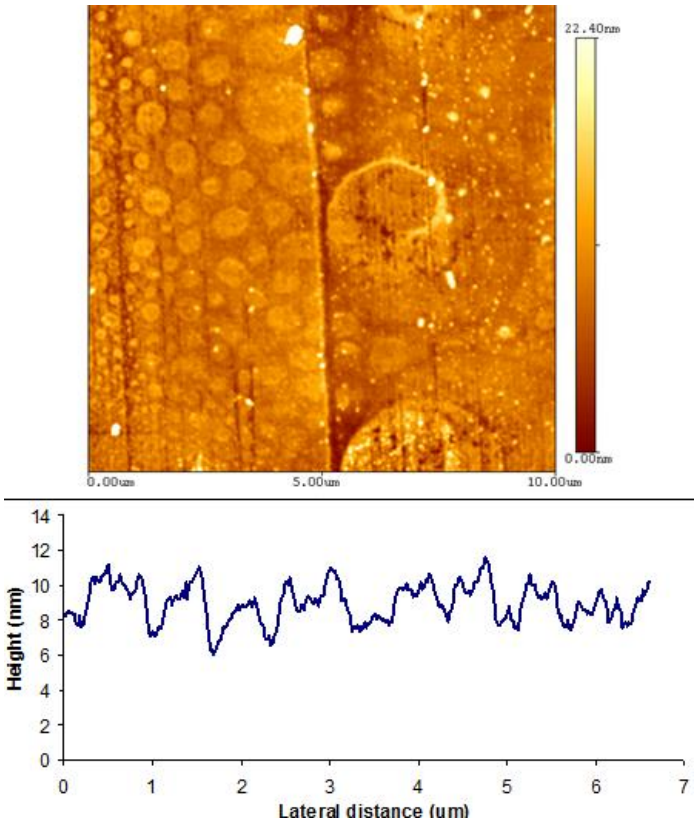

Figure 43. Flake formations seen in trail of larger particle. Height of particles is ~2.5 nm.

Additionally, the same ordered thin features are seen next to the larger flake, which similarly to the earlier measurements, exhibited ~5nm thicknesses. Furthermore, in the sliding direction of the test area, behind the particle, a film of smaller thin flakes are also observed, for which a higher magnification AFM scan is provided in Figure 43. These particles also exhibit the characteristic thickness or ~2.5nm and diameters down to 100 nm, which are smaller than those obtained from the CTE optimization trials. These smaller diameter particles formed under the larger flake suggest that either the load is distributed under the large flake, the reaction is limited by the barrier of the large flake

such that smaller features are favored, or the large flake is composed of the smaller particles which deposit during the sliding process and then continue to grow. The absence of the larger particles in the earlier CTE experiments suggests that the last case is not necessarily true, so it is likely one or a combination of the first two cases. As such, a diffusion limited reaction is expected, which makes sense when considering reaction kinetics.

In addition to the formations observed within the sliding area of the tribosynthesis area, a number of flake-like particles were observed in the area outside sliding path, which were presumably suspended into the liquid medium during the tribosynthesis procedure, and then re-deposited when the surface was dried. These particles, shown in Figure 44, were observed with the digital microscope and then the diameters were measured (indicated by the dimensioning lines in the images) and reported in the histogram in the bottom left of the figure. Here it becomes immediately apparent that these formations are much bigger than those in the test area with average diameters near 40 μm and ranging up to nearly 100 μm. It is believed that these formed at the sliding interface much like the others previously discussed, but that these – having larger sizes – were much more susceptible to viscous effects and fluid shear were carried away by the liquid medium during the tribosynthesis procedure. These large flakes reiterate the influence of the three-body abrasive processing, where the presence of the suspended graphite contributed in some way to the larger particle generation.

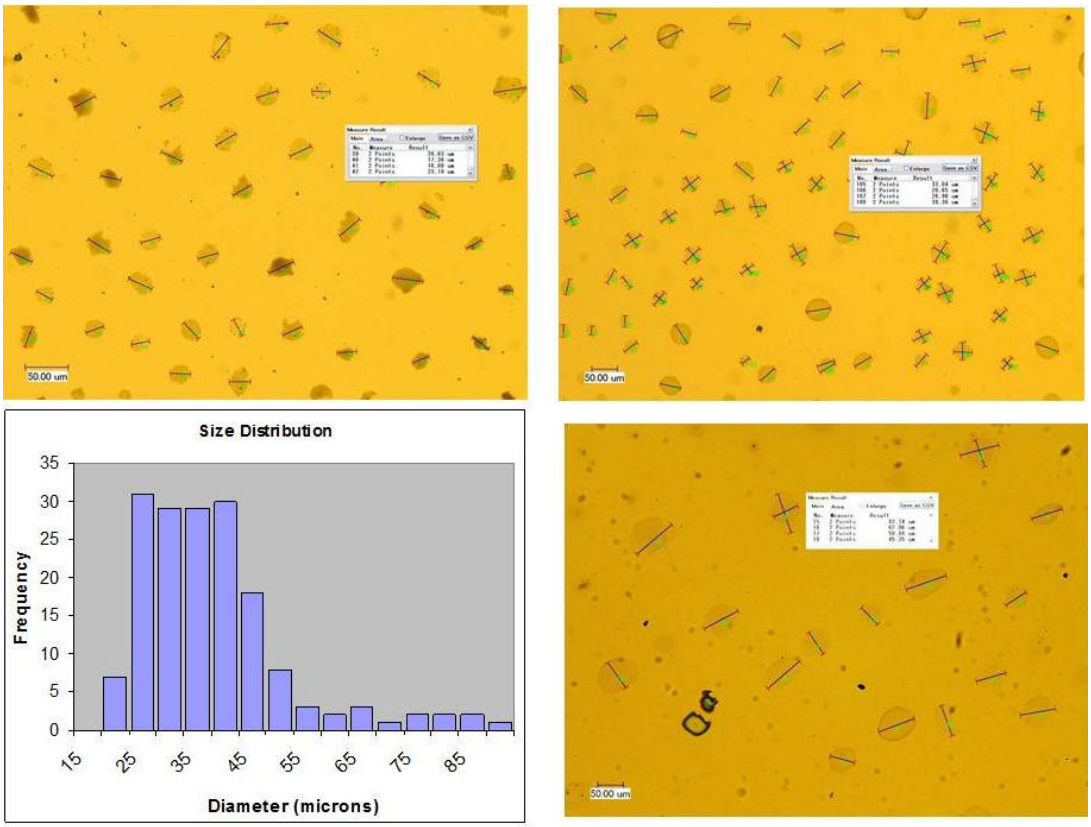

Figure 44. Observation of many flakes deposited outside sliding path, presumably suspended in the test medium (graphite suspended in $N_2H_4 \cdot H_2O$) then deposited as dried. Histogram showing an average diameter near 40µm. Scale bars in images: 50µm.

Using the images' pixel depth in the images, the particles' absorption of light was estimated using a thresholding procedure in the digital microscope images of the large particles. Using ImageJ, the 256 bit RGB images were converted into 8-byte grayscale images; then the background brightness level (or intensity) was measured to determine the baseline reflected light intensity. This value was scaled by the color depth (0-255), and then the reflected light intensity of the particles was determined by increasing the image intensity threshold until the particles were captured. This intensity

was then referenced against the baseline value in order to determine a percentage decrease in brightness. This measurement can be used as an approximation of the absorption of light passing through the particles, so long as the scattering of light from the particles is much less than the transmittance. For these particles in which a uniformly thin and flat surface is observed, this assumption is appropriate. The process yielded staged results in which certain particles exhibited more or less decreased intensity than others, indicating various tiers of absorption, or a stepwise effect. The resulting data is presented in Table 8. The steps can be assumed to be related to the stepped thickness of the particles discussed in the previous discussion, for which each characteristic thickness absorbs a distinct percentage of the light. This raises a peculiarly similar characteristic of the tribosynthesized material to graphene layers, which have been shown to absorb exactly 2.3% of incident white light per atomic layer as a result of graphene's electronic structure.[8] Especially when considering that the material synthesized by the tribosynthesis procedure is only several nanometers thick, most materials at that thickness are completely transparent. This extraordinary feature suggests that the material is indeed graphene, or at least graphene-based, for which more careful spectroscopic determination and characterization will be discussed in Section 4.2.3.

Table 8. Optical absorption of platelets on Si surface.

Threshold Step	*Intensity Decrement, % (raw brightness value)*		
	Image 1	Image 2	Image 3
Background	(249)	(249)	(215)
1	**3.6** (240)	**3.6** (240)	**5.1** (204)
2	**17.7** (205)	**10.0** (224)	-
3	**26.1** (184)	**26.1** (184)	-
4	**37.8** (155)	**34.9** (162)	-
5	**51.4** (121)	**45.8** (135)	-

Another set of tests were performed using the graphite suspended in $N_2H_4 \cdot H_2O$, except instead of using the suspension as a liquid medium for testing, the solution was deposited on the surface of Si, and allowed to air dry prior to the sliding of the loaded graphite pin. A small amount of the liquid was still present at the beginning of the sliding procedure, which had primarily migrated to one side of the test area. As before, after processing, the surface was examined in the digital microscope and is presented in Figure 45. In this image it is noticed that a large collection of debris/surface modification is observed on the side of the track where the remaining liquid had settled.

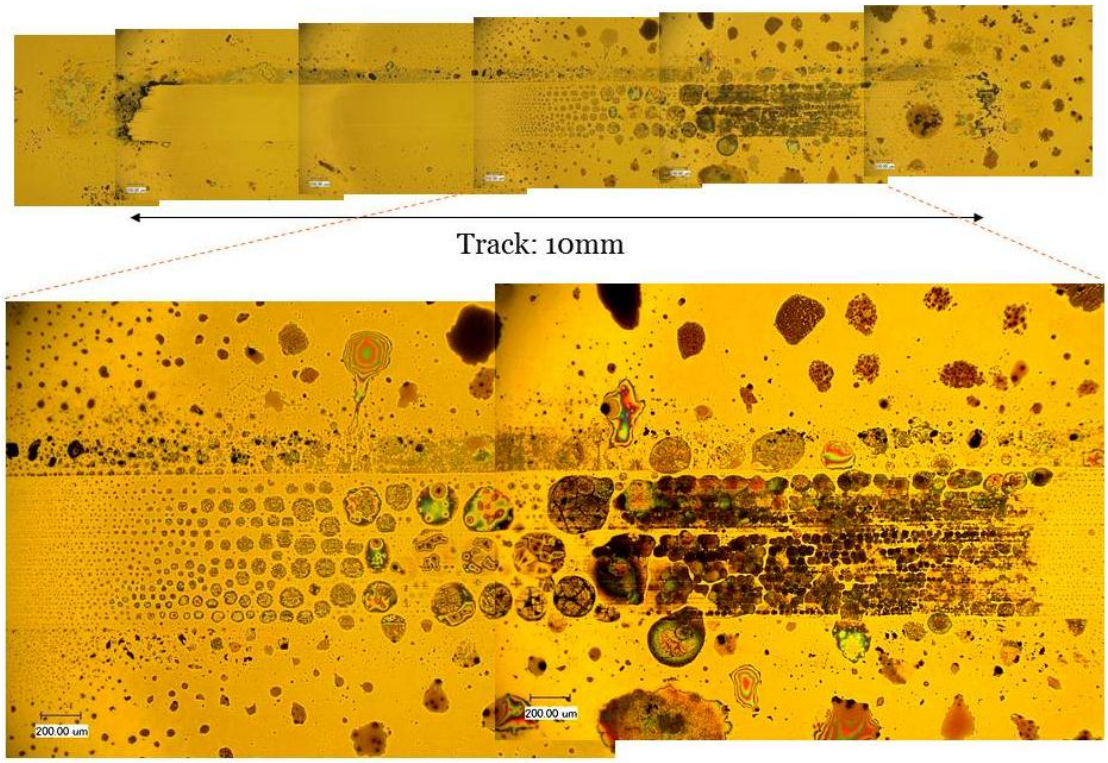

Figure 45. Shaved graphite suspended in Hydrazine hydrate, dried on surface prior to test: 4N, 2cm/s, 1000cycle. Scale bars are 200µm.

A closer examination of this darkly patterned area of the test area (Figure 46) showed similar circular flake like nucleations, but with much more complicated geometries and features on their surface and of much greater size than seen in previous images. Many of the particles in these images have diameters greater than 100 µm! In fact, it is seen that there are several very large, non-circular formations (>250µm) that are comprised of many circular shapes of 50-100µm. Furthermore, as illustrated in the top left image, some of the particles exhibited fractal-like patterns on their surfaces which may be indicative of organic substance on the surface. It is also possible that

some of these lines may be the result of folds in the material that arise from the rubbing procedure, or even a thermodynamic tendency for thin materials to fold.[122]

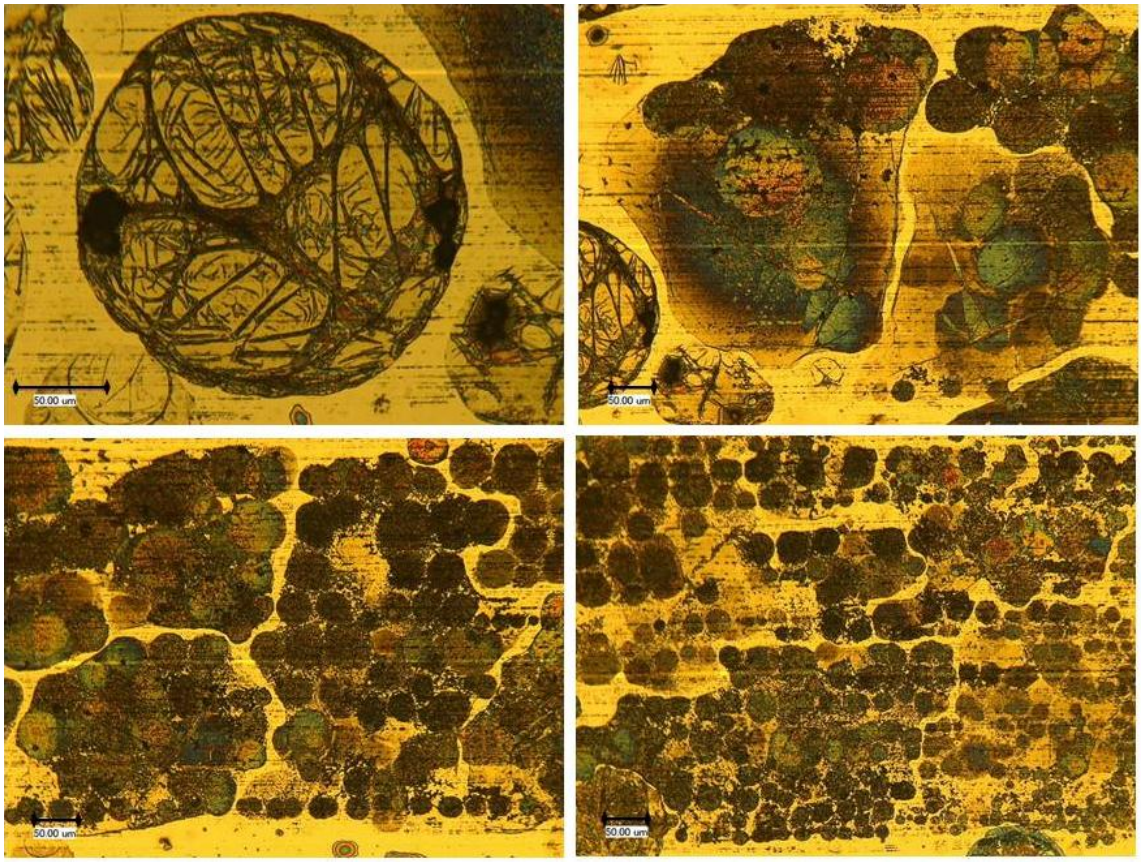

Figure 46. Close-ups of larger particles from previous figure. Notice fractal patterns in top left. Also, notice secondary nucleation events inside largest flakes. Scale bars: 50 um.

From AFM scans of the material, it was determined that the visible materials were much thicker in parts than those seen in the previous tests, although isolated particles on the surface were found with <1 nm thicknesses (see Figure 47) along with many others that also exhibited the characteristic dimension seen in previous samples (Figure 48 and Figure 49). The intriguing aspect about these formations is that they

clearly exhibit lamellar behavior much like graphitic materials, where double and triple layers are observed. In Figure 47, the intriguing element is that the platelets exhibit sub-nanometer thicknesses down to 4 Å which is almost the exact inter-layer spacing of graphene (3.34 Å)[123] as determined by XRD of graphite (see Figure 23).

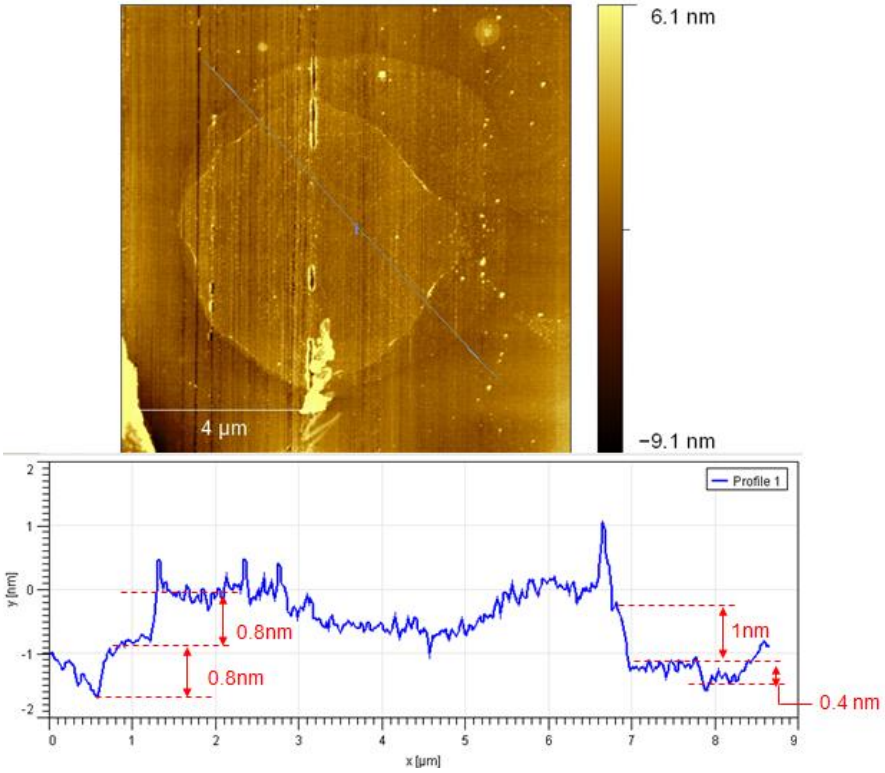

Figure 47. Flakes identified on the surface having thicknesses down to 4 angstroms - equal to that of graphene.

In Figure 48 we also see the lamellar behavior and observe the typical 2-3 nm thicknesses, particularly in the rightmost long particle whose edge is clearly layered, and it also has divots or pits arising from multiple layers of material. Furthermore, the particles are often observed to have larger particles sitting at the center of the platelet

formations as seen in both Figure 48 and Figure 49. This is presumably related to their formation, since these are likely abrasive particles that were on the surface that provide the stress necessary to induce a nano-nucleation during sliding. Additionally, it is observed that the edges tend to exhibit slightly taller features than the inside of the flakes, which can be attributed to curling or "scrolling" of the edges of the flakes to reduce the surface energy at the edges. Moreover, this effect is more notable in the direction of sliding of the graphite pin, suggesting that the scrolling is also induced from the friction and sliding.

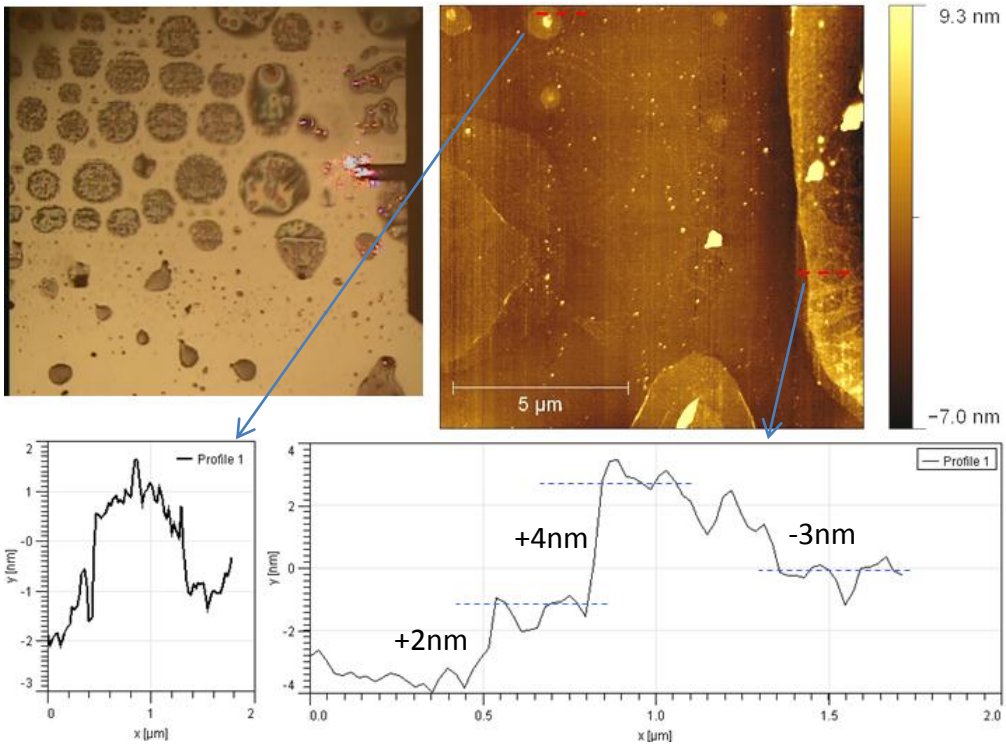

Figure 48. Lamellar flakes identified directly, having 2-3 nm step heights between layers.

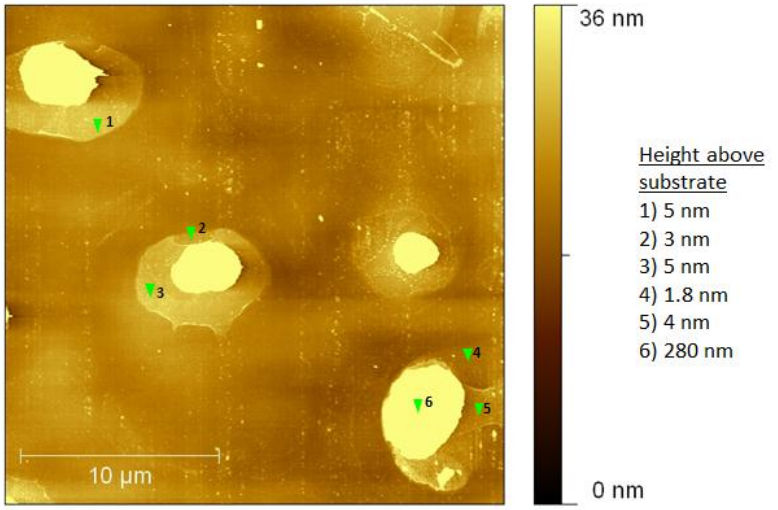

Figure 49. Additional flake formation and step heights for various locations. The larger particles are seen on top of the formations suggesting that they play a role in the synthesis of the nanoplatelets.

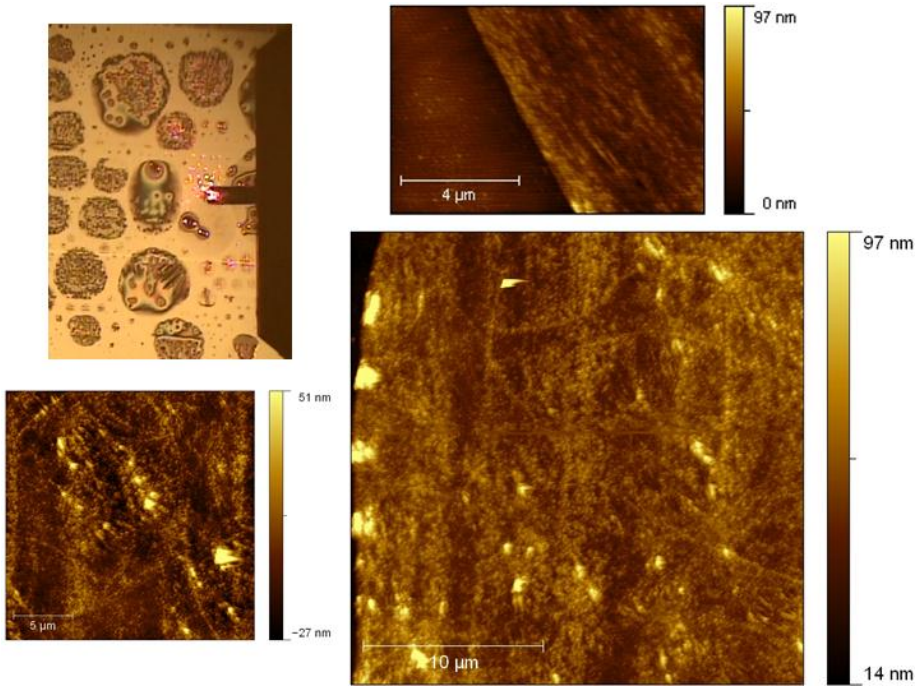

Figure 50. Large, thin flake found on surface having 30 nm thickness while maintaining a smooth surface though nearly 100 µm in diameter. Top left: scan location on thin feature. Top right (and bottom right): edge of flake having a 30 nm step height. Bottom left: surface of particle showing very little variation.

Regarding the much larger platelets of extremely large dimensions compared to the graphitic-like formations just discussed, their thickness is expectedly greater, as they are readily seen by optical microscopy. While many of the large particles had large fractal patterns on the surface, still several existed which appeared very smooth and of slightly darker brightness amongst the other formations such as the one shown in Figure 50. Here a ~100μm diameter particle was seen to have only 30 nm thickness, and relatively smooth surface across its face. In contrast to this particle, the darker particles' fractal-like patterns on the surface were found to be 50-200 nm taller than the surrounding surface for the smaller features, and 1-3μm for the largest features. Aside from these features, the particles also were smooth along the surface, and exhibited similar image contrast in the smooth regions to the smooth particle discussed in Figure 50. Additionally, AFM analysis of the features did not show any evidence of being a separate material from the base flake (see Figure 51) such as debris. Furthermore, the rippled appearance of the edge of the flake seen in Figure 52 also points to the particle being folded rather than having a separate material growing on the surface. Also note that immediately next to the large formation several characteristic flakes like those seen in other trials and samples are seen having 2.5 nm and 5 nm thicknesses. This proximity may show that the presence of the larger particles (this one having an edge height of ~1.8μm) doesn't prevent the formation of nearby particles. It is suggested that these large formations with fractal-like features on their surface are actually similar to the particle in Figure 50, but having experienced internal folding and scrolling due to the rubbing process.

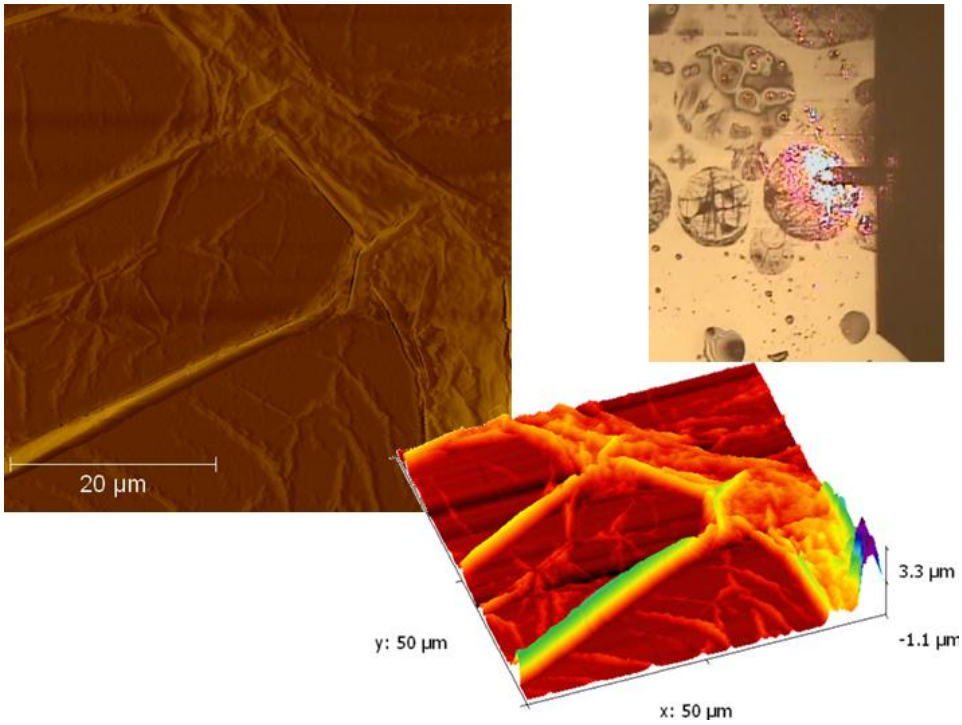

Figure 51. Fractal-like patterned shape. Left: shaded height image, Right: scan location, Bottom: 3D height representation of pattern.

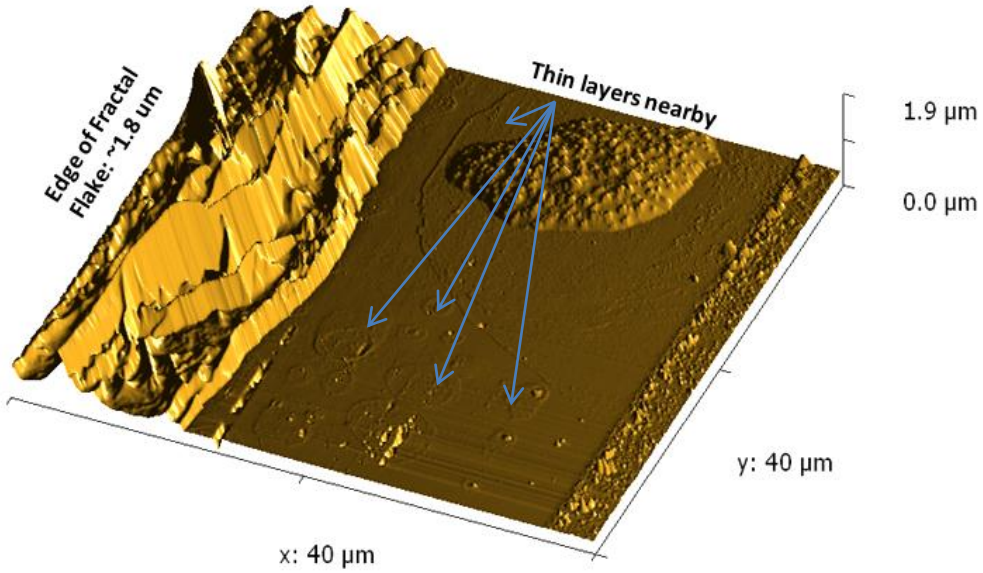

Figure 52. Edge of fractal-like shape with apparent folding. Nearby on the surface also is characteristic 2.5 and 5 nm thick flakes.

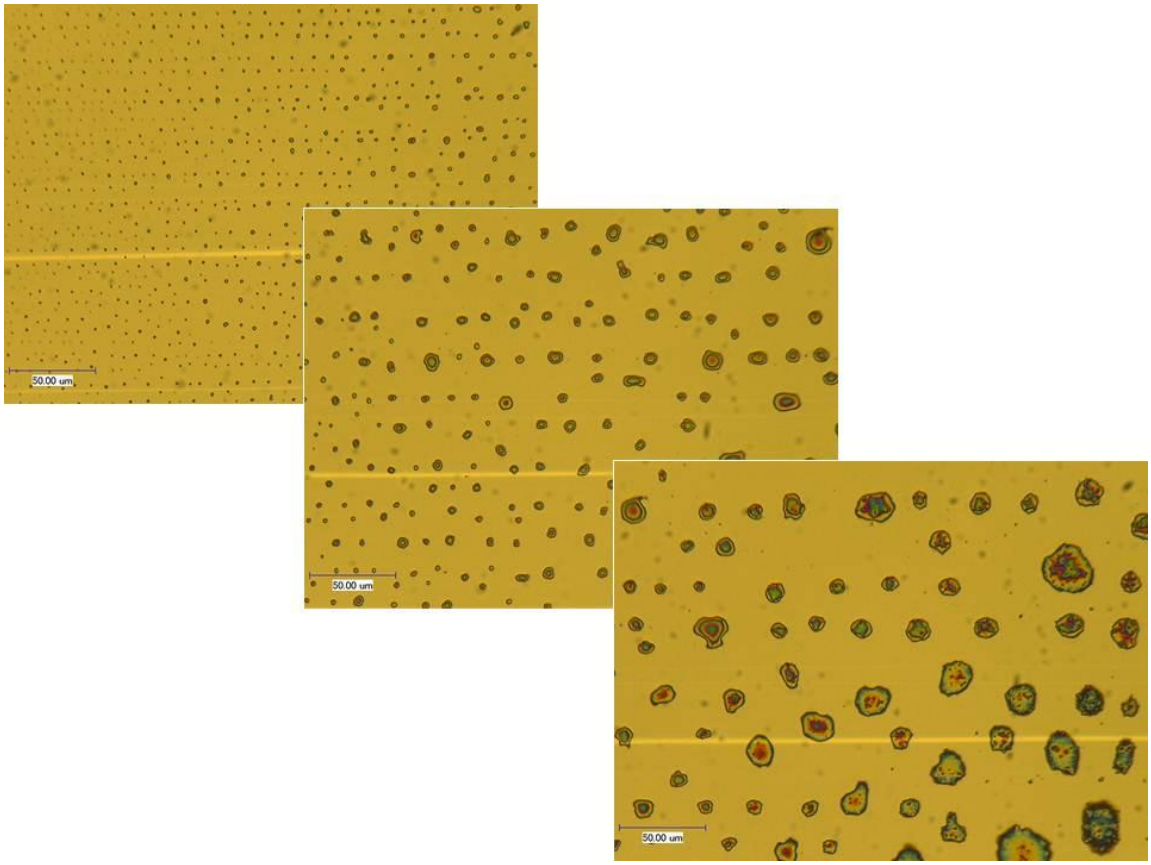

Figure 53. Transition from small flakes to larger. 800x images; scale bar: 50 μm

On the other side of the test area (away from where the liquid settled), a different behavior was observed as presented in Figure 53. Here, a transition between small nucleation events and the larger ones seen in Figure 46 is observed as the pin nears the area of where the remaining liquid had settled. That observation, combined with the knowledge that the friction over the surface was relatively uniform (see Figure 54), leads to the conclusion that the formation of the material is not only dependent on the loading and sliding conditions, but also the presence and concentration of both the hydrazine and graphitic material – reiterating the presumption of a diffusion-limited process (discussed

on page 81-78). Some interfacial reaction still occurs where the presence of the "free" graphite and $N_2H_4 \cdot H_2O$ is limited, but the reaction proceeds at a much faster rate – leading to larger particles over the same time period – where the material is present in greater amounts on the surface. Furthermore, the absence of a liquid medium during the sliding process prevents the suspension of sufficiently large particles as seen in the "wet" testing, so that the large particles remain at the tribosynthesis test area and continue to grow and thicken during the cyclic loading.

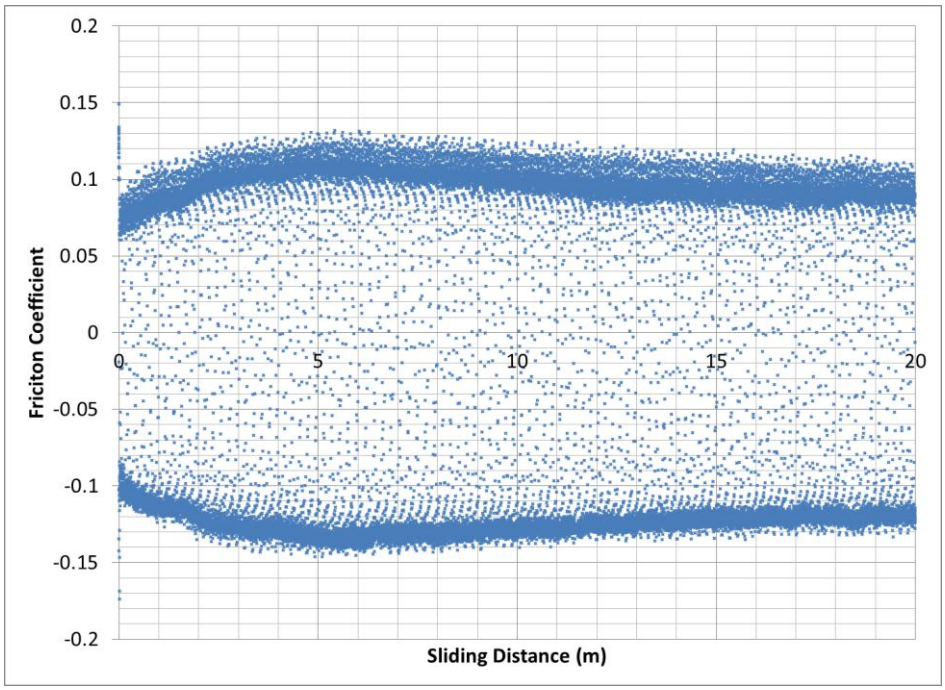

Figure 54. Dried graphite-hydrazine solution on surface of Si, friction versus sliding distance: 4N, 2cm/s, 1000cycles.

Additionally, to verify that the production of these nanoplatelets are in fact a result of the tribosynthesis process, the graphite suspension in hydrazine hydrate was deposited onto a Si substrate and then investigated for the presence of nanomaterials. No flake-like formations were observed by AFM, however, after exposing the solution to UV light for 8 hours (see process for sample: CMG1), a TEM examination of the fluid residue found coagulated nanoplatelets randomly oriented and of non-ordered shapes, as seen in Figure 55. These shapes exhibit crystallographic edges, and a corner having an angle of 150° is clearly defined, which is exactly the angle between the graphitic armchair and zigzag edge orientations (see inset schematic), which are defined as such due to the shape resulting from the shape of the hexagonal lattice at the edge of that direction.[113] This same 150° angle was observed upon close examination of some of the flakes formed from the dry sliding procedure (see Figure 56). This indicates the nanoplatelets also have the graphitic lattice structure; or at least have it as a backbone to the structure that formed as a result of the tribosynthesis procedure.

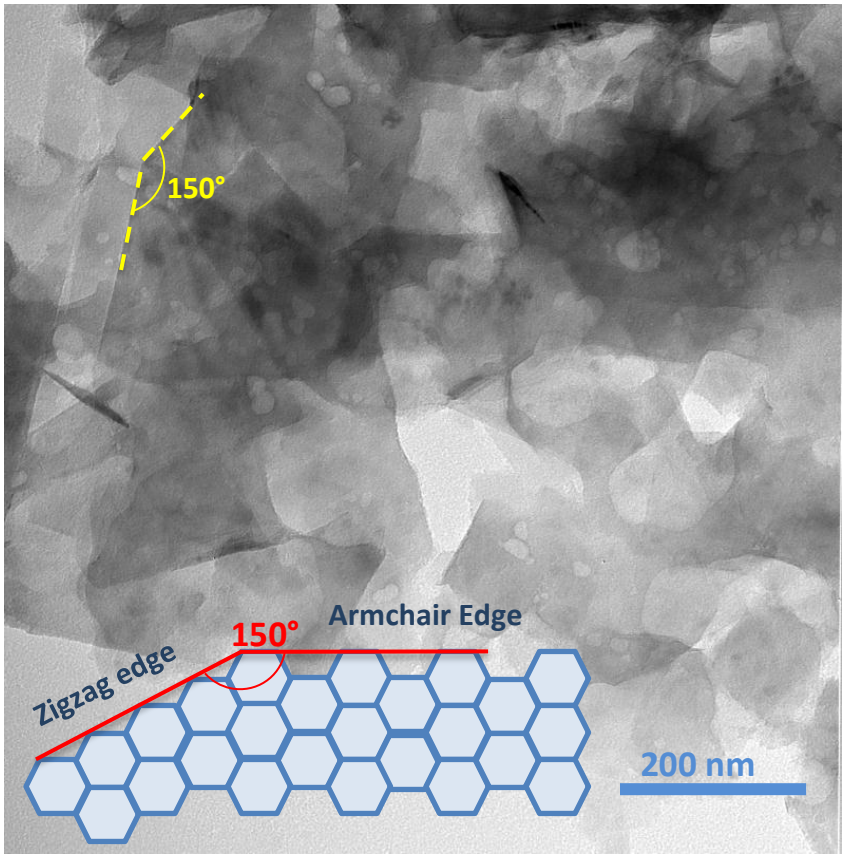

Figure 55. Apparent graphene flakes formed through UV irradiation of the shaved graphite in hydrazine hydrate

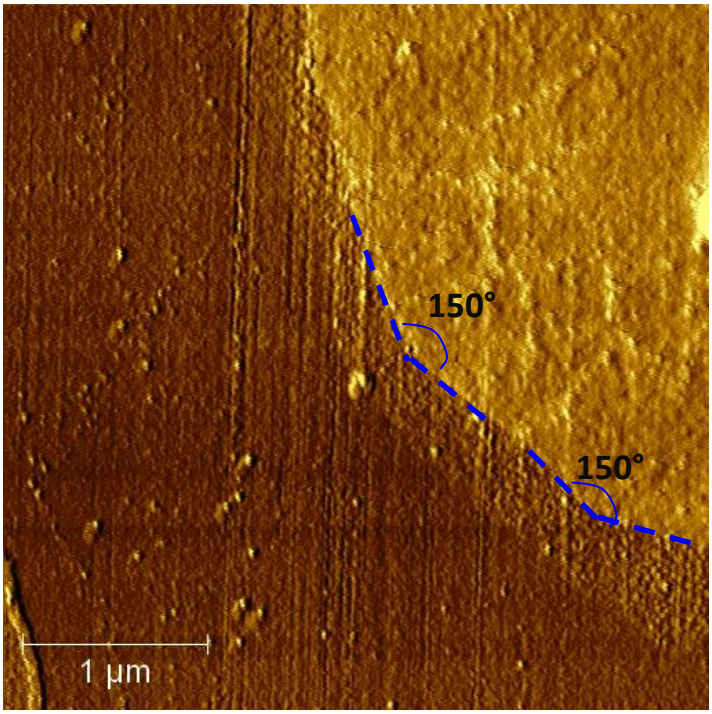

Figure 56. Characteristinc 150° angle between armchair and zigzag lattice directions observed in tribosynthesis tests as well.

Additionally, these apparent graphenes in the CMG synthesis have sizes on the order of 100nm, which are at least twice the size of the crystallites observed in the control experiments and calculated according to the Sato correlation.[117] In addition to these UV exposed samples, a number of other chemical approaches to obtaining chemically modified graphenes or CMGs were evaluated and found to produce graphene related platelets. A summary of the results of these experiments can be found in Appendix B. Moreover, these results suggest that despite originally consisting of 35-40 nm crystallites, when the graphite from the rod is exposed to an external energy source such as UV irradiation or strain/friction mechanical power in the presence of the reducing agent N_2H_4, the flakes have the propensity to grow in lateral size.

With the combined results of the sliding and the UV exposure, it appeared that the tribosynthesis process had resulted in the formation of larger graphene or graphene-based platelets whose size and shape were dependent on the processing conditions. However, visual data does not prove the existence of the graphene material, so additional spectroscopic evaluations were made to elucidate the chemical nature of the produced nanomaterials. This is discussed in the next section.

4.2.3. Spectroscopic Characterization of Tribosynthesized Nanomaterial

The production of these nanomaterials must be accompanied by reliable spectroscopic data that validates whether in fact these are indeed graphenes or CMGs. A number of various spectroscopic investigations were made from the samples produced, including UV-vis absorption, FTIR, XPS, and Raman; but often the problem of poor signal quality due to the small concentration of material deposited on the surface and the tiny nature of the materials themselves prevented the direct measurement of the nanomaterial properties. Even so, the procedure to produce the nanomaterials was adapted to increase the concentration as much as possible by increasing cycling and operating in the ideal test ranges identified by the process optimization as described previously in Figure 34.

As a starting point, some control tests were performed to observe the spectroscopic nature of the graphite powder alone as compared to the tribosynthesis procedure results. As a baseline, shaved graphite was dispersed in DI water and $N_2H_4 \cdot H_2O$, and the CMG1 sample (exposed to UV irradiation) were tested for their UV-vis absorption spectra. The 1 wt% graphite in H_2O exhibited no distinct absorption

wavelength, but the samples in hydrazine hydrate had strong absorption in the region <240 nm, presumably as a result of hydrazine interaction with the graphite. In order to obtain a measurable signal for the graphite in the hydrazine solutions ("Gr in Hyd"), the suspension was diluted many times with DI water until the concentration of graphite was 0.02 wt%. The effect was to reduce the saturated signal which was determined to be a result of the hydrazine hydrate, which always exhibited strong absorption below ~220 nm with exponentially decaying intensity up to ~300nm, which was also represented in literature.[124] The resulting absorption spectra (Figure 57) revealed absorption at 268, 254, 250 nm and also exhibited a saturated signal at 230nm in the case of the UV irradiated sample, but the non-irradiated showed no distinct peaks above 220nm.

According to several literature sources, the peaks observed in the UV irradiated sample (CMG1) correspond to graphene related electronic structures. In fact, the theoretically calculated wavelength for energy absorption of a hexagonal carbon ring due to its electronic structure was calculated by P.R. Wallace in 1946 as 230 nm.[9] More recently, absorption of GO peak was shown to be 230nm[110,120,125] and the graphene peak isolated at 280 nm.[125,126] The differences in these values from Wallace's calculations probably arise from new understanding of graphene electronic structures which were not well understood before the past 5-10 years. Furthermore, Li et al., demonstrated that the amount of oxygenation (OH and COOH functionalization) of the GO creates a spectrum of peaks between 231 and 270 nm, indicating the relative purity of the graphene isolated in the sample as it undergoes reduction via hydrazine.[126] The peaks observed in the CMG1 test case suggest that the UV synthesis process produced a relatively small

proportion of reduced graphene flakes (270nm peak) while having a larger proportion of GO (230nm) and partly reduced GO (in between peaks) that are likely partially N_2H_2 and N_2H_3 functionalized according to Kim et al.[106] This validates the claim of graphene materials being produced from UV excitation in $N_2H_4{\cdot}H_2O$, and furthermore, suggests that the energetic formation possible via tribosynthesis is also feasible as an alternate reaction pathway, as alluded to on page 96-91.

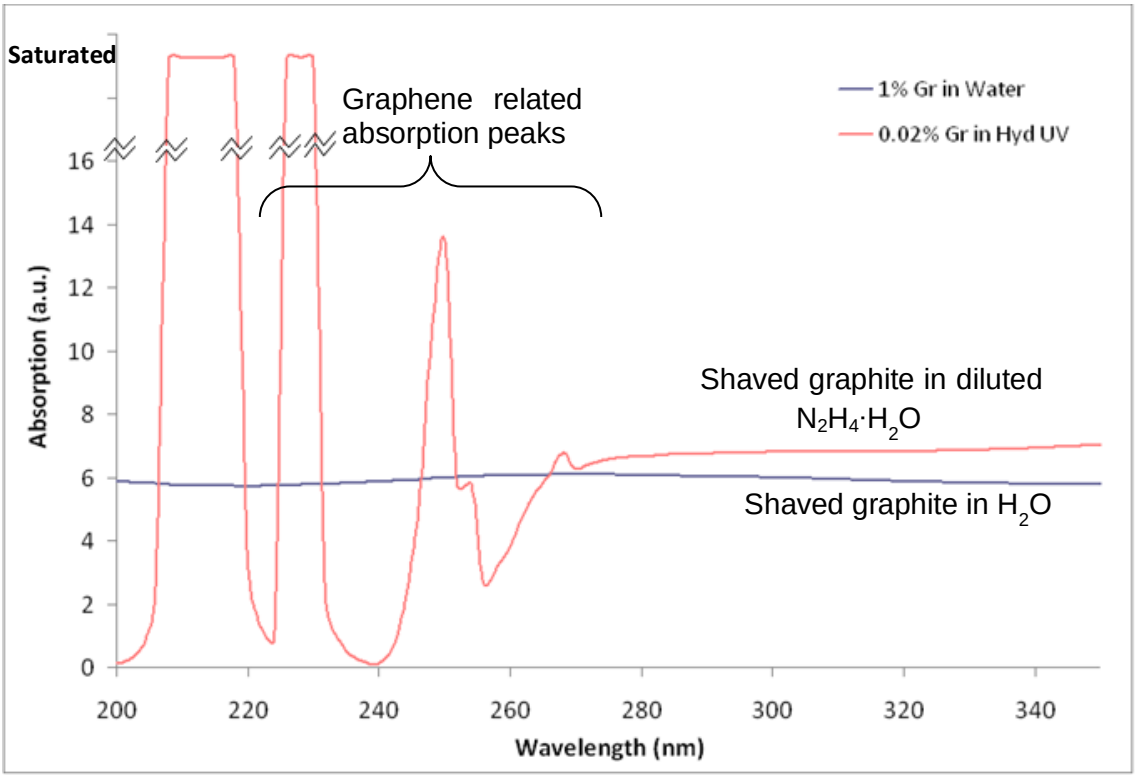

Figure 57. Absorption spectra results of shaved graphite in water and hydrazine hydrate showing the formation of graphene based materials.

Unfortunately, the small concentrations afforded by the tribosynthesis procedures would not yield a measurable quantity of material for gathering absorption spectra, so

alternate methods were invoked to produce measurable quantities of material. Instead of depositing 50 μL of $N_2H_4 \cdot H_2O$ on the substrate as a liquid medium during a single test event, in one case 100 μL was deposited on the substrate and cycled 8,500 times, after which the liquid was collected. Also, the noticeable amount of material synthesized (observed by the color change of the liquid from clear to orange/brown; see Figure 58) allowed for additional capture of particles by depositing a ~200 μL droplet of DI water onto the substrate, allowing to soak for ~15 minutes, collecting it, and repeating until a sufficient quantity of liquid for UV-vis testing was obtained (2.5-3mL). An alternate method consisting of performing 10 repeated 500 cycle tests in a fresh 50 μL $N_2H_4 \cdot H_2O$ medium at 0.5 mm spacings on Si was also attempted. Each of the tests was performed with a 4N load to both encourage larger formations and encourage their re-suspension in the fluid as a result of surface scrubbing.

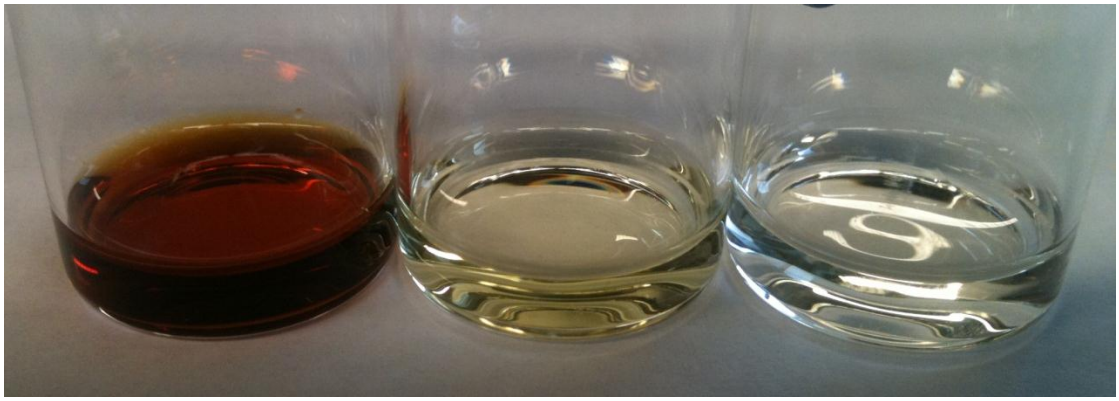

Figure 58. Suspensions of tribosynthesized material from 8,500 cycles on Si_3N_4 (left), 8,500 cycles on Si (center) and 5,000 intermittent cycles on Si (right).

As seen in Figure 58, the color change of the liquid media from clear to an orange/brown solution matches the results of colloidal GO synthesis observed by Stankovich et al.[127] Additionally, the darker result seen on the Si_3N_4 surface suggests that some interaction with the surface also affects the rate of formation, or the nature of the electronic structure resulting in absorption. When looking at the absorption spectra of the two high cycle tests (presented in Figure 59) the findings were intriguing. While the darker liquid obtained from the cycling on Si_3N_4 exhibited a mass of noisy peaks for all wavelengths less than ~480nm, the lighter yellow solution obtained from cycling on Si showed two distinct peaks of fairly broad range centered about 270 nm and 390 nm. As discussed previously, the 270 nm correlates exactly to the graphene absorption band. The broader and larger peak at 390 nm is attributed to N_2H_2 and N-conjugated compounds.[128] The presence of redshifted N_2H_2 directly confirms the chemical reaction progressions predicted by Kim et al.[106] and Gao et al.[107] during the reduction of graphene oxide. Furthermore, as the wavelength decreases past the graphene band on the Si sample, the absorption rapidly rises to a peak at 230 nm (GO peak) after which it oscillates. This oscillation can be linked to the presence of ammonia (NH_3) in the solution which is a product of the tribosynthesis procedure as the hydrazine decomposes during rubbing. Additionally, the presence of ammonia was detected by the generation of its unique odor during processing. For reference, the oscillatory absorption signal from ammonia is charted in the graph as measured by Chen et al.[129] Furthermore, in previous tribological investigations of sliding on Si_3N_4, Kajdas[130] demonstrated that a

frictional load in the presence of water on Si_3N_4 generates ammonia according to the reaction:[131]

$$Si_3N_4 + 6H_2O \rightarrow 3SiO_2 + 4NH_3.$$

This may also explain the noisy absorption spectra which arose from the formation of ammonia and ammonia-like reaction products due to excess nitrogen atoms available in the solution containing N_2H_4, H_2O and carbons. Presumably, the formation of the flakes is relatively unaffected by this excess nitrogen, as noted by similar production of flakes from the microscopy data; however, the input energy in the form of friction that helps to drive the reaction of the graphenes and their reduction from GO now also encourages additional reactions with nitrogen. Thus, the absorption is not obviously pointing to a specific compound.

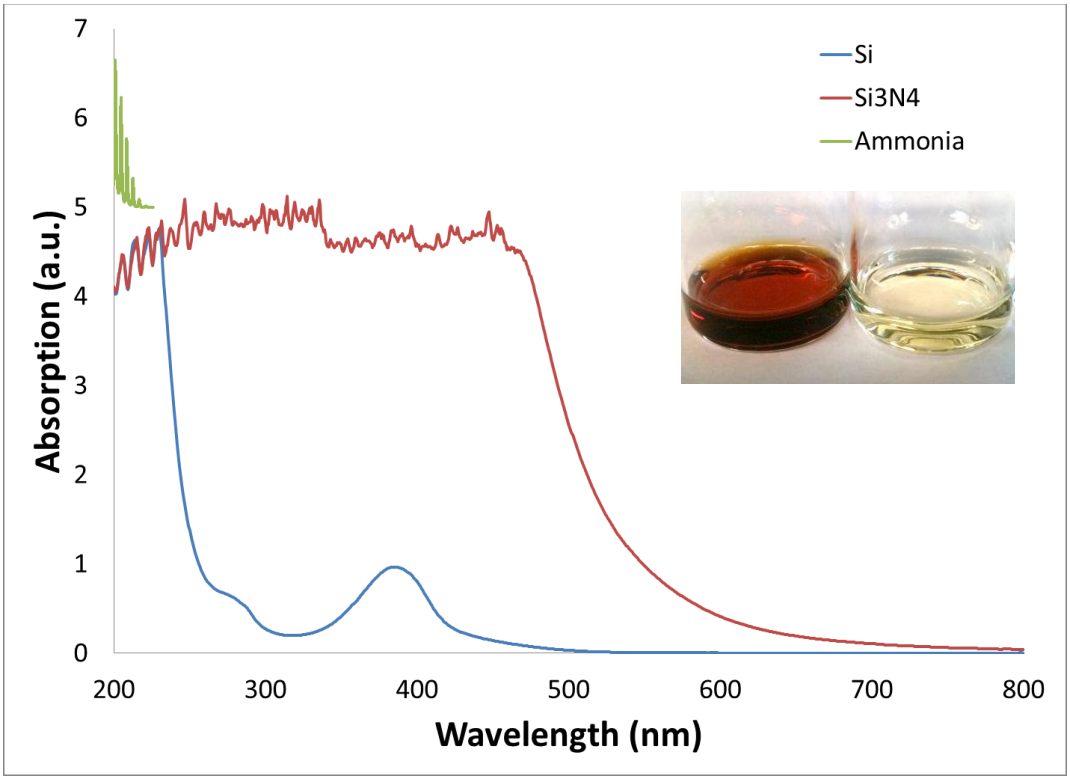

Figure 59. Absorption spectra for 4N cycling 85000 times.
Comparison with ammonia from reference [129]

In order to gain a better understanding of the precise functional groups present on the surface of the flakes produced from this tribosynthesis, FTIR spectra was taken for the samples. In order to obtain useful data, the water from the samples had to be removed; otherwise the signal was not strong enough. The dried powder (brown in color) was then tested for which the results are shown in Figure 60. Although still relatively weak, this fact complemented graphitic FTIR tests found in literature, which were also weak – especially considering that most had completely opaque solutions. The results of these literature reports were cross-referenced against the peaks seen in Figure 60. Several papers reported FTIR peaks resulting from the "graphitic skeleton"

of graphene in the 1500-1600 cm^{-1} range,[121,132,133] with one specific mention of a peak at 1562 cm^{-1}.[133] These peaks are sometimes reflected in results of GO as well as determined by Paredes et al. [120] Additionally, Wang et al. found that GO exhibited peaks in 3000-3700 cm^{-1} as well as around 1600-1700 cm^{-1}.[110] According to Murugan et al. when investigating the use of graphene and GO in nanocomposites, graphene and GO share a peak around 2400 cm^{-1}.[133] Furthermore, when investigating the improved electrical properties of NH_2 functionalized graphene over GO, Lai et al. found a unique peak around 1580 cm^{-1}, although they still expected to have oxygenous groups on the surface.[134] Furthermore, tribo-processing of the nanomaterial on Si and Si_3N_4 raised the important question of whether silicon was involved in the reaction, however, our FTIR revealed that no silanized (Si-O-C bonding) reactions were present according to work done by Hou et al. on silane functionalized graphitic compounds;[135] although SiC was identified at 671 cm^{-1}.[136,137] Using this information from recent literature combined with classically defined functional groups from textbook references,[138] the results yielded that the tribosynthesis technique does in fact yield graphenes, but in conjunction with GO, with surface functionalizations of Si-H groups[137,139] N-H groups and some oxygenous and OH groups as indicated in Figure 60. This correlates well to the characteristic dimension of 2-2.5 nm seen throughout the AFM scans, for which the surface functional group would easily increase the layer thickness from graphene at 0.34 nm and GO at 0.8-1.2 nm (0.86 nm by XRD[133] and application of Bragg's Law). Furthermore, similar results were seen from C-N functionalization of GO previously using chemical approach

for the formation of surface amides [(R-C=O) linked to a nitrogen atom (N) R-(CO)-NR] or carbamate esters (urethanes) [NH-(C=O)-O-].[127]

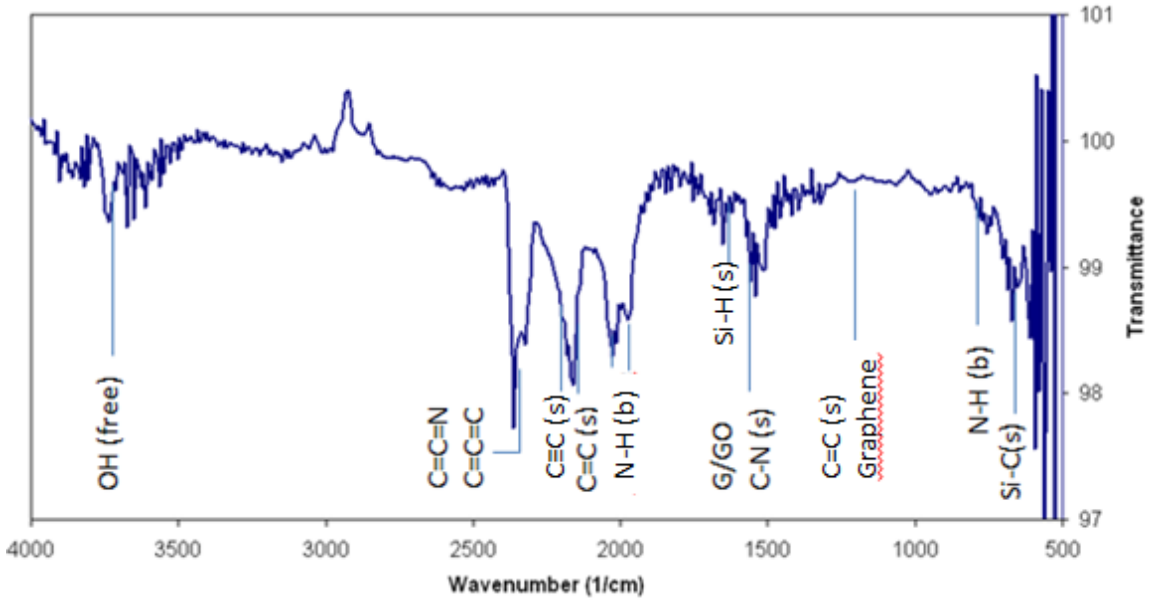

Figure 60. FTIR of particles produced via 10k cycling on Si_3N_4. "s" and "b" refer to stretching and bending, respectively.

As an alternate verification of the composition of the synthesized nanomaterial, XPS was used to identify the electron binding energies (BE) associated with the C 1s electrons, by which their exact BE correlates directly to the type of bonding present. To make sure that the products were not affected by further processing required to obtain sufficient signal strength in the UV-vis and FTIR spectra, the sample was created by rubbing the graphite rod directly on either Si or Si_3N_4 substrates for 6 sets of 250 cycles at 3N and 2cm/s max sliding speed (similar conditions to the CTE testing discussed previously). Between each set, the 50 µL of hydrazine hydrate used as a medium was

removed, and fresh liquid was reapplied for the next test cycle. The collective fluid after all experiments was then deposited on a Si substrate and then heated in an oven at 150°C to remove all liquid and leave behind the solid residue. This residue was tested in the XPS at Stanford Synchrotron Radiation Light Source for which the results are shown in Figure 61. Here the C 1s peak is observed for both the samples created on Si and Si_3N_4 substrates, for which the Si is slightly offset to a higher intensity value arbitrarily for the sake of clarity. In the image, the data can be seen to be quite similar, both having slight shoulders on the high energy side (left), which can be attributed to the presence of C-N and C-O bonds on the surface. These peak locations are represented by the vertical lines in the chart.

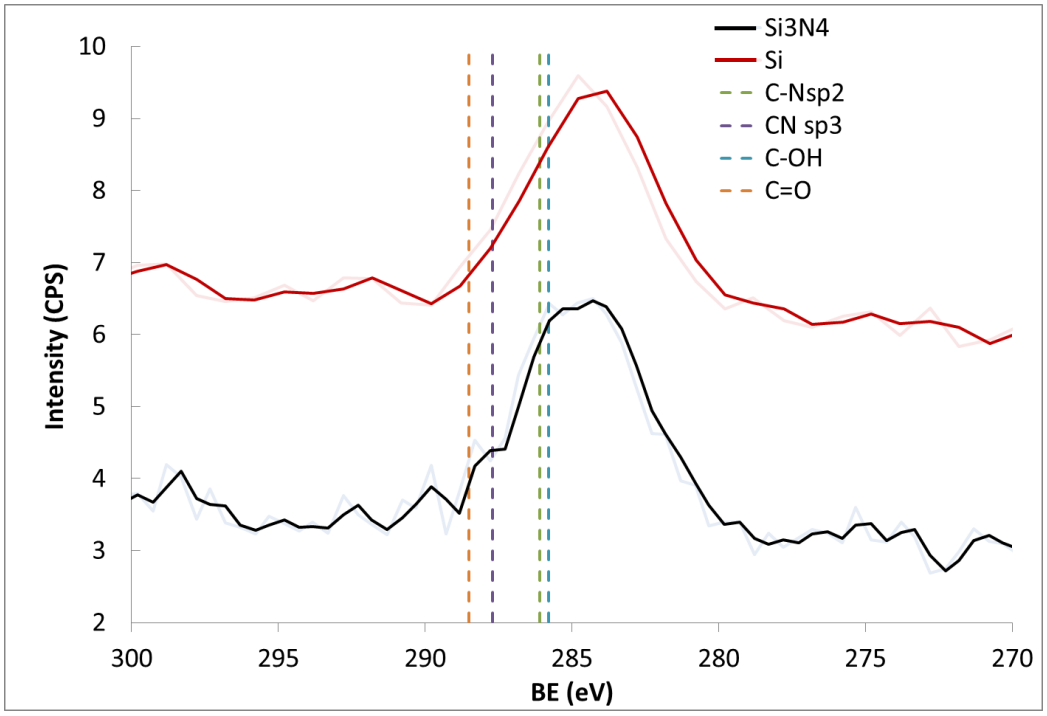

Figure 61. XPS spectra for C1s peak for deposited particles from 3N load @ 2cm/s reciprocated 250x × 6 lines at 0.75mm spacing on Si (top) and Si_3N_4 (bottom).

To properly identify the amount and nature of various C- bonds on the surface of the nanomaterials, XPSPeak V4.1 was used to fit Gauss-Lorentzian peaks at the specified binding energies and reconstruct (or conversely, deconvolute) the chemical species present. Using the knowledge about Si-C, C-N, and C=O bonds obtained from FTIR to set the peak fitting routine, the following parameters were used: 80% Gaussian weighting for the shape of the peak, full width at half maximum (FWHM) equal to 2.3, and invariable peak locations. An example of the resulting peak fitting procedure on Si3N4 is shown in Figure 62. The quantitative results showing composition from both samples is presented in Table 9 along with the peak positions. The results yielded that the samples were indeed quite similar with the exception that processing on Si_3N_4 yields a higher percentage of C-N sp^2 bonds, as predicted from the absorption spectra data. This information also helps to confirm the graphene backbone which has the sp^2 structure, since the sp^3 conjugation with N was so little. Nevertheless, the main component was the C-C bonds arising from the graphene backbone to the materials, but also showing a significant formation of C-Si bonds. Additionally, a reduced oxidation of the platelets was observed in the case of the Si_3N_4 substrate, suggesting that the excess N in the aqueous solution helped to reduce the oxygenated carbon terminals more completely, leaving behind the NH groups according to the reaction predictions by Kim[106] and Gao.[107] Alternatively, the additional presence of oxygen on the surface of the Si wafer which is oxidized as SiO_2 may encourage the stabilization of OH on the platelets despite the reducing action of N_2H_4. The relative reduction of C-OH groups as compared to C=O in the Si_3N_4 sample suggests that the OH groups are more sensitive to

the presence of NH compounds, or alternatively, that the SiO_2 surface promotes C=O bond formation during tribosynthesis.

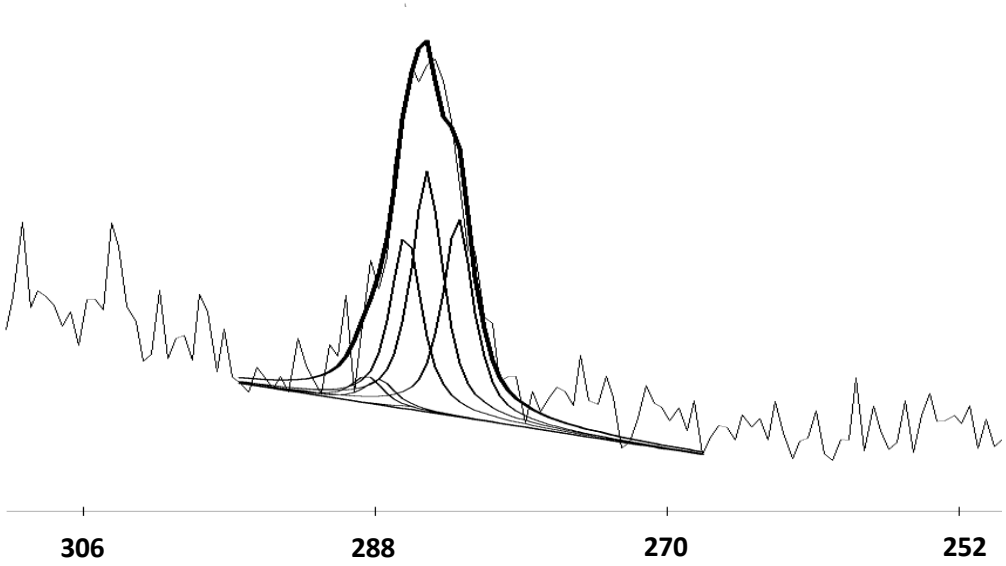

Figure 62. Peak fitting using XPS Peak 4.1 identifying carbon bonding from Si_3N_4 sample.

Table 9. Composition determined from XPS peak fitting.

		Composition (%)	
Bond description [ref]	**Peak location (eV)**	Si substrate	Si_3N_4 substrate
C-C	284.8	41.41	36.03
C=O [104,106]	288.5	0.51	3.99
C-OH [104,106]	285.9	10.05	0.45
CN sp^2 [140]	286.1	10.7	25.95
CN sp^3 [140]	287.7	9.1	3.8
C-Si [141]	282.9	28.22	29.77

4.2.4. Summary of Hydrazine tests

Here for the first time the production of mesoscopic (in between nano and macro scale) graphene sheets using a tribological approach. The characterization of the produced nanometer thick platelets found that they were surface functionalized, and perhaps "stitched" together, with the presence of C-N and C-Si bonds, which arise from the substrate material and hydrazine hydrate medium during sliding. The AFM results indicated a strong dependence on loading condition for the resulting platelet size, and also a dependence on the availability of carbon material to grow the materials as seen in the graphite suspended in $N_2H_4 \cdot H_2O$. Furthermore, the surface functionalization of nitrogen compounds can be removed using an argon anneal or vacuum oven as reported in previous GO reduction experiments using hydrazine.[21] Ultimately, a new route for the synthesis of graphenes has been demonstrated in tribosynthesis, which raises the question of whether other tribological methods are available using other chemistries. Moreover, is it possible to model and predict the behavior of the growth of the platelets as an engineered process? The next section will address a proposed method of modeling the synthesis as a chemical rate model.

5. ANALYSIS OF PARTICLE FORMATION

The production of new interfacial materials when contacting materials move relative to one another raises an important question. What is the driving force behind the chemical reaction taking place at the interface? The XPS and FTIR results presented in the previous section suggest that the tribosynthesis process leads to the stitching of graphenes via functional molecules on the surface, such as C-Si and C-N groups, leading to cascaded CMG nanoplatelets. Does the energy supplied for the reaction arrive from local heating or from frictional work? From the first law of thermodynamics, it is understood that the energy consumed by the reaction must be provided in some form, whether mechanically, thermally, electromagnetically, or some other energy source. In this case, the only legitimate energy sources are from mechanical and thermal inputs, for which the analysis in this section will address the influence of both and their relative importance.

5.1. Flash Temperature at Interface

When contacting surfaces are moved relative to one another, the friction at the interface has the effect of generating a local temperature rise, as known from pre-historic times with fire building. This work due to friction that results in heat generation, and arises from the conversion of energy from motion to heat as contacting materials slide past one another. This phenomena whose associated temperature rise has been come to known as the “flash temperature” has been of immense importance to mechanical systems design, such as engines, pumps, and many other mechanical devices that consist of moving components, as temperature fluctuations can be detrimental to system

performance. Furthermore, the irreversible energy losses associated with friction reduce the efficiency of such systems, and the development of lubricants and special chemical additives have been pursued as a means of combatting these losses. Even with good lubrication, the flash temperatures may still lead to performance problems, which is the reason for cooling systems being often incorporated with mechanical devices.

Some pioneering work in trying to determine the nature of the flash temperature at the interface of sliding materials was performed in the 1980's and 1990's[142,143,144] in order to best characterize the heat/energy generated at the surface. The following notation for the developed model follows that described in "Modern Tribology Handbook" by Bharat Bhushan.[145] To model the behavior of a sliding pin, it was represented as a uniform "heat source" for which the heat generated per unit contact area could be represented as:

$$q_{total} = \mu p U \tag{5.1}$$

where μ is the coefficient of friction, p is the contact pressure, and U is the sliding velocity. It is important to note that p may vary within the contact area, and furthermore, U represents a relative velocity if both surfaces are moving. According to the Fourier law of conduction,[146] the heat source acts as a boundary condition for the surface whose temperature (T) profile is determined according to:

$$\nabla^2 T = \frac{1}{\kappa}\frac{\partial T}{\partial t} \tag{5.2}$$

And

$$\kappa = \frac{k}{\rho C} \tag{5.3}$$

where k is the conductivity, ρ is the density and C is the heat capacity of the surface material. The modified Bessel function solution of the temperature profile can be shown to have a dependence on what is known as the non-dimensional Peclet number, which is defined as

$$Pe \equiv \frac{Ur}{2\kappa} \tag{5.4}$$

where r is the radius of the presumed circular contact area. If the contact area is a square, then it is half the side length of the square. For Pe<10, it was shown by Greenwood[143] that the max steady-state temperature rise for a uniform heat flux can be approximated by the following equation.

$$\Delta T_{max,flash} \cong \frac{2qr}{k\sqrt{\pi(1.273+Pe)}} \tag{5.5}$$

This equation assumes circular contact geometry, and other geometries result in a slightly modified expression. A list of other expressions and geometries is presented in Table 10, which was adapted from Bhushan's summary.[145] Additionally, it can be seen that for very small Pe (small velocities or contact area), the equation loses dependence on the Pe, and conversely as Pe becomes large, the 1.273 becomes insignificant.

Table 10. Flash temperature models for differing contact geometries and heat flux conditions. Adapted from reference.[145]

Geometry of Contact	Heat Flux distribution	SS Max Flash Temperature rise
Band (r=s/2)	Uniform	$\Delta T_{max,flash} \cong \frac{2qr}{k\sqrt{\pi(1+Pe)}}$
Square (r=s/2)	Uniform	$\Delta T_{max,flash} \cong \frac{2qr}{k\sqrt{\pi(1.011+Pe)}}$
Circle	Uniform	$\Delta T_{max,flash} \cong \frac{2qr}{k\sqrt{\pi(1.273+Pe)}}$
Circle	Parabolic	$\Delta T_{max,flash} \cong \frac{2.32qr}{k\sqrt{\pi(1.234+Pe)}}$
Ellipse (r=major axis radius)	Uniform	$\Delta T_{max,flash} \cong \frac{2qr}{k\sqrt{\pi(1.273Se+Pe)}}$ & Se≈2.448 (shape factor)

This maximum temperature reflects the steady state condition, which indicates there is a transitional period for this temperature to be achieved; however, Bhushan calculated the sliding distance required to reach SS as only 2.5 times r (the pin radius)[147]according to an earlier model by Jaeger.[148] Additionally, Yevtushenko et al.[149] predicted an instantaneous temperature rise to 87% of the SS temperature during sliding, suggesting that the temperature increase is mostly immediate.

To determine the average temperature rise on the surface, Tian et al.[144] used Green's theorem to solve Ling et al.'s[150] temperature solution profile such that

$$T_{ave} = \frac{8qr}{3\pi\kappa} \quad 5.6$$

Also, Tian explained that asperities undergoing plastic deformation actually exhibit less temperature rise than those purely elastically deformed,[144] so that the ratio of the two is represented by:

$$\frac{\Delta T_{elastic}}{\Delta T_{plastic}} \cong 1.16 \qquad 5.7$$

Furthermore, in the case of a reciprocating loading condition, such as that seen in the experiments described in this work, Tian and Kennedy[151] demonstrated both analytically and experimentally the transient temperature increase at a specific site that matches well with the SS condition at the interface of the tip. Additionally, the transient, periodic temperature profile shows an oscillation between the max temperature predicted by Eq. 5.5 and the ambient temperature, such that cascading temperature rise does not contribute to further temperature increase.[151]

Each of these researchers have sought both experimentally and analytically to understand this temperature rise on the surface during tribological contact, and often were concerned with temperature rises in gearboxes or electric motor brushes or automotive braking systems. But in the case of tribochemical activations, the flash temperature has been studied little.

5.2. Flash Temperature Model in Particle Formation

In the experiments enumerated in this work, the lateral size of the tribosynthesized CMG was seen to be heavily dependent on the contact pressure as shown earlier in Figure 33. Also, it is notable to mention that the best-fit model predicts a "zero-point" pressure, or the pressure at which a particle begins to form, at ~4.2 MPa average contact pressure. This suggests a threshold pressure corresponding to a required energy to initiate the reaction to tribosynthesize the CMGs. This idea correlates well to the notion of a chemical reaction rate, in which the progression of a reaction (in this

case, the formation of functionalized graphene nanoplatelets) is dependent on available energy and whether it surpasses a necessary activation energy. This relationship is best described by the Arrhenius equation below.

$$k = Ae^{-E_a/RT} \quad 5.8$$

Here k is the reaction rate constant, determined by the activation energy (E_a), and the reaction temperature (T), and R is the universal gas constant, and A is a reaction specific, pre-exponential factor. E_a and A must be determined experimentally, for which the activation energy is defined as:

$$E_a \equiv -R\left[\frac{\partial lnk}{\partial(1/T)}\right] \quad 5.9$$

If we redefine the Arrhenius relationship in terms of diameter and pressure, a tribosynthesis rate equation for CMG synthesis can now be represented as a chemical rate equation. Thus, letting k be proportional to diameter of particles (i.e. growth rate), and letting T be replaced by the pressure term, a well-defined pseudo-rate reaction is apparent as shown in Figure 63.

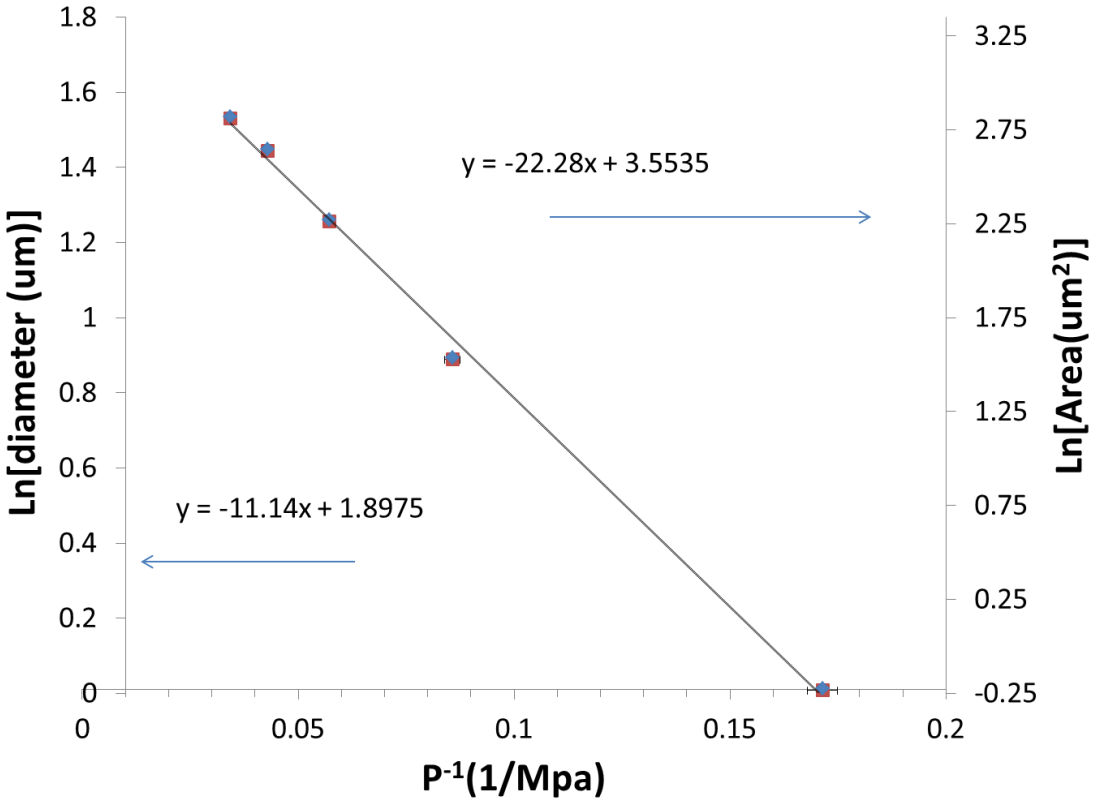

Figure 63. Psuedo-rate or reaction for the tribosynthesis of CMG's using diameter (or area) and pressure terms.

Using the Arrhenius analogy, we find an activation energy, which will be termed the "flash activation energy" in terms of average pressure of 8.314 × 11.14 = 92.62 J·MPa/K·mol, which also has the units of [cm^3·MPa^2/K·mol]. Additionally, it may be helpful to think of the rate in terms of area of the flake particles instead of diameter, since the area is proportional to the number of bonds formed during the reaction. Even so, the relationship remains the same, and the slope now increases by a factor of 2 according to the properties of logarithms, and the flash energy in terms of pressure now

becomes: 8.314 × 22.28 = 185.24 J·MPa/K·mol which also has the units of [cm^3·MPa^2/K·mol].

Alternatively, the pressure can be related to a surface temperature via the flash temperature model given in Equation 5.5. If we apply the relationship between pressure and temperature according to flash temperature principle, the temperature (for a circular contact area) can be represented as:

$$T_{flash} = \frac{2pU \cdot \mu \cdot r}{k\sqrt{\pi(1.273+Pe)}} + T_{ambient} = \frac{2U \cdot \mu \cdot \sqrt{pL}}{k\pi\sqrt{(1.273+Pe)}} + T_{ambient} \qquad 5.10$$

which is an implicit equation of "r" (contact radius) via the Peclet #. In the second expression, the radius of contact (r) is translated in terms of pressure (p) and applied load (L). Translating the average pressure into flash temperature now yields a reaction rate with temperature dependence as charted in Figure 64. Here the temperature is represented in terms of 10000/T in order to facilitate easier interpretation.

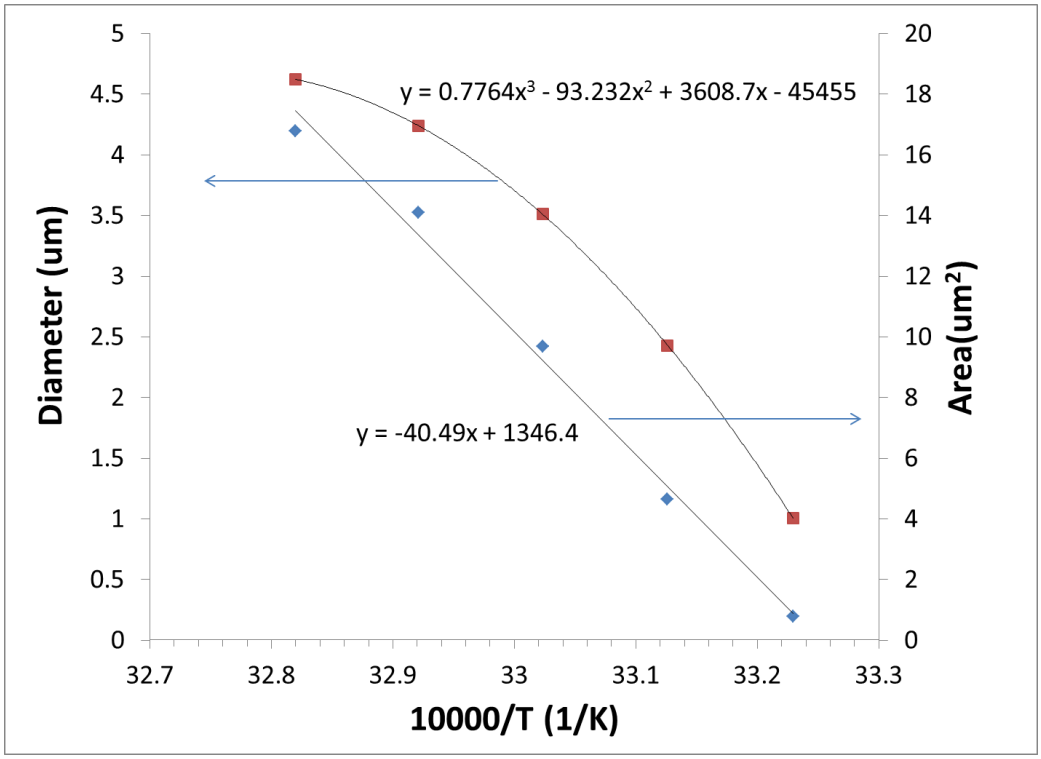

Figure 64. Reaction rate represented in terms of inverse flash temperature.

Here, it is seen that the particle diameter loses its "linear" relationship, but the area (proportional to # of bonds) retains nice behavior, indicating that indeed it is more representative of the rate of reaction. However, the relationship between the area and inverse temperature is no longer obtained through the ln(A), suggesting that the area is actually proportional to ln(k) instead of k itself. Or,

$$A_{particle} = C \cdot \ln(k) \qquad 5.11$$

where C is a proportionality constant. If this is the case, then the flash activation energy can be represented as

$$E_a = -\frac{R}{C} \cdot \frac{\partial A}{\partial (T^{-1})} \quad 5.12$$

so that for this experiment, $E_a = C^{-1} \cdot 3{,}366$ kJ/mol.

Since we know that the activation energy is related to the friction energy required to initiate the formation of the particles, we can use our zero-point pressure (4.2MPa) to find the associated "zero-point flash temperature" (300.86K), and calculate the energy via the Boltzmann relationship:

$$E = k_b T = 1.38E^{-23} \left[\frac{J}{K}\right] \times 300.86\,[K] \times 6.022E^{23} \left[\frac{atom}{mol}\right] = 2500.3 \left[\frac{J}{mol}\right]$$

Equating this number to the previously derived E_a we find that C=1346.5 m^2. Unfortunately, this activation energy is rather low, considering the bond enthalpy (or dissociation energy) for many of the bonds present in our synthesized material (see Figure 60) would not be satisfied by that energy supply (see Table 11 for relevant bond energies). This is largely the result of low flash temperatures that arise from the relatively low sliding velocities and pressures present in our system. As a reference, an example of the calculation of the max flash temperature rise is given below for a representative case from the tribosynthesis tests. In this example, a 3N load traveling at a maximum velocity of 0.5cm/s is distributed over a 467 μm diameter circular pin geometry (total area), as seen in the results section.

Table 11. Relevant bond energies[137,152]

Bond Type	Bond Enthalpy
C≡C (alkyne)	837 kJ/mol
C=C (alkene)	620 kJ/mol
C-C (alkane)	347-356 kJ/mol
C-N	304 kJ/mol
C-O	356 kJ/mol
C=O	742 kJ/mol
C-Si	301 kJ/mol

q=0.2×3N×0.5cm/s=0.3 N-cm/s / (pi×0.0233^2) = 175.9N/cm-s

Pe=V×a×rho×C/2k=0.5cm/s×0.0233cm×2.198g/cm^3×0.703J/g/K / (2×0.0114W/cm/K)

= 0.7895

ΔT_{max}=2×175.9N/cm-s×0.0233cm/(1.14N-cm/cm/K×sqrt(3.14×(1.273+Pe)))= 2.83K

In this example, the maximum temperature rise is quite small, having only 3 K increase from the initial condition. This calculation (and the previous charts and values) assume an averaged contact area over the entire test area. According to the model, as the contact area decreases, the localized pressure can induce much higher temperatures. However, this assumes that the contact load is transmitted through a single point or asperity, where in reality the load is distributed between multiple contact points within the nominal or average contact area. Assuming the particles are distributed fairly uniformly, ultimately, the flash temperature behavior at the interface is still an averaged value, just with slightly different contact behavior based on the statistical distribution of particles at the surface. For the test conditions used to find the reaction rate expressions, the maximum flash temperature increase for the given conditions was ~6K when

considering only the nominal/averaged contact area, but it is useful to know if this value underrepresents the true flash temp based on presumed asperity contact. If we define a statistical term, δ, which represents the average periodicity of asperities or third-body particles at the interface of the pin and substrate, we can now re-write our flash temperature equation in terms of this periodicity factor. Defining this parameter as the average length between adjacent asperities (l_a) relative to the asperity radius (r*),

$$\delta = {}^{l_a}/_{r^*} \tag{5.13}$$

its value can be experimentally determined by relating this periodicity factor to the number of particles/asperities per unit area (#). I.e. the observed particles per area can be also explained in terms of the periodicity factor by a geometric relationship based on the length between asperities such that:

$$\# = {}^{1}/_{(\delta r^*)^2} \tag{5.14}$$

Schematically, this is explained in Figure 65, where the reciprocal of the shaded area is equivalent to # (Eq. 5.14).

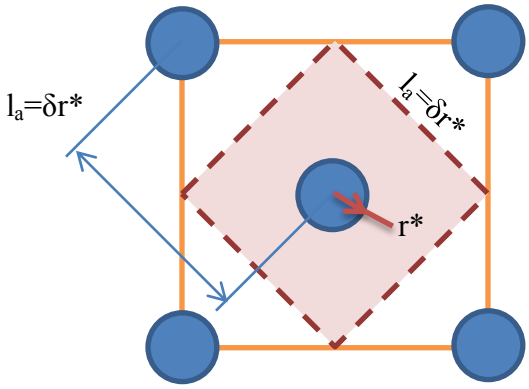

Figure 65. Schematic showing relationship between asperity radius (blue circles) and periodicity factor

With asperities or third body particles carrying the nominal load (L), the distributed load (L*) on each of the particles under the nominal contact area (A_{nom}) can be represented as

$$L^* = \frac{L}{\#\cdot A_{nom}} = \frac{L(\delta r^*)^2}{A_{nom}} \tag{5.15}$$

and the particle's new contact area can be represented as A*. Using the distributed loads over the asperity area to define a local contact pressure (p*), the localized asperity flash temperature (ΔT*) can be calculated as:

$$\Delta T^*_{max,flash} \cong \frac{2L\delta^2 r^* U\mu}{A_{nom}\pi^{3/2}k\sqrt{1.273+Pe^*}} \tag{5.16}$$

and

$$Pe^* \equiv \frac{Ur^*}{2\kappa} \tag{5.17}$$

Using this approach, the flash temperature function is more sensitive to the asperity periodicity than the radius alone. Furthermore, the Flash temperature increases

almost linearly with particle/asperity radius for a constant periodicity (or equivalently, a decrease in # in inverse proportion to r^{*2} – see Eq. 5.14). This contrasts starkly with the inverse relationship between the flash temperature and the particle size for a single point contact, because, ultimately, the load will be carried through multiple contact locations rather than a single point. The graph in Figure 66, shows the two competing flash point mechanisms (single point contact versus distributed loads), for various periodicity values. The curves were plotted using a 5N load over a nominal area having a diameter of 467 μm (determined from expermental measurements), with a sliding velocity of 5mm/s and average μ=0.2 sliding on Si. As seen in the chart, depending on the value of δ, the single point contact curve and the distributed load curves intersect. This intersection corresponds to the point at which the contact area of a single point (A_{nom}) equals the area of a single "period" of the distributed contact points. I.e.

$$A_{nom} = A_{per,dist}$$

$$\pi r^2 = (\delta r^*)^2 \qquad 5.18$$

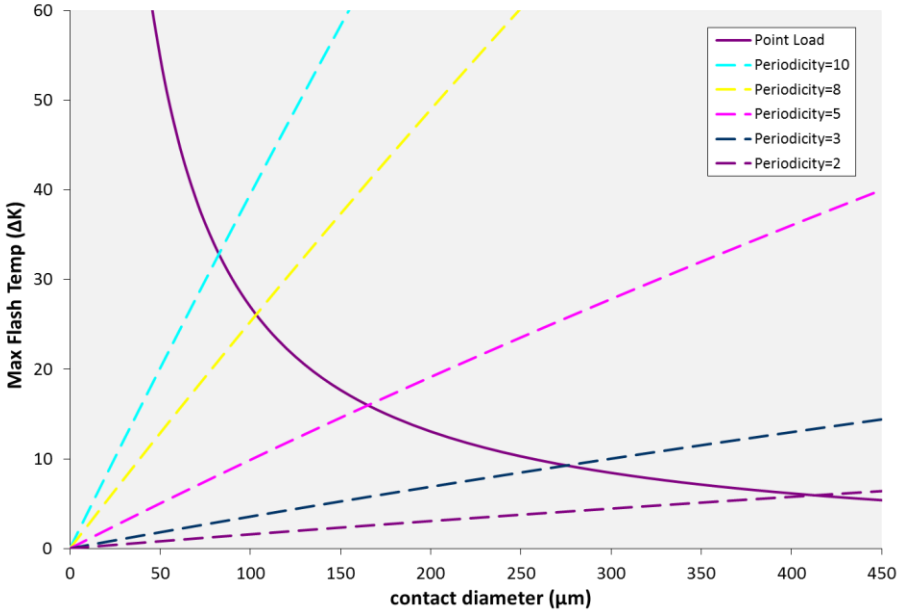

Figure 66. Maximum flash temperature for single point and distributed loading. Intersection of lines for a given periodicity factor indicate the absolute maximum temperature rise for a given nominal contact area.

As such, this intersection corresponds to a maximum temperature rise that can occur as a result of a distributed load under a nominal contact area. The result is a balance between single point contact and distributed loads via multiple asperities or third-body particles. Above this intersection point, the single particle behavior dominates, whereas below, the distributed behavior takes over. Thus, a critical asperity/particle radius (r_{crit}^{*}) can be defined according to the periodicity factor.

$$r_{crit}^{*} = \frac{\sqrt{\pi}\cdot r}{\delta} \tag{5.19}$$

Therefore, the true maximum for a distributed load can be determined using the critical asperity radius in the flash temperature equation.

$$\Delta T_{max,flash} \cong \frac{2qr_{nom}}{\delta\cdot k\sqrt{(1.273+Pe)}}$$

or

$$\Delta T^*_{max,flash} \cong \frac{2L\delta U\mu}{\pi^2 r_{nom} k\sqrt{1.273+Pe^*}} \quad 5.20$$

Here, r_{nom} is the radius of the nominal contact area. It is interesting to note that at the minimum periodicity, δ=2 (when adjacent particles are touching), the critical radius is just slightly less than the nominal radius. Or,

$$\frac{r^*_{crit}}{r_{nom}} = \frac{\sqrt{\pi}}{2} \approx 0.886 \quad 5.21$$

Additionally, we see that the flash temperature has a second-order dependence on the periodicity, as illustrated in Figure 67, and its sensitivity to the periodicity increases as the asperity size increases. This indicates that the localized flash temperatures at extremely small asperity sizes are essentially negligible, but as the size increases, it becomes immensely important.

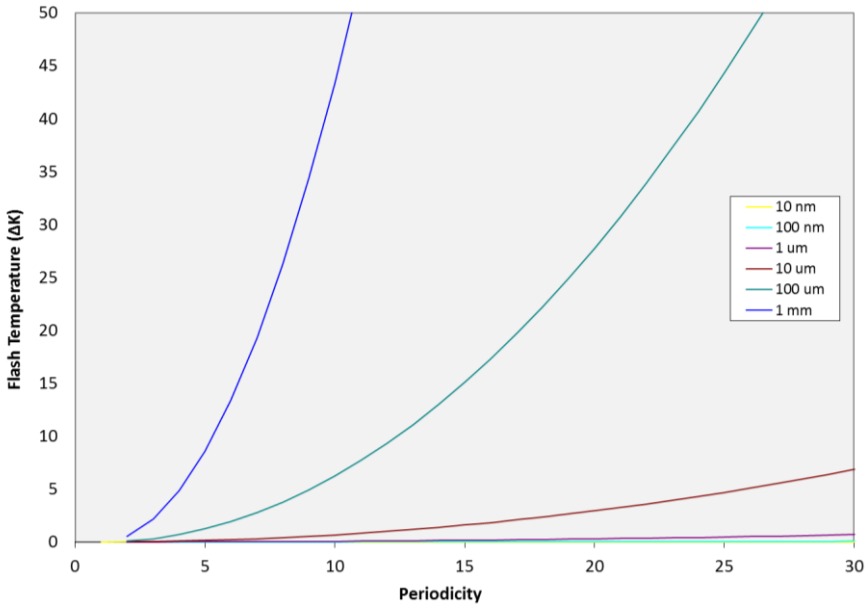

Figure 67. Flash temperature rise versus periodicity factor for various size asperities/particles

Statistically, we can determine the value of δ from observing the debris on the surface of the samples. For example, Figure 68 shows the presence of debris particles that presumably play a role in the formation of the nanoplatelets which are also seen (though dimmer) on the surface of the Si. According to the definition of δ set forth in Eq. 5.14, the experimentally measured periodicity is approximately 8.

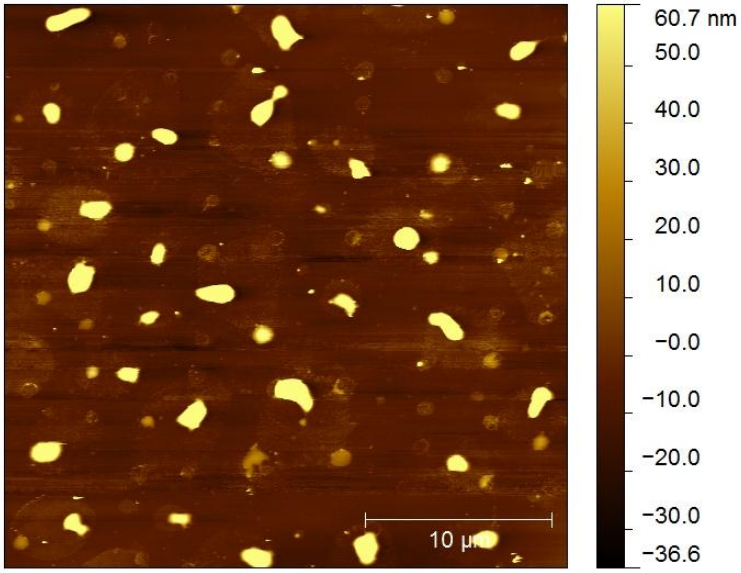

Figure 68. AFM image of debris particles (bright circles) on top of nanoplatelets (fainter circles) resulting from processing at 3N, 2 cycles, and 0.5 cm/s maximum velocity.

Considering that the max temperature as a result of flash heating by friction is obtained at a critical asperity radius, if we assume the maximum condition is met, we find that the highest possible temperature rise for our test conditions is approximately 3 degrees per newton of loading. An updated chemical rate analysis with the Arrhenius

equations yields $E_a=C^{-1}\cdot 1{,}092$ kJ/mol, and using an updated zero-point flash temperature condition, the corresponding Ea=2,511 J/mol, and C=434.8 m^2. However, including the energy resulting from the strain at the interface, according to the activation suggested by J.J. Gilman[100] a strain induced activation energy can be calculated according to

$$E_{strain} = \frac{F^2}{2k_{spring}} = \frac{F^2 t}{2AE} \tag{5.22}$$

where F is the force acting at the interface, t is the length or thickness of the strained interfacial material in the direction of strain (which we'll assume to be the characteristic thickness of the CMG), A is the cross section area of the strained material and E is the Young's modulus which is related to the spring constant of the material (k_{spring}). Taking the net force acting at the interface as the magnitude of the shear from friction and the normal load,

$$\|F\| = (L^2 + \mu^2 L^2)^{1/2} = L\sqrt{1+\mu} \tag{5.23}$$

the strain energy can be alternately represented as:

$$E_{strain} = \frac{L^2(1+\mu)t}{2AE} = \frac{p^2(1+\mu)tA}{2E_{int}} \tag{5.24}$$

Additionally, the interface modulus (E_{int}) can be determined according to

$$E_{int} = \left[\frac{1}{E_1} + \frac{1}{E_2}\right]^{-1} \tag{5.25}$$

which, for the graphite-silicon interface is 11.19 GPa (dominated by graphite). Calculating the energy provides the net energy supplied at the interface, and normalizing the energy by the particle size and assuming the planar surface density of the CMG to be the same as graphene (9.28×10^{18} atoms/m^2), the relationship between particle formation

size and specific strain energy (kJ/mol) can be determined as shown in Figure 69. As the particle size decreases, the specific strain increases rapidly due to the small area, whereas the increasing pressure/size relationship drives the increase in specific strain on the upper portion of the curve. In the chart, the diamond-shaped data points reflect actual measured values, whereas the line represents the pressure-area relationship defined by the logarithmic relationship shown in Figure 63. According to the predicted value, the model predicts an energy barrier of ~39 kJ/mol for the given test conditions. Curiously, this minimized energy for producing the CMG nanoplatelets occurs precisely along the test conditions which produced the maximum particle surface density/coverage in the sliding area of the tribosynthesis CTE tests (see Figure 34). This observation is an astute validation the energy barrier model, which suggests that the synthesis proceeds most easily at this minimum energy condition resulting in the formation of greater numbers of particles at the interface at near the minimum energy condition. Furthermore, this suggests that the activation energy can actually be represented as the sum of this strain energy barrier and the zero-point flash temperature ($T_{flash,z.p.}$) energy.

$$E_a = E_{Sb} + RT_{flash,z.p.} \quad 5.26$$

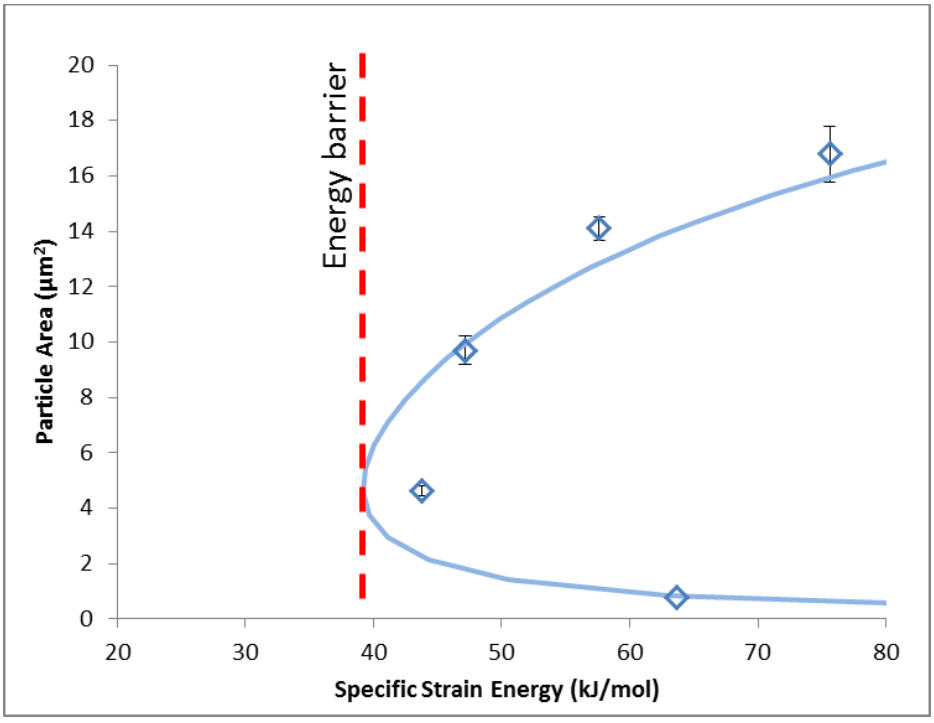

Figure 69. Energy barrier for strain energy. Experimental data points shown overlaid onto curve predicted from observed logarithmic relationship between pressure and particle area.

As such, the activation energy for tribosynthesis of the CMG developed in this work is ~41.6 kJ/mol, which prescribes that the proportionality constant C=26.3 m^2. The intriguing insight obtained from this value is that it falls directly in the range of the differences between the C-O or C-C and C-N or C-Si bonds (see Table 11). In other words, the primary bond formations observed by XPS and FTIR from the original graphite, which is terminated with C-C and C-O bonds, require 40-50 kJ/mol of energy input to replace the existing bond terminations.

From previous works, we know that strain and temperature don't simply lead to bond replacement; however, the energy input at the surface initiates these reactions via

the emission of "low-energy" elections or exoelectrons, from which incomplete electronic structures arise on the surface atoms. This leads to the formation of new bonds to lower the surface energy. [153,154] Previous works predicted and measured the emission of these electrons to have energies primarily in the range of 1-4 eV which then react with molecules in the sliding medium to form ions and radicals which are prone to react with the surfaces.[99,103,155] Curiously, these predictions represent one order of magnitude greater energy than the energy barrier predicted from these experiments, assuming that each surface atom ejects an electron. However, as explained by Kajdas,[155] the electrons can be assumed to only be emitted from the tops of asperities, for which a reduction by the periodicity factor (representative of the asperities per area) observed to be ~8 matches extremely well with Kajdas and Molina's previous calculations and experiments in organometallic formations on lubricated surfaces.[103,154] Moreover, Buyanovsky[156] acknowledged the formation of interfacial structures in heavy contact loadings having 2-8nm thicknesses that formed through the combined action of deformation, diffusion, friction heat, and chemical reactions at the surface. This film forms as a means to passivate the friction activated surface, such that Buyanovsky observed that ~90-98% of the friction energy is transferred into these interstitial films.[156] These results corroborate the idea that the friction energy is supplied into the interface such that the natural thermodynamic inclination toward lower energy favors the formation of the interfacial films, and that the calculated energies are appropriate estimations for the amount of energy supplied to the interface.

5.3. Summary

In the previous calculations and analytical look at flash temperatures, the fact is revealed that the energy supplied for bond formation is predominantly the result of strain at the interface, and flash temperature contributes minimally to the overall reaction rate. This is also supported by Buyanovsky's assertion that the elastic-plastic deformation is the primary activating factor during tribochemical reactions.[156] The subsequent conclusion is that the reaction proceeds nearly athermally, although local temperatures do increase slightly. Furthermore, the reaction can be explained in terms of an Arrhenius-type rate equation, for which the pressure or flash temperature can be used to describe the "flash activation energy," whether in terms of pressure (185.24 J·MPa/K·mol) or flash temperature and strain (41.6 kJ/mol).

6. CONCLUSION

The research presented herein investigated the use of a tribological technique to synthesize graphene based nanomaterials. This approach is an entirely new methodology in nanofabrication and synthesis of graphenes, and even showed exceptional success in producing graphenes of large dimensions, when compared to typical colloidal-type fabrication methods.

In this work, a single-step tribosynthesis procedure was introduced for the fabrication of graphene-based nanoplatelets as a result of tribochemical surface reactions. The resulting nanomaterials were found to exhibit the lamellar nature of graphite, having a characteristic thickness of 2-2.5nm. The added thickness beyond the graphene dimension of 4 angstroms comes as a result of the surface functionalizations, having C-Si, C-N, C-O bonding and loosely attached OH groups. The lateral size of the resulting particles was demonstrated to be a function of the contact pressure, for which an activation energy of 41.6 kJ/mol was calculated based on the input strain energy and local flash temperatures during the sliding process.

Using a two-body friction approach, the nanoplatelets were shown to have diameters in the 1-10 μm, while maintaining the characteristic thickness, which is comparable to multi-step colloidal graphene synthesis. When using a three-body friction approach, having suspended graphite particles in solution of hydrazine hydrate, the platelet size was observed to jump considerably to diameters of 100 μm, which is much greater dimensions than seen using other traditional methods.

The three-body approach resulted in larger sizes primarily as a result of higher contact stresses combined with the increased chemical availability due to the suspended graphite in the solution. These large particles exhibited thicknesses of ~30 nm but also exhibiting lamellar behavior with the characteristic dimensions. The largest platelets exhibited rippling or folding on the surface of the platelets, which can be expected as a combined result of the sliding procedure and reducing the overall surface energy of such large platelets. The additional advantage of the tribosynthesis approach is that the process directs the assembly of the nanoplatelets at a specific location, rather than random dispersions from colloidal suspensions. Furthermore, it produces relatively uniform sizes and thicknesses, which is comparable to or even better than other typical chemical approaches.

6.1. Broader Impacts

Having demonstrated a new approach to the direct synthesis of graphene-based materials on the surface of silicon, this technique offers a new approach to nano-electronics fabrication. Furthermore, graphene has been touted as an ideal material for molecular electronics, having a unique electronic structure that enables its use as both an ultra-conductive material and as a field effect transistor. In this work, a new reaction pathway was discovered for the production of mesoscopic graphene platelets with modified surface functionality. This one-step procedure demonstrated the ease of producing these chemically modified graphenes directly on a semi-conductor substrate, which could be easily adapted into the integrated circuit design process for creating nano-electronics. Moreover, the direct-write procedure could be scaled down to

nanometer lengths such that high localized stresses could be obtained at a very small scale, such that nanometer dimension wires could conceivably be produced. And even though the surface functionalities present in the samples discussed in this report are not pristine graphene, a number of chemical methods for restoring graphene structure to CMGs have been developed and discussed elsewhere.

Additionally, the unique optical properties of graphenes make it an excellent candidate for solar energy collection and conversion, and a directed assembly procedure such as the tribosynthesis technique presented herein may offer new opportunities for development of solar collectors with a combination of structural and optically based light trapping mechanisms.

Ultimately, the exciting nature of graphene and its unique properties offer a myriad of technological opportunities if the production methods are capable of delivering a graphene product of desirable size and functionality. This new tribosynthesis approach offers a fresh and different methodology for obtaining desirable sizes and uniformity among its synthesized products. It may very well be the portal to future development of graphene-based materials technologies.

6.2. Future Recommendations

The development of these graphene products have been demonstrated using a tribological technique; however, further development will lead to the actual integration of this method with existing technologies. Ideally, a continuous graphene sheet could be patterned directly, and in order to accomplish that the process would have to be optimized to facilitate that formation. Based on observations from these experiments

and other literature references to tribochemistry, the following actions and areas are recommended for further study.

- Tribocatalysis: using a catalyst agent to aid in the formation of the graphene, and reduce the required strain energy to obtain large formations.
- Nanoscale replication: using an AFM-based system to facilitate nanoscale contact to increase local pressures while maintaining small contact area. Furthermore it would be representative of a process used to pattern nanowires into a circuit.
- Lattice optimization: As graphene can behave differently in terms of its electronic transport properties, if a relationship between the tribo-induced strain and the lattice directions could be established, a functional development of directionally synthesized graphenes could conceivably be established.

Using this newly developed tribosynthesis technique, it has been shown that graphene features can be written on a Si surface. With further development it may be possible to use a pencil – one of the simplest tools – to create advanced circuitry more powerful and faster than any existing method.

REFERENCES

[1] K. S. Novoselov, A. K. Geim, S. V. Morozov, D. Jiang, M. I. Katsnelson, I. M. Grigorieva, S. V. Dubonos, and A. A. Firsov, Nature **438**, 197 (2005); K. S. Novoselov, E. Mccann, S. V. Morozov, V. I. Fal'ko, M. I. Katnelson, U. Zeitler, D. Jiang, F. Schedin, and A. K. Geim, Nature Physics **2**, 177 (2005); K. S. Novoselov, A. K. Geim, S. V. Morozov, D. Jiang, Y. Zhang, S. V. Dubonos, I. V. Grigorieva, and A. A. Firsov, Science **306**, 666 (2004).

[2] A. K. Geim and K. S. Novoselov, Nat Mater **6** (3), 183 (2007).

[3] H. P. Boehm, R. Setton, and E. Stumpp, Pure and Applied Chemistry **66** (9), 1893 (1994).

[4] C. Lee, X. Wei, J. W. Kysar, and J. Hone, Science **321** (5887), 385 (2008).

[5] T. J. Booth, P. Blake, R. R. Nair, D. Jiang, E. W. Hill, U. Bangert, A. Bleloch, M. Gass, K. S. Novoselov, M. I. Katsnelson, and A. K. Geim, Nano Letters **8** (8), 2442 (2008).

[6] A. A. Balandin, S. Ghosh, W. Bao, I. Calizo, D. Teweldebrhan, F. Miao, and C. N. Lau, Nano Letters **8** (3), 902 (2008).

[7] J.-H. Chen, C. Jang, S. Xiao, M. Ishigami, and M. S. Fuhrer, Nat Nano **3** (4), 206 (2008).

[8] R. R. Nair, P. Blake, A. N. Grigorenko, K. S. Novoselov, T. J. Booth, T. Stauber, N. M. R. Peres, and A. K. Geim, Science **320** (5881), 1308 (2008).

[9] P. R. Wallace, Physical Review **71** (9), 622 (1947).

[10] J. Liu, A. R. Wright, C. Zhang, and Z. Ma, Applied Physics Letters **93** (4), 041106 (2008); Y. Zhang, T.-T. Tang, C. Girit, Z. Hao, M. C. Martin, A. Zettl, M. F. Crommie, Y. R. Shen, and F. Wang, Nature **459** (7248), 820 (2009).

[11] Y. Zhang, Y. W. Tan, H. L. Stormer, and P. Kim, Nature **438**, 201 (2005).

[12] A. K. Geim and A. H. Macdonald, Physics Today **60** (8), 35 (2007).

[13] G. Eda, G. Fanchini, and M. Chhowalla, Nature Nanotechnology **3** (5), 270 (2008).

[14] X. Wang, L. Zhi, and K. Mullen, Nano Lett. **8**, 323 (2008).

[15] P. Blake, Nano Lett. **8**, 1704 (2008).

[16] I. W. Frank, D. M. Tanenbaum, A. M. Van Der Zande, and P. L. Mceuen, J. Vac. Sci. Technol. B **25**, 2558 (2007).

[17] W. S. Hummers and R. E. Offeman, J. Am. Chem. Soc. **80**, 1339 (1958).

[18] L. Staudenmaier, Ber. Deut. Chem. Ges. **31**, 1481 (1898).

[19] V. C. Tung, M. J. Allen, Y. Yang, and R. B. Kaner, Nature Nanotech. **4**, 25 (2008).

[20] S. Gilje, S. Han, M. Wang, K. L. Wang, and R. B. Kaner, Nano Letters **7** (11), 3394 (2007).

[21] S. Park and R. S. Ruoff, Nat Nano **4** (4), 217 (2009).

[22] D. Li, M. B. Muller, S. Gilje, R. B. Kaner, and G. G. Wallace, Nature Nanotech. **3**, 101 (2008).

[23] J. I. Paredes, S. Villar-Rodil, A. Martinez-Alonso, and J. M. D. Tascon, Langmuir **24**, 10560 (2008).

[24] R. Muszynski, B. Seger, and P. V. Kamat, J. Phys. Chem. C **112**, 5263 (2008).

[25] G. Williams, B. Serger, and P. V. Kamat, ACS Nano **2**, 1487 (2008).

[26] Y. Hernandez, Nature Nanotech. **3**, 563 (2008).

[27] N. Liu, Adv. Funct. Mater. **18**, 1518 (2008).

[28] D. Bratton, D. Yang, J. Dai, and C. K. Ober, Polymers for Advanced Technologies **17** (2), 94 (2006).

[29] V. Yuli, A. Bourdillon, O. Vladimirsky, W. Jiang, and Q. Leonard, Journal of Physics D: Applied Physics **32** (22), L114 (1999).

[30] S. Y. Chou, P. R. Krauss, and P. J. Renstrom, Applied Physics Letters **67** (21), 3114 (1995).

[31] J. Neddersen, G. Chumanov, and T. M. Cotton, Applied Spectroscopy **47**, 1959 (1993).

[32] K. Scow, Proceedings of Semiconductor Integrated and Production Conference and Exhibition, 9-11 Feb. 1971, Chicago, IL, USA, 1971.

[33] A. Chatterjee, A. Datta, A. K. Giri, D. Das, and D. Chakravorty, Journal of Applied Physics **72**, 3832 (1992); Z. Ji, L. Longtu, G. Zhilun, Z. Xiaowen,

and D. J. Barber, Nanostructured Materials **8**, 321 (1997); H. Kozuka, M. Okuno, and T. Yoko, Journal of the Ceramic Society of Japan **103**, 1305 (1995).

[34] L. Peng, H. Lee, W. Teizer, and H. Liang, Wear **267** (5-8), 1177 (2009).

[35] K. Salaita, Y. Wang, and C. A. Mirkin, Nat Nano **2** (3), 145 (2007).

[36] Y. Zhang, J. P. Small, W. V. Pontius, and P. Kim, Applied Physics Letters **86** (7), 073104 (2005).

[37] P. Balaz, *Mechanochemistry in Nanoscience and Minerals Engineering*. (Springer-Verlag, Berlin Heidelberg, 2008).

[38] J. J. Gilman, Science **274** (5284), 65 (1996).

[39] V. V. Boldyrev, Russian Chemical Reviews **75** (3), 177 (2006).

[40] P. A. Thiessen, G. Heinicke, and E. Schober, Zeitschrift für anorganische und allgemeine Chemie **377** (1), 20 (1970).

[41] M. K. Beyer and H. Clausen-Schaumann, Chemical Reviews **105**, 2921 (2005).

[42] J. E. Jones, Proceedings of the Royal Society of London. Series A **106** (738), 463 (1924).

[43] C. J. Eckhardt, Molecular Crystals & Liquid Crystals **456** (1), 1 (2006).

[44] J. Ribas-Arino, M. Shiga, and D. Marx, Angewandte Chemie - International Edition **48**, 4190 (2009).

[45] P. Baláz and E. Dutková, Minerals Engineering **22** (7-8), 681 (2009).

[46] L. Takacs, Journal of Materials Science **39** (16), 4987 (2004).

[47] C. Suryanarayana, Progress in Materials Science **46** (1-2), 1 (2001).

[48] J. S. Benjamin, Materials Science Forum **88 - 90** (Mechanical Alloying), 1819 (1992).

[49] M. K. Beyer and H. Clausen-Schaumann, Chemical Reviews **105** (8), 2921 (2005).

[50] J. Sohma, Progress in Polymer Science **14** (4), 451 (1989).

[51] K. Tkáčová, *Mechanical Activation of Minerals*. (Elsevier, Amsterdam 1989).

[52] E. Gock, *Mechanische Aktivierung von Phosporitkonzentraten im Hinblick auf den direkten Einsatz als Düngemitte.* (Technical University Berlin, 1987).

[53] J. Amgalan, M. V. Chaikina, M. Dulamsuren, and A. Bilegbaatar, Chemistry for Sustainable Development **6**, 221 (1998).

[54] S. Biangardi and H. Pietsch, Proceedings of Symposium on Hydrometallurgy, The Institution of Chemical Engineers Symposium Manchester 1975; S. Biangardi and H. Pietsch, Erzmetall **29** 73 (1976).

[55] I. J. Corrans and J. E. Angove, Minerals Engineering **4** (7-11), 763 (1991); C. M. Palmer and G. D. Johnson, JOM **57** (7), 40 (2005).

[56] P. Baláž and M. Achimovičová, Hydrometallurgy **84** (1-2), 60 (2006).

[57] L. Turčániová, J. Kádárová, P. Imrich, T. Liptaj, J. Vidlář, J. Vašek, F. Foldyna, J. Sitek, and P. Baláž, Journal of Materials Science **39** (16-17), 5467 (2004).

[58] G. Kaupp, *Solid-State Reactions with 100% Yield*. (Springer/Heidelberg, Berlin 2005); G. Kaupp, J. Schmeyers, M. R. Naimi-Jamal, H. Zoz, and H. Ren, Chemical Engineering Science **57** (5), 763 (2002); D. Braga and F. Grepioni, Angewandte Chemie - International Edition **43** (31), 4002 (2004).

[59] E. L. Parrott, Journal of Pharmaceutical Sciences **63** (6), 813 (1974).

[60] A. V. Dushkin, Chemistry for Sustainable Development **12**, 251 (2004).

[61] D. Huitink, L. Peng, R. Ribeiro, and H. Liang, Applied Physics Letters **94** (18), 183111 (3 pp.) (2009).

[62] D. Huitink, F. Gao, K. Wang, and H. Liang, Electrochemical and Solid-State Letters **13** (9), F16 (2010).

[63] T. Tsuzuki and P. G. McCormick, Journal of Materials Science **39** (16), 5143 (2004).

[64] T. Tsuzuki and P. G. McCormick, Nanostructured Materials **12** (1-4), 75 (1999).

[65] M. Achimovicova, K. Lucenildo Da Silva, N. Daneu, A. Recnik, S. Indris, H. Hain, M. Scheuermann, H. Hahn, and V. Sepelak, Journal of Materials Chemistry **21** (16), 5873 (2011).

[66] J. Ding, W. F. Miao, P. G. McCormick, and R. Street, Applied Physics Letters **67** (25), 3804 (1995).

[67] J. Ding, T. Tsuzuki, P. G. McCormick, and R. Street, Journal of Physics D: Applied Physics **29** (9), 2365 (1996).

[68] J. Ding, T. Tsuzuki, P. G. McCormick, and R. Street, Journal of Alloys and Compounds **234** (2), L1 (1996).

[69] J. Ding, T. Tsuzuki, and P. G. McCormick, Journal of the American Ceramic Society **79** (11), 2956 (1996).

[70] J. Ding, T. Tsuzuki, and P. G. McCormick, Nanostructured Materials **8** (1), 75 (1997).

[71] T. Tsuzuki, E. Pirault, and P. G. McCormick, Nanostructured Materials **11** (1), 125 (1999).

[72] T. Tsuzuki and P. G. McCormick, Journal of the American Ceramic Society **84** (7), 1453 (2001).

[73] T. Tsuzuki and P. G. McCormick, Acta Materialia **48** (11), 2795 (2000).

[74] T. Tsuzuki, P. McCormick, Nbsp, and G, Materials Transactions **42** (8), 1623 (2001).

[75] L. M. Cukrov, T. Tsuzuki, and P. G. McCormick, Scripta Materialia **44** (8-9), 1787 (2001).

[76] J. Ding, T. Tsuzuki, and P. G. McCormick, Nanostructured Materials **8** (6), 739 (1997).

[77] T. Tsuzuki and P. G. McCormick, Scripta Materialia **44** (8-9), 1731 (2001).

[78] T. Tsuzuki, J. Ding, and P. G. McCormick, Physica B: Condensed Matter **239** (3-4), 378 (1997).

[79] T. Tsuzuki and P. G. McCormick, Applied Physics A: Materials Science & Processing **65** (6), 607 (1997).

[80] T. Tsuzuki, K. Pethick, and P. G. McCormick, Journal of Nanoparticle Research **2** (4), 375 (2000).

[81] K. Fujiwara and K. Komatsu, Organic Letters **4** (6), 1039 (2002); X. Cheng, G. W. Wang, Y. Murata, and K. Komatsu, Chinese Chemical Letters **16** (10), 1327 (2005).

[82] K. D. Ausman, H. W. Rohrs, M. Yu, and R. S. Ruoff, Nanotechnology **10** (3), 258 (1999).

[83] K. Wang, S. Kundu, H. Lee, and H. Liang, The Journal of Physical Chemistry C **113** (19), 8112 (2009).

[84] S. M. Hsu, J. Zhang, and Z. Yin, Tribology Letters **13** (2), 131 (2002).

[85] P. Kar, P. Asthana, and H. Liang, Journal of Tribology **130** (4), 042301 (2008).

[86] A. Morina and A. Neville, Journal of Physics D: Applied Physics **40** (18), 5476 (2007).

[87] J. S. Sheasby, T. A. Caughlin, and J. J. Habeeb, Wear **150** (1-2), 247 (1991); S. Bec, A. Tonck, J. M. Georges, R. C. Coy, J. C. Bell, and G. W. Roper, Proceedings of the Royal Society of London, Series A (Mathematical, Physical and Engineering Sciences) **455**, 4181 (1999).

[88] H. Spedding and R. C. Watkins, Tribology International **15** (1), 9 (1982).

[89] J. Ye, M. Kano, and Y. Yasuda, Tribology Letters **16** (1), 107 (2004).

[90] J. B. Retzloff, B. T. Davis, M. E. Gluckstein, and J. M. Pietras, Lubrication Engineering **35**, 568 (1979).

[91] P.-Y. Zheng, X.-A. Han, and R.-L. Wang, Proceedings of ASLE Preprints Presented at the ASME/ASLE Tribology Conference., Pittsburgh, PA, USA, 1986; Y. Yamamoto, S. Gondo, T. Kamakura, and N. Tanaka, Wear **112**, 79 (1986).

[92] Y. Yamamoto, S. Gondo, T. Kamakura, and M. Konishi, Wear **120**, 51 (1987); C. Grossiord, J. M. Martin, T. Le Mogne, K. Inoue, and J. Igarashi, Journal of Vacuum Science & Technology A (Vacuum, Surfaces, and Films) **17**, 884 (1999); C. Guerret-Piecourt, C. Grossiord, T. Le Mogne, J. M. Martin, and T. Palermo, Surface and Interface Analysis **30**, 646 (2000).

[93] A. R. Lansdown, *Molybdenum Disulphide Lubrication*. (Elseiver Science, Amsterdam, 1999).

[94] C. Kajdas and K. Hiratsuka, Proceedings of the Institution of Mechanical Engineers, Part J (Journal of Engineering Tribology) **223**, 827 (2009).

[95] B. Vick, M. J. Furey, and S. J. Foo, Numerical Heat Transfer; Part A: Applications **20**, 19 (1991).

[96] J. Vizintin, in *Surface Modifications and Mechanisms*, edited by G.E. Totten and H. Liang (Marcel Dekker, Inc, New York, 2004), pp. 243.

[97] J. Ferrante, ASLE Transactions **20**, 328 (1977).

[98] M. J. Furey and C. Kajdas, in *Surface Modification and Mechanisms*, edited by G.E. Totten and H. Liang (Marcel-Dekker Inc, New York, 2004), pp. 165.

[99] C. Kajdas, M. J. Furey, A. L. Ritter, and G. J. Molina, Lubrication Science **14**, 223 (2002); G. J. Molina, M. J. Furey, A. L. Ritter, and C. Kajdas, Tribologia **21**, 3 (2002).

[100] J. J. Gilman, Science **274**, 65 (1996).

[101] K. Nakayama and H. Hashimoto, Wear **185**, 183 (1995); K. Nakayama and H. Hashimoto, Tribology Transactions **38**, 541 (1995); R. A. Nevshupa and K. Nakayama, Journal of Applied Physics **93**, 9321 (2003).

[102] C. Z. Kajdas, ASLE Transactions **28**, 21 (1985); K. Nakayama, N. Suzuki, and H. Hashimoto, Journal of Physics D (Applied Physics) **25**, 303 (1992).

[103] G. J. Molina, M. J. Furey, A. L. Ritter, and C. Kajdas, Proceedings of 9th Nordic Symposium on Tribology, NORDTRIB 2000, 11-14 June 2000, Netherlands, 2001.

[104] A. K. Geim and P. Kim, in *Scientific American* (2008), Vol. April.

[105] D. J. Godfrey, (1968), Vol. 10.

[106] M. C. Kim, G. S. Hwang, and R. S. Ruoff, The Journal of Chemical Physics **131** (6), 064704 (2009).

[107] X. Gao, J. Jang, and S. Nagase, The Journal of Physical Chemistry C **114** (2), 832 (2009).

[108] D. A. Dikin, Nature **448**, 457 (2007).

[109] S. Wang, Y. Zhang, N. Abidi, and L. Cabrales, Langmuir **25** (18), 11078 (2009).

[110] G. Wang, B. Wang, J. Park, J. Yang, X. Shen, and J. Yao, Carbon **47** (1), 68 (2009).

[111] R. D. Piner, J. Zhu, F. Xu, S. Hong, and C. A. Mirkin, Science **283** (5402), 661 (1999); M. Binggeli and C. M. Mate, Applied Physics Letters **65** (4), 415 (1994).

[112] F. Tuinstra and J. L. Koenig, The Journal of Chemical Physics **53** (3), 1126 (1970).

[113] M. A. Pimenta, G. Dresselhaus, M. S. Dresselhaus, L. G. Cancado, A. Jorio, and R. Saito, Physical Chemistry Chemical Physics **9** (11), 1276 (2007).

[114] D. Graf, F. Molitor, K. Ensslin, C. Stampfer, A. Jungen, C. Hierold, and L. Wirtz, Nano Letters **7** (2), 238 (2007).

[115] M. Hulman, M. HalušKa, G. Scalia, D. Obergfell, and S. Roth, Nano Letters **8** (11), 3594 (2008).

[116] A. C. Ferrari, J. C. Meyer, V. Scardaci, C. Casiraghi, M. Lazzeri, F. Mauri, S. Piscanec, D. Jiang, K. S. Novoselov, S. Roth, and A. K. Geim, Physical Review Letters **97** (18), 187401 (2006).

[117] K. Sato, R. Saito, Y. Oyama, J. Jiang, L. G. Cançado, M. A. Pimenta, A. Jorio, G. G. Samsonidze, G. Dresselhaus, and M. S. Dresselhaus, Chemical Physics Letters **427** (1-3), 117 (2006).

[118] S. M. Hsu, Z. Jun, and Y. Zhanfeng, Tribology Letters **13**, 131 (2002).

[119] J. Lin, L. Wang, and G. Chen, Tribology Letters **41** (1), 209 (2011).

[120] J. I. Paredes, S. Villar-Rodil, A. MartíNez-Alonso, and J. M. D. TascóN, Langmuir **24** (19), 10560 (2008).

[121] K. A. Worsley, P. Ramesh, S. K. Mandal, S. Niyogi, M. E. Itkis, and R. C. Haddon, Chemical Physics Letters **445** (1-3), 51 (2007).

[122] S. F. Braga, V. R. Coluci, S. B. Legoas, R. Giro, D. S. Galvão, and R. H. Baughman, Nano Letters **4** (5), 881 (2004).

[123] J. B. Aladekomo and R. H. Bragg, Carbon **28** (6), 897 (1990).

[124] G. L. Vaghjiani, The Journal of Chemical Physics **98** (3), 2123 (1993).

[125] E.-Y. Choi, T. H. Han, J. Hong, J. E. Kim, S. H. Lee, H. W. Kim, and S. O. Kim, Journal of Materials Chemistry **20** (10), 1907 (2010).

[126] D. Li, M. B. Muller, S. Gilje, R. B. Kaner, and G. G. Wallace, Nat Nano **3** (2), 101 (2008).

[127] S. Stankovich, R. D. Piner, S. T. Nguyen, and R. S. Ruoff, Carbon **44** (15), 3342 (2006).

[128] H. R. Tang and D. M. Stanbury, Inorganic Chemistry **33** (7), 1388 (1994).

[129] F. Z. Chen, D. L. Judge, C. Y. R. Wu, and J. Caldwell, Planetary and Space Science **47** (1-2), 261 (1998).

[130] C. K. Kajdas, Proceedings of 1st International Conference: Mechatronic Systems and Materials, MSM 2005, October 20, 2005 - October 23, 2005, Vilnius, Lithuania, 2006.

[131] H. Tomizawa and T. E. Fischer, ASLE Transactions **30**, 41 (1987).

[132] Y. Si and E. T. Samulski, Nano Letters **8** (6), 1679 (2008).

[133] A. V. Murugan, T. Muraliganth, and A. Manthiram, Chemistry of Materials **21** (21), 5004 (2009).

[134] L. Lai, L. Chen, D. Zhan, L. Sun, J. Liu, S. H. Lim, C. K. Poh, Z. Shen, and J. Lin, Carbon **49** (10), 3250 (2011).

[135] S. Hou, S. Su, M. L. Kasner, P. Shah, K. Patel, and C. J. Madarang, Chemical Physics Letters **501** (1-3), 68 (2010).

[136] T. Fujii, M. Yoshimoto, T. Fuyuki, and H. Matsunami, Japanese Journal of Applied Physics **36** (Part 1, No. 1A), 289 (1997).

[137] M. T. Kim and J. Lee, Thin Solid Films **303** (1-2), 173 (1997).

[138] D. H. Williams and I. Fleming, *Spectroscopic Methods in Organic Chemistry*, 4th ed. (McGraw-Hill Book Company (UK) Limited, Maidenhead-Berkshire, England, 1987).

[139] T. Kaneko, D. Nemoto, A. Horiguchi, and N. Miyakawa, Journal of Crystal Growth **275** (1-2), e1097 (2005).

[140] K. Yamamoto, Y. Koga, and S. Fujiwara, Japanese Journal of Applied Physics, Part 1 **40** (Part 2, No. 2A), L123 (2001); A. P. Dementjev, A. De Graaf, M. C. M. Van De Sanden, K. I. Maslakov, A. V. Naumkin, and A. A. Serov, Diamond and Related Materials **9** (11), 1904 (2000); E. P. Dillon, C. A. Crouse, and A. R. Barron, ACS Nano **2** (1), 156 (2008).

[141] K. L. Smith and K. M. Black, Journal of Vacuum Science & Technology A: Vacuum, Surfaces, and Films **2** (2), 744 (1984).

[142] D. Kuhlmann-Wilsdorf, Wear **107** (Compendex), 71 (1986); D. Kuhlmann-Wilsdorf, Material Science and Engineering **93**, 107 (1987); D. Kuhlmann-Wilsdorf, Material Science and Engineering **93**, 119 (1987); D. Kuhlmann-Wilsdorf, Journal of Tribology **109**, 321 (1987).

[143] J. A. Greenwood, Wear **150**, 153 (1991).

[144] X. Tian and F. E. Kennedy, Journal of Tribology **116**, 167 (1994).

[145] B. Bhushan, *Modern Tribology Handbook*. (CRC Press, New York, 2001).

[146] J. B. J. Fourier, *Théorie Analytique de la Chaleur*. (Chez Firmin Didot, père et fils, Paris, 1822).

[147] B. Bhushan, Journal of Tribology **109**, 243 (1987).

[148] J. C. Jaeger, Royal Society of New South Wales -- Journal and Proceedings **76** (Part 3), 203 (1942).

[149] A. Yevtushenko and E. Ivanyk, Wear **206**, 53 (1997).

[150] F. E. Kennedy Jr and F. F. Ling, American Society of Mechanical Engineers (1973).

[151] X. Tian and F. E. Kennedy, Proceedings of the Institution of Mechanical Engineers, Part J: Journal of Engineering Tribology **209**, 41 (1995).

[152] S. J. Blanksby and G. B. Ellison, Accounts of Chemical Research **36** (4), 255 (2003); R. T. Sanderson, *Chemical bonds and bond energy*. (Academic Press, New York, 1976).

[153] M. J. Furey, C. Kajdas, G. J. Molina, and B. Vick, Proceedings of 2005 World Tribology Congress III, September 12, 2005 - September 16, 2005, Washington, D.C., United states, 2005.

[154] C. K. Kajdas, Proceedings of Boundary Lubrication, *Tribology International, 3rd Ed.* **38**, 337 (2005).

[155] C. Kajdas, Lubrication Science **6**, 203 (1994).

[156] L. A. Buyanovsky, Frict. Wear **14**, 174 (1993).

APPENDIX A

TRIBOSYNTHESIS SUPPLEMENTAL DATA

Supplemental data from the tribosynthesis tests are provided in this appendix. The first section will focus on friction monitoring data from the control experiments of dry sliding of graphite on silicon. The following section will show some additional results of platelet formation in other tests.

Control Experiments

In the control experiments, the friction monitoring data for sliding experiments is provided in this section of the appendix. In Figure A - 1, the two-cycle friction response for 1N loading at various maximum speed conditions is shown. The flat nature of the peaks and valleys show a relative independence upon speed in the friction coefficient, although the average value in the peaks tends to be slightly depended on the max speed.

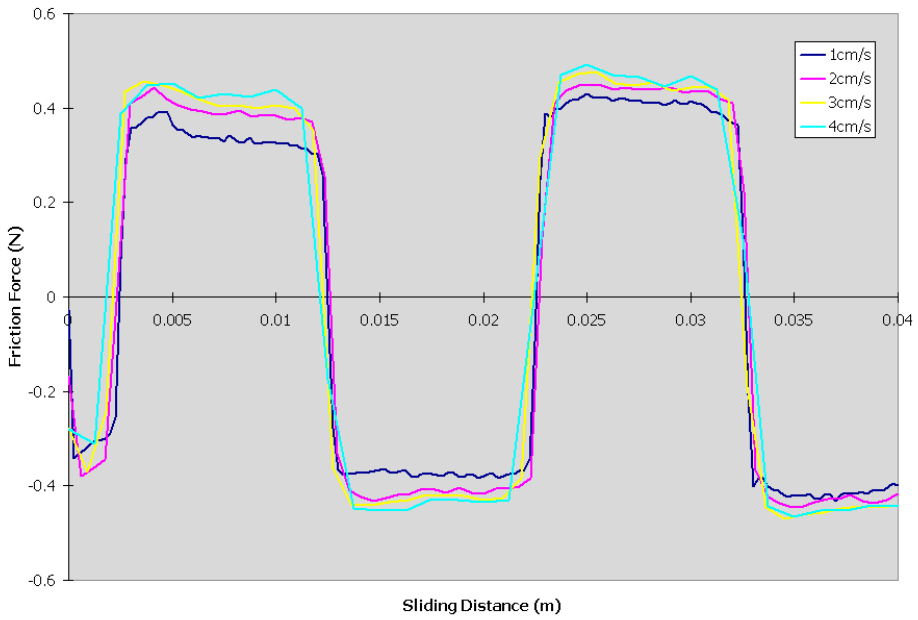

Figure A - 1. 1N Friction Coefficient for Control experiment

But when looking at the net behavior over a longer cycling period, we find that the friction coefficient is really stable as seen in Figure A - 2.

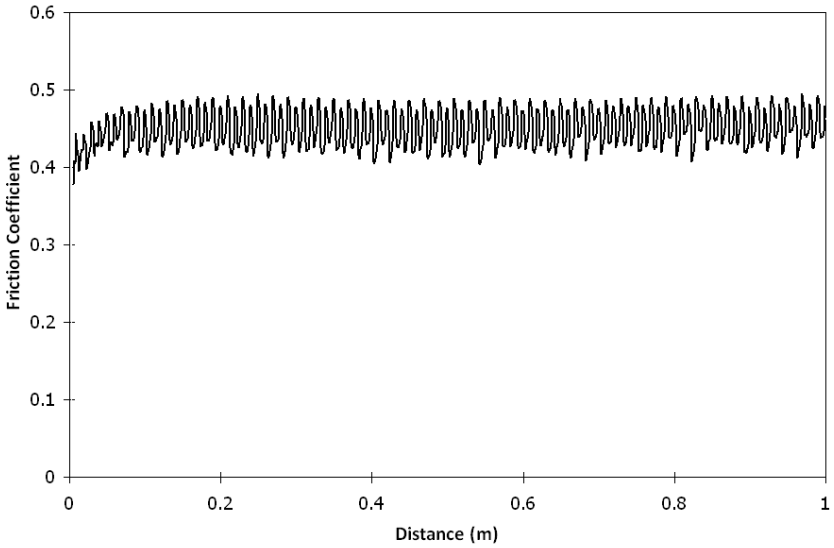

Figure A - 2. 50 cycle friction behavior for 1N load at 2cm/s

A very similar behavior is observed in the case of 2N loading, which is depicted in Figure A - 3, along with the 50 cycle behavior in Figure A - 4.

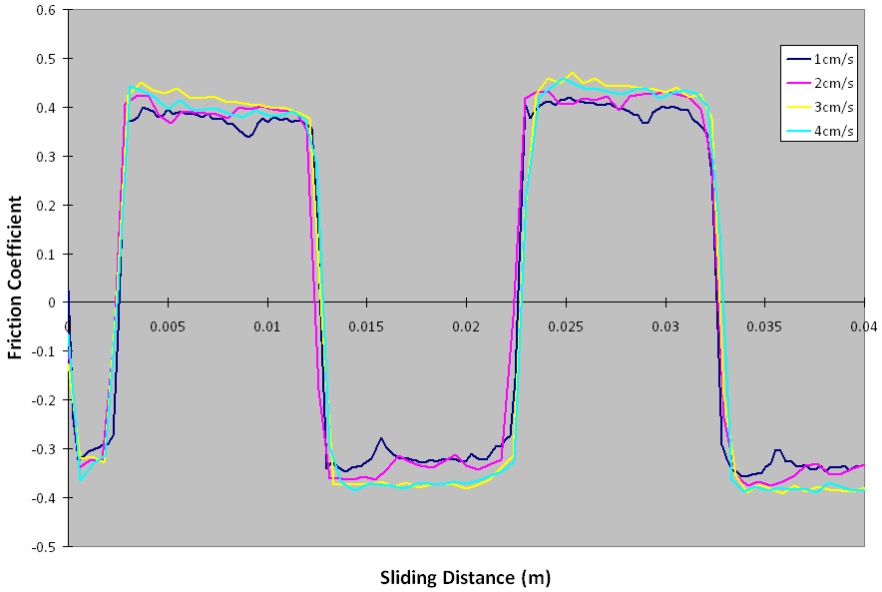

Figure A - 3. 2N Friction Coefficient for Control experiment

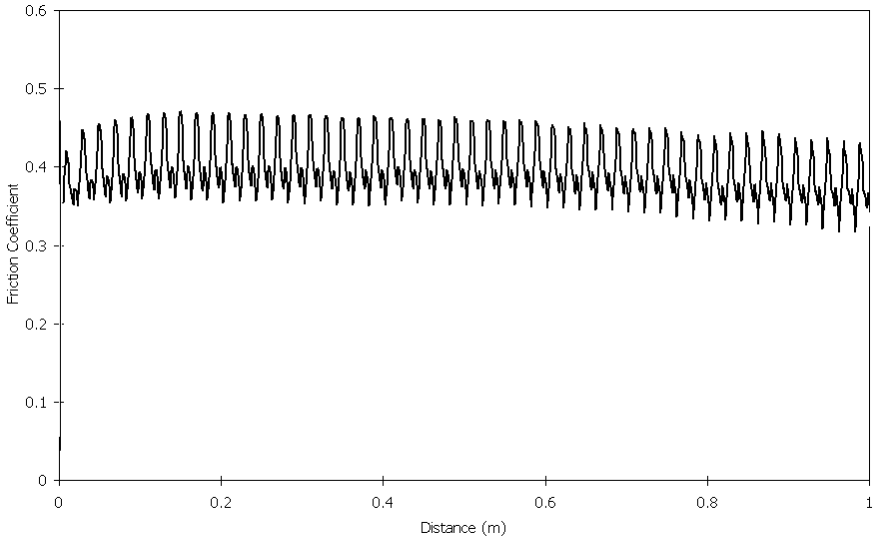

Figure A - 4. 50 cycle friction behavior for 2N Load, 2cm/s

When applying larger loads as seen in Figure A - 5, the deviation in friction coefficients at different speeds disappears, indicating that it may be an issue of sensitivity in the load cell at lower loads. Even so we still see an average friction coeffiecient near 0.35-0.4 in both Figure A - 5 and Figure A - 6 with 50 cycles.

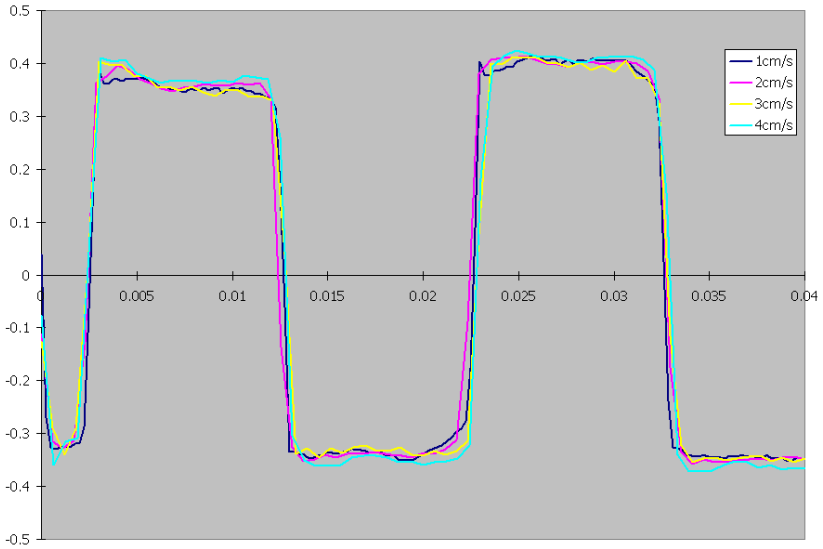

Figure A - 5. 3N Friction Coefficient for Control experiment

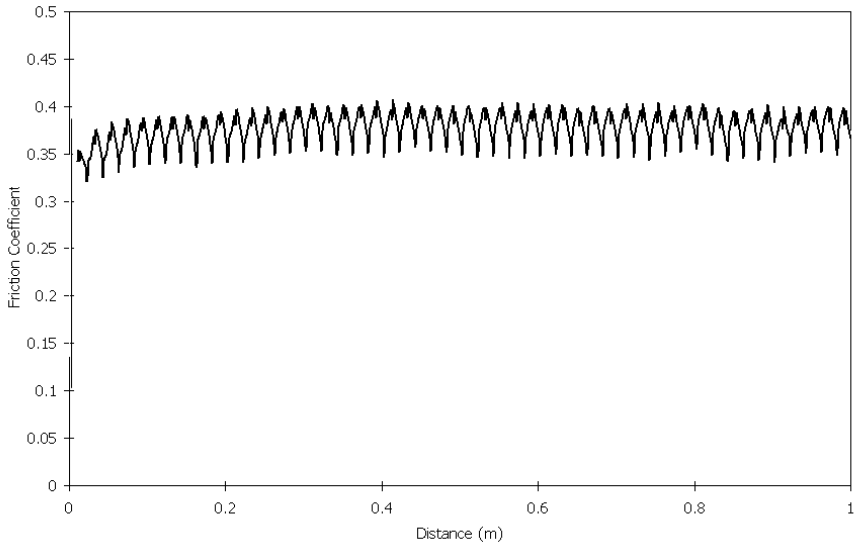

Figure A - 6. 50 cycle friction behavior for 3N Load, 2cm/s

Again a very similar response is seen in the case of 4N loading as seen in Figure A - 7.

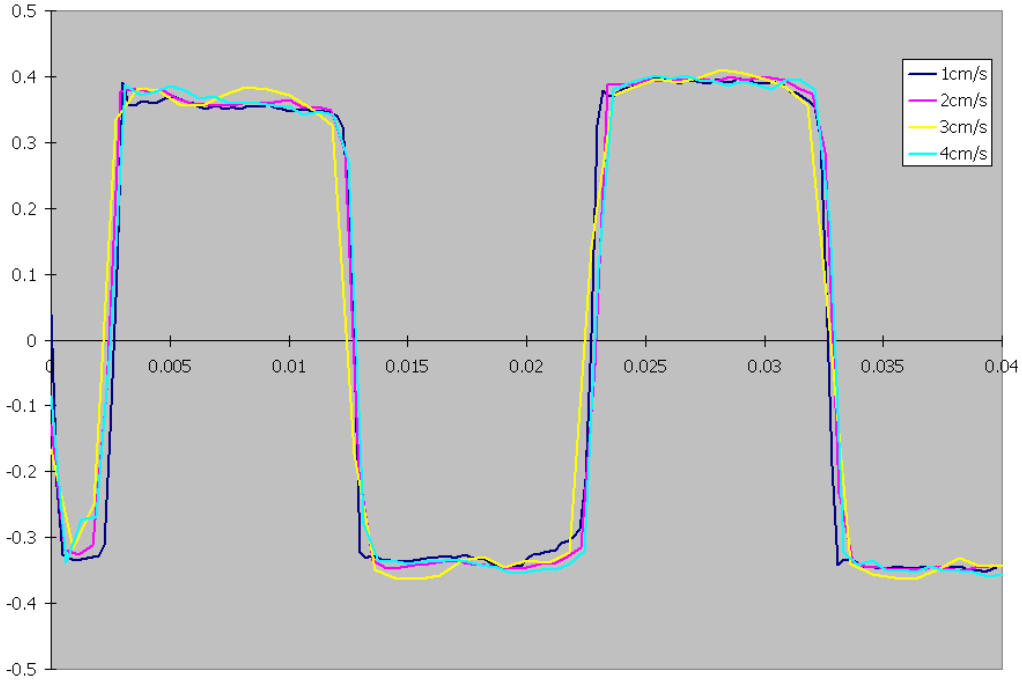

Figure A - 7. 4N Friction Coefficient for Control experiment

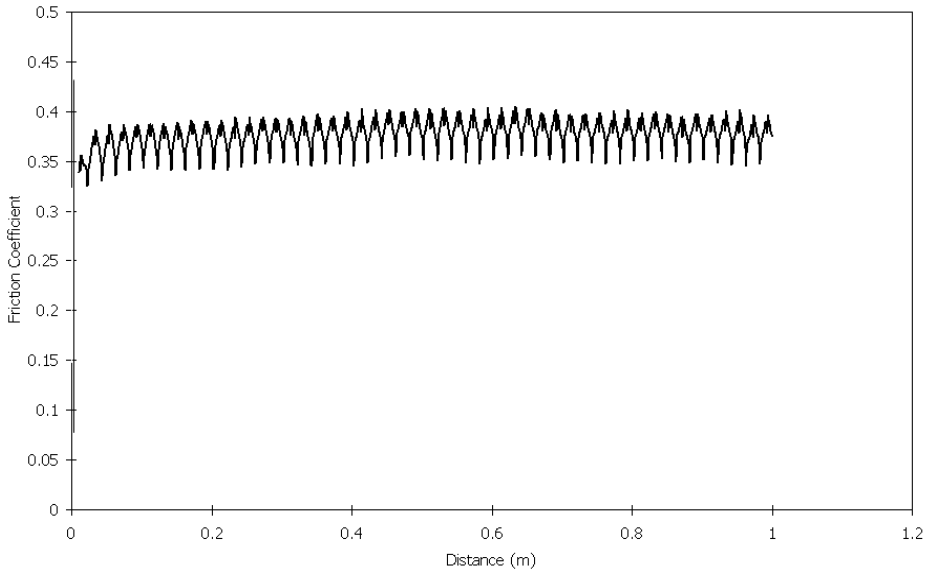

Figure A - 8. 50 cycle friction behavior for 4N Load, 2cm/s

Additionally the 4N load at 50 cycles shows another similar friction response during the abrasion of graphite onto the silicon substrate shown in Figure A - 8.

AFM of Nanoplatelet formations.

Unlike the control experiments, the presence of hydrazine hydrate facilitated the formation of many platelets on the surface of the Si during sliding experiments. The following figures and results document some of the additional platelet formations observed from sliding in suspended graphite in $N_2H_4H_2O$. For instance, in Figure A - 9, when sliding the formation of the characteristic 2.5nm thick large (nearly 10μm) nano-flakes were seen immediately alongside thicker and smaller flakes, as demonstrated in Figure A - 10. Furthermore, curling at the edges of the thinner platelets is observed, falling in line with predictions of stability of large platelets of graphene.

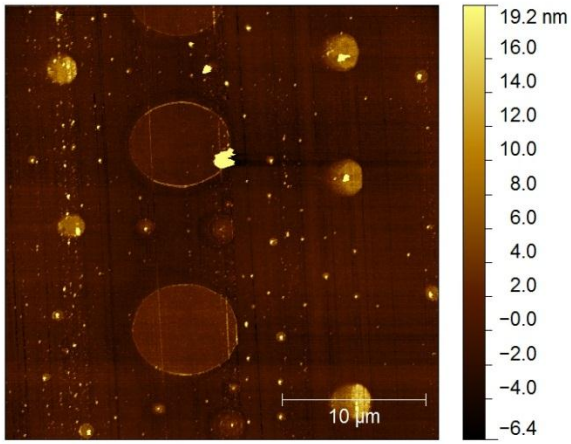

Figure A - 9. Platelet formations from wet sliding in hydrazine hydrate with suspended graphite.

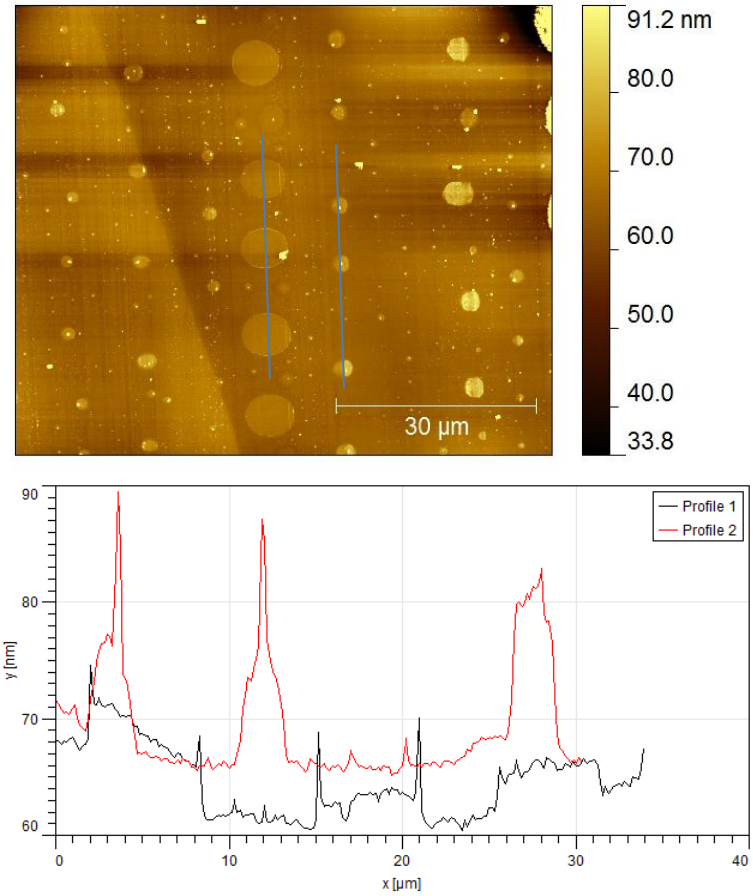

Figure A - 10. AFM of platelets (top) and height profiles (bottom) showing dimensions.

Additionally many other flake formations were observed in wet sliding along the surface. In Figure A - 11, many flake-like shapes are observed, but in some cases they appear to be incomplete. This may suggest that the flakes do not grow radially but start with the collection of debris in a localized area which is then stitched together.

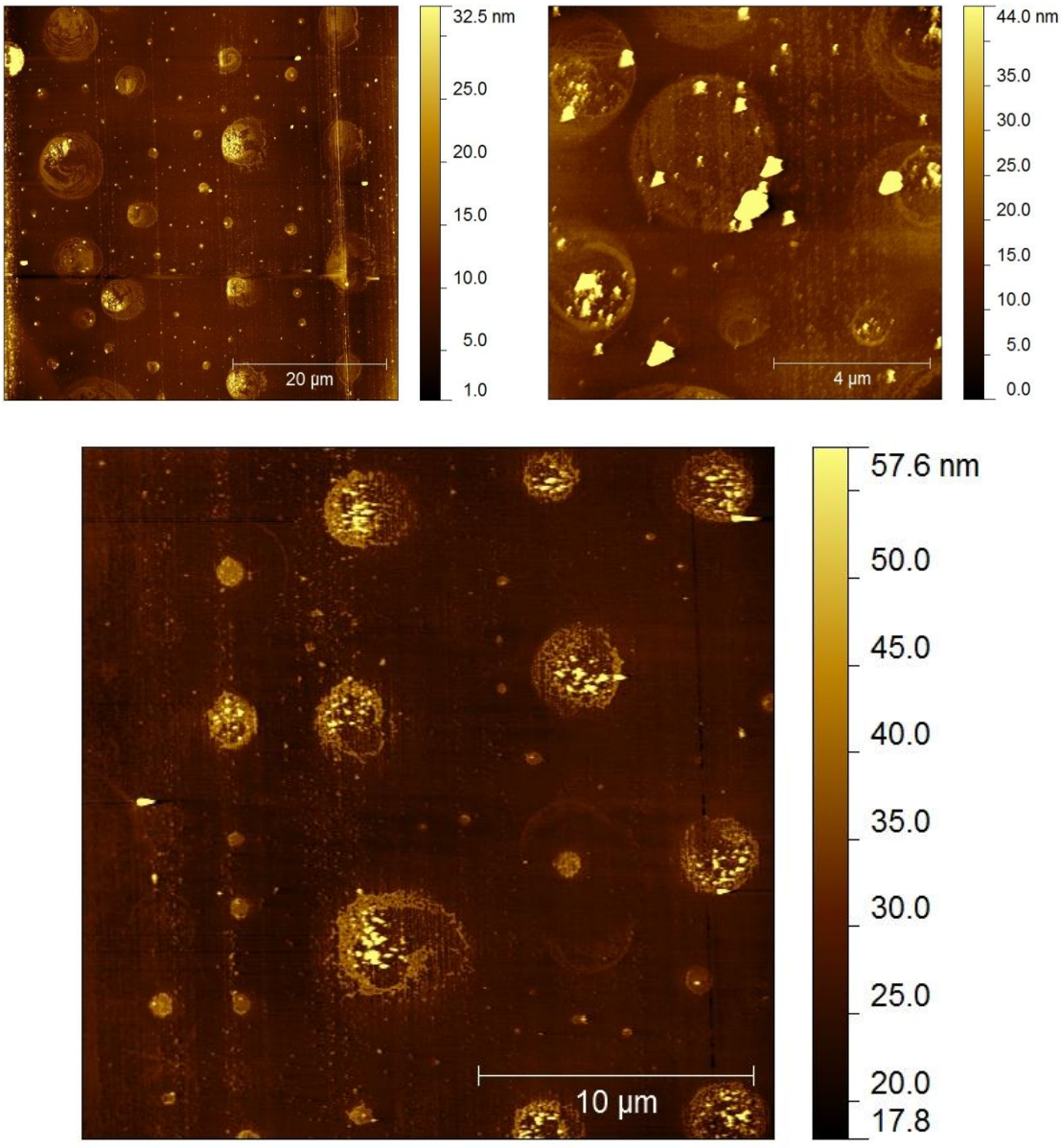

Figure A - 11. Flake nucleations, perhaps showing the development of the CMG flakes produced from the tribosynthesis procedure.

APPENDIX B

CHEMICAL PREPARATION OF CHEMICALLY MODIFIED GRAPHENES

In addition to all the tribosynthesis tests, a number of chemical approaches were taken to investigate the production of graphene-based nanoplatelets as alternate reaction pathways. The method of production involved dispersion of shaved graphite in hydrazine hydrate, and then treating with various energy inputs to facilitate growth of graphene platelets.

Chemically Prepared CMGs

In the first case, (called CMG1) the shaved graphite in hydrazine hydrate was exposed to UV irradiation for 75 minutes, and ultrasonicated. The resulting dispersion was evaluated in TEM which found the presence of coagulated flakes were seen as shown in Figure B - 1. These were discussed earlier in the report. These flakes showed the representative 150 degree angle of the graphitic lattice. The same was not seen in the case that the suspension was not exposed to the UV irradiation.

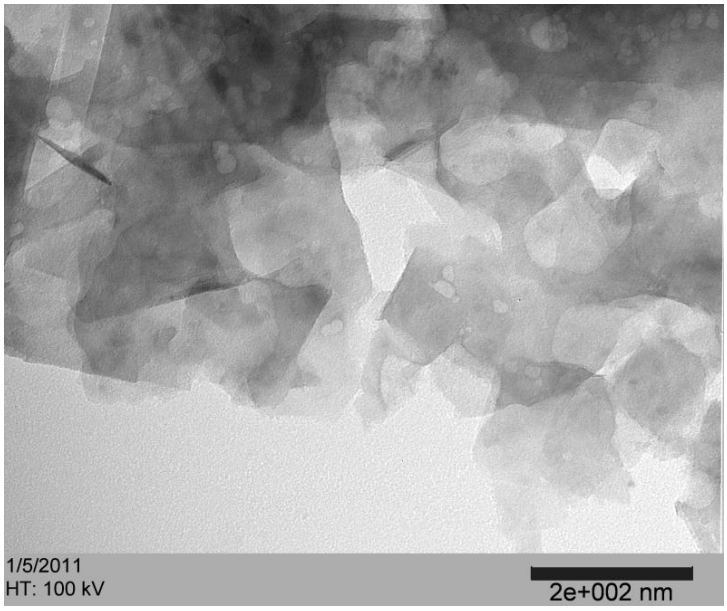

Figure B - 1. CMG1 showing production of coagulated flakes.

In the other samples, the effect of Pt as a catalyst agent was investigated based on preliminary results seen from other experiments (not discussed in this report). In the case of CMG2, the combination of Pt and shaved graphite in hydrazine hydrate was placed in a microwave and heated using repeated bursts of energy of a few seconds at 10 second intervals, in order to avoid boiling of the liquid. The resulting suspension was similarly studied in TEM, as shown in Figure B - 2. Here flake-like formations were also observed, with the exception that multiple layers of the structure were well aligned as evidenced by the edges of the particle.

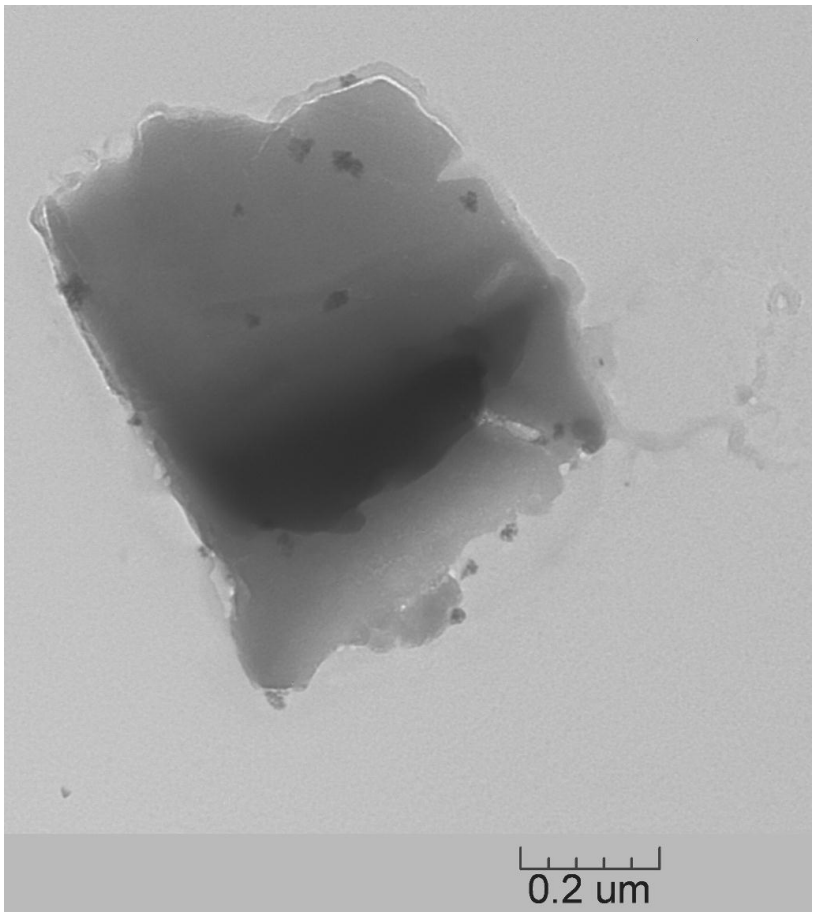

Figure B - 2. CMG2. Layered flake structure of ordered size from μ-wave processing with Pt cubes also seen in image.

Similarly to CMG1, CMG3 was prepared by UV irradiation, with the exception that Pt nanoparticles were incorporated into the suspension to encourage catalytic action. In fact, as seen in Figure B - 3, larger and more distinct platelets were indeed formed from this process. Much clearer separation and distinct boundaries are observed in this image, along with folding of the edges of the platelets.

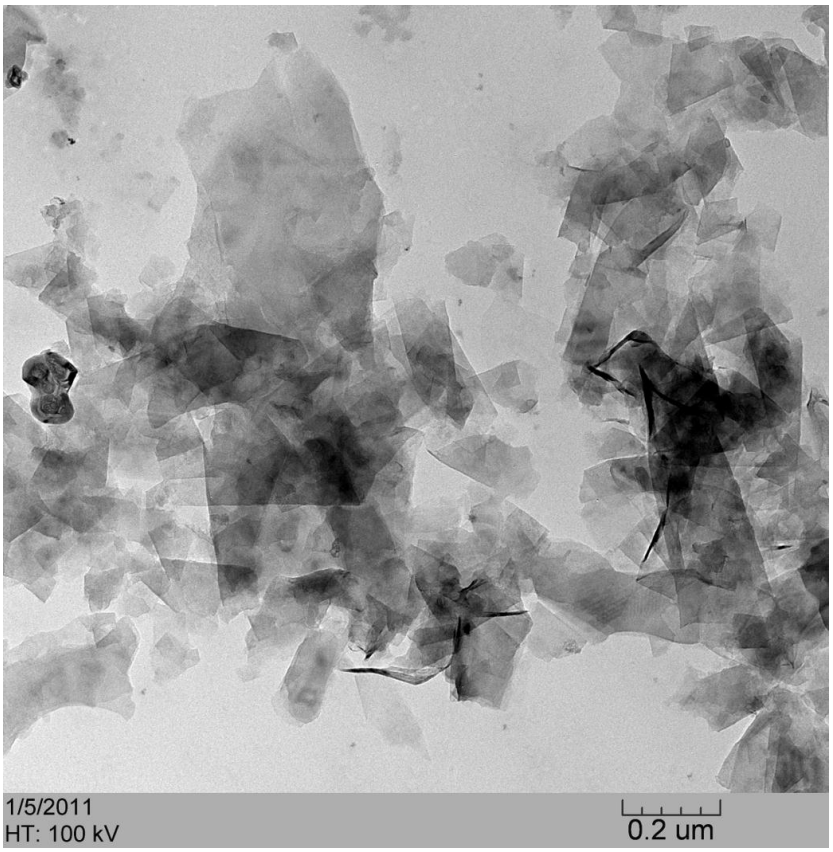

Figure B - 3. CMG3. Flake particles from UV processing with Pt cubes, showing more separated behavior and distinct boundaries.

Each of the resulting samples were tested for UV-vis absorption, which is shown in Figure B - 4. When looking at the "base solution," or the hydrazine hydrate with only shaved graphite (no energy input), the absorption showed a peak characteristic of a graphite oxide, whereas in every other case, the unique graphene absorption peak is observed at 232 nm. This indicates that these pathways are indeed methods to arrive at the formation of graphenes, however, the morphology from each method is slightly different.

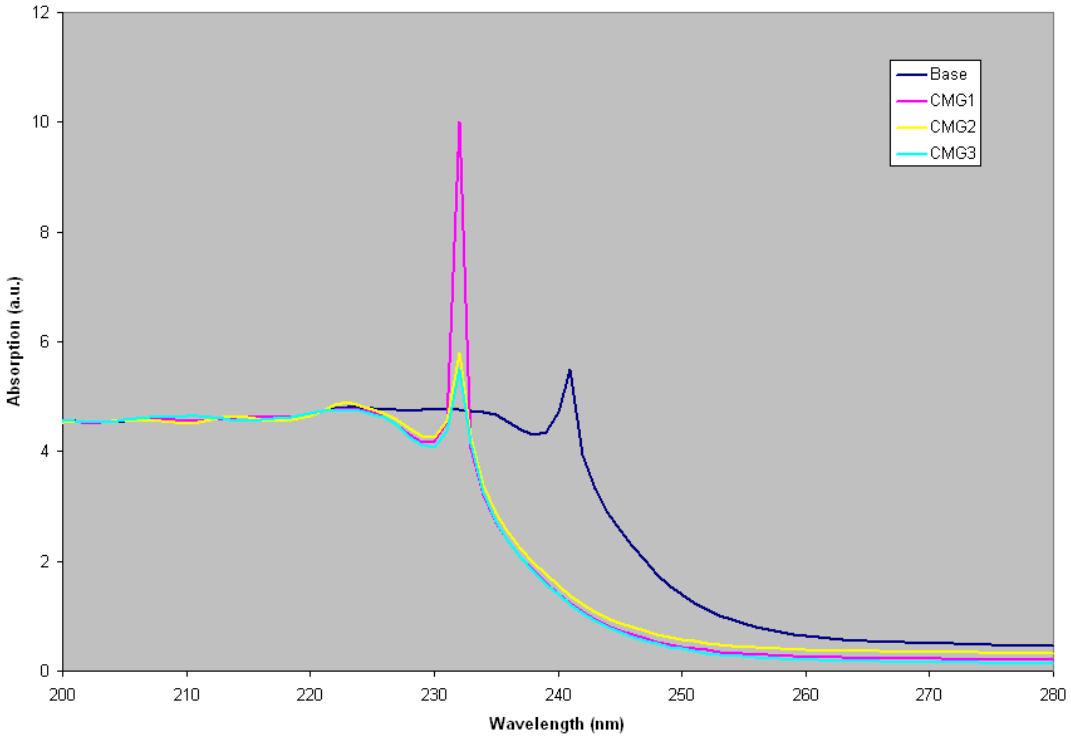

Figure B - 4. Absorption spectra for CMGs compared against starting suspension of graphite in hydrazine hydrate (base). CMG1: UV exposure; CMG2: add in Pt cubes and microwave exposure; CMG3: add in Pt cubes and additional UV exposure.

VITA

Name: David Ryan Huitink

Address: TAMU 3123

Dept. of Mechanical Engineering

Rm 100 ENPH

College Station, TX 77843-3123

Email Address: david.huitink@gmail.com

Education: B.S., Mechanical Engineering, Texas A&M University, 2006

M.S., Mechanical Engineering, Texas A&M University, 2007

Ph.D., Mechanical Engineering, Texas A&M University, 2011